9-2022

Efficiency Quantification for Pulsed-source Digital Holographic Wavefront Sensing

Steven A. Owens

EFFICIENCY QUANTIFICATION FOR PULSED-SOURCE DIGITAL HOLOGRAPHY

DISSERTATION

Steven A. Owens, Captain, USAF

AFIT-ENP-DS-22-S-046

DEPARTMENT OF THE AIR FORCE
AIR UNIVERSITY

AIR FORCE INSTITUTE OF TECHNOLOGY

Wright-Patterson Air Force Base, Ohio

AFIT-ENP-DS-22-S-046

EFFICIENCY QUANTIFICATION FOR PULSED-SOURCE DIGITAL HOLOGRAPHY

DISSERTATION

Presented to the Faculty

Department of Engineering Physics

Graduate School of Engineering and Management

Air Force Institute of Technology

Air University

Air Education and Training Command

In Partial Fulfillment of the Requirements for the

Degree of Doctor of Philosophy in Applied Physics

Steven A. Owens, BS, MS

Captain, USAF

August 2022

AFIT-ENP-DS-22-S-046

EFFICIENCY QUANTIFICATION FOR PULSED-SOURCE DIGITAL HOLOGRAPHY

Steven A. Owens, BS, MS

Captain, USAF

Committee Membership:

Dr. Glen P. Perram
Chairman

Dr. Mark F. Spencer
Member

Dr. Jack E. McCrae
Member

Dr. Benjamin F. Akers
Member

ADEDEJI B. BADIRU, PhD
Dean, Graduate School of Engineering and Management

AFIT-ENP-DS-22-S-046

Abstract

This dissertation analyzes the efficiencies of a digital holography (DH) system in the pulsed configuration and the off-axis image plane recording geometry, and is comprised of three unique contributions. For the first contribution, the system efficiencies of an infrared-wavelength DH system in a homodyne-pulsed configuration are measured and compared to those of a visible-wavelength DH system in a homodyne-continuous-wave (CW) configuration. The total-system, excess-reference-noise, shot-noise-limit, and mixing efficiencies of the pulsed-source system were found to be consistent with those of the CW-source system. This indicated no new efficiencies were necessary to characterize pulsed-source systems when no temporal delay exists between the pulses. The consistency of efficiencies also showed infrared DH systems are viable but degraded due to infrared detector technology. A new efficiency, called the ambiguity efficiency, was introduced to account for the degradation in system performance as the temporal delay between the pulses increased. This novel efficiency was then experimentally verified. For the second contribution, a DH system in a heterodyne-pulsed configuration was characterized in terms of the total-system and ambiguity efficiencies. The efficiencies measured using a heterodyne-pulsed configuration were consistent with those measured using a homodyne-pulsed configuration. Therefore, there was no degradation in system performance by changing from a homodyne configuration to a heterodyne configuration. This will allow the effective range of pulsed-source DH systems to greatly increase. For the third contribution, the effect of spectral broadening of the source laser of a DH system in the heterodyne-pulsed configuration was analyzed. Experiments showed the ambiguity efficiency was not significantly affected by the degradation in temporal

coherence. However, the total-system efficiency did change as a function of temporal coherence degradation.

Acknowledgements

I would like to thank Dr. Glen Perram. It has been a pleasure working for and with him for the past three years and for the year and a half of my Master's program. This experience would not have gone as well as it did without his knowledge and guidance through classwork, research, and the writing process.

I would also like to thank Dr. Mark Spencer as the spiritual, and in many ways actual sponsor of my work at AFIT. He did everything from giving me a lot of his time to teach me the ins-and-outs of digital holography, including a month of hands-on teaching at Kirtland AFB, to teaching me a totally different way of writing papers, to continuing his support after he PCS'd to Hawaii. This project would not have been possible without him.

Dr. Jack McCrae and Lt Col Milo Hyde deserve thanks as well. Outside of hosting one-on-one independent studies to ensure I had the knowledge needed to complete this project, they were both available whenever I needed to help with complex, one-off issues. Even if it required multiple hours across multiple days within their already busy schedules.

To all of my other instructors and the lab technicians, I know my incessant questioning did not make life easy. Thank you for always being willing to help out. You are what keep AFIT the quality institution that it is.

Table of Contents

List of Figures

List of Tables

List of Symbols

Symbol Page

Symbol		Page
G	Phase-modulated line shape [*unitless*]	66
A_L	Amplitude of the Lorentzian line shape [*unitless*]	66
A_S	Amplitude of the sinc^2 line shape [*unitless*]	66
$\Delta\nu_L$	Width of the Lorentzian line shape [*Hz*]	66
$\Delta\nu_S$	Width of the sinc^2 line shape [*Hz*]	66
ν_0	Center frequency of the line shape [*Hz*]	66
β	Ratio of energy in the sinc^2 line shape [*unitless*]	67
η_{coh}	Coherence efficiency [%]	67
γ_{eff}	Effective complex degree of coherence [*unitless*]	68
γ	Complex degree of coherence [*unitless*]	68
T_R	Temporal profile of the reference pulse [*unitless*]	69
T_S	Temporal profile of the signal pulse [*unitless*]	69
V_{p-p}	Peak-to-peak voltage of the PRBS signal [*V*]	71
$\overline{\nu}_1$	Fundamental mode central frequency [*Hz*]	95
$\overline{\nu}_2$	Transverse mode central frequency [*Hz*]	95
ω	Angular frequency [*Hz*]	102

List of Abbreviations

EFFICIENCY QUANTIFICATION FOR PULSED-SOURCE DIGITAL HOLOGRAPHY

I. Introduction

Military applications involving light propagating through long path lengths of atmosphere, such as high energy laser weapons or intelligence, surveillance, and reconnaissance (ISR) missions, can experience severe degradations in performance due to turbulence. Typical adaptive optics techniques to compensate for this degradation include a wavefront sensor and a deformable mirror. Current direct-detection wavefront sensor technology, such as the Shack-Hartmann wavefront sensor, can provide near diffraction-limited performance in weak turbulence conditions, characterized by isoplanatic distortion [1]. Performance of these systems quickly degrades when used in low-light and deep-turbulence scenarios as signal-to-noise ratios (SNRs) are greatly reduced. Additionally, the distributed-volume nature of deep-turbulence environments introduces branch points and branch cuts, or points and lines across the wavefront where the phase shifts by more than 2π radians, as well as anisoplanatism. These branch points and cuts limit the accuracy and, therefore, usability of direct-detection sensors [2]. It is of interest, then, to research an alternate wavefront detection scheme that is robust against low SNRs and anisoplanatism.

Digital holography (DH), based on a concept introduced in the 1960s and made practical by the advent of digital cameras in more recent decades, is one such method [3-5]. By interfering the light reflected off an object of interest, called the signal field, with a strong reference field, experiments and demonstrations have shown DH as tolerant to both low SNRs and deep turbulence [6-21]. The use of a strong reference boosts the signal well above the noise floor of the system, resulting in higher SNRs, and provides access to the complex-optical field, allowing for the estimation of the wrapped phase of the wavefront [22].

In order to maximize the applicability of DH, the limitations of the technique itself and the technology used to perform DH must be well understood. Usability of detection systems is highly dependent on SNR, therefore it is convenient to characterize the performance of different DH schemes and configurations in terms of SNR degradation. For DH, individual sources of SNR loss are known as efficiencies. Previous research into DH efficiencies focused on systems with continuous-wave (CW) sources [4-9, 12, 15-21], mainly due to the long coherence lengths of modern-day CW laser sources. However, experiments showed system performance rapidly degraded as the path-length difference between the signal and reference exceeded the coherence length of the CW source [18]. Therefore, the longitudinal coherence of the source limits the effective ranges of DH systems in a CW configuration.

DH systems using pulsed sources can surpass this limit, allowing for longer effective ranges. While this extended range is advantageous to deep-turbulence applications, DH in a pulsed configuration introduces additional considerations. Principle among these is the temporal overlap of signal and reference pulses. As the path length difference between the pulses deviates from zero, the overlap of the pulse amplitudes will decrease, resulting in a degradation of SNR. And while DH in the pulsed configuration has been used in the microscopy and medical-imaging communities since the 1990's [23-25], there has been no publications concerning this degradation.

Additionally, previous work used visible-wavelength sources. Changing to an infrared (IR) wavelength will increase the utility of DH as modern military lasers are commonly in the IR to take advantage of favorable atmospheric propagation characteristics [26]. However, IR detection technology is inherently noisier than its visible-wavelength counterparts. Thus, there is a need to characterize DH systems performance, in terms of SNR, when IR-wavelength sources are used.

The goal of this dissertation is two-fold: (1) to characterize the SNR degradation, or efficiency, caused by the non-ideal temporal overlap between pulses of DH systems in a pulsed configuration and (2) analyze the system-level effect on DH when an IR wavelength is used as the source. This is achieved through three contributions.

First, the efficiency associated with pulse temporal overlap, called the ambiguity efficiency, is quantified for deterministically correlated, or dependent, reference and signal pulses with wavelengths in the IR. This is accomplished by amplitude-splitting a single pulse to create the required pulses. Because the pulses are identical in all ways expect absolute amplitude, this is called the homodyne-pulsed configuration. Results from this experiment showed the ambiguity efficiency is the only efficiency introduced inherently when changing from a CW configuration to a pulsed configuration. Furthermore, this experiment showed the efficiencies quantified for an IR-wavelength, pulsed configuration are consistent with those quantified for a visible-wavelength, CW configuration.

Second, the ambiguity efficiency is quantified for non-deterministically correlated, or independent, reference and signal pulses. Because the phases of the pulses are non-deterministically correlated, this is called the heterodyne-pulsed configuration. Using independent pulses is of interest as the engineering requirements to interfere dependent pulses are detrimental to deep-turbulence applications. Results from this experiment showed using independent pulses, instead of dependent pulses, does not degrade performance of DH systems in a pulsed configuration.

Third, the effect of degraded temporal coherence within the laser source on DH systems in a heterodyne-pulsed configuration is quantified. High-powered laser sources used for DH applications may not have ideal temporal coherence, leading to a degradation in overall system

performance. Results from this experiment showed degraded temporal coherence within the source did not significantly affect ambiguity efficiency, but did cause a uniform reduction in total-system efficiency.

With the above contributions in mind, this dissertation proceeds in the following manner. Chapter II provides the necessary background information. The individual contributions are then presented in the following Chapters:

Chapter III: Pulsed laser source digital holography efficiency measurements.

Chapter IV: Digital-holography efficiency measurements using a heterodyne-pulsed configuration.

Chapter V: Spectral broadening effects on digital-holography systems in a heterodyne-pulsed configuration.

Lastly, Chapter VI provides a summary of the presented contributions and recommendations for future work.

II. Background

This chapter provides the necessary background material and theory for the contributions presented in Chapters III-V. First, DH in the off-axis image plane recording geometry (IPRG) is presented. Next, the SNR for DH systems in the off-axis IRPG is derived. Then, the reasons for and effects of using an IR-wavelength source are discussed. Lastly, a brief introduction to the ambiguity function is given.

2.1 Digital holography in the off-axis image plane recording geometry

Multiple DH recording geometries exist [6-8, 22], each providing different benefits and drawbacks. For this dissertation, the off-axis image plane recording geometry (IPRG) was used because of the simplicity in setup [6, 15-21]. An example setup for the off-axis IPRG is depicted in Fig. 2.1.

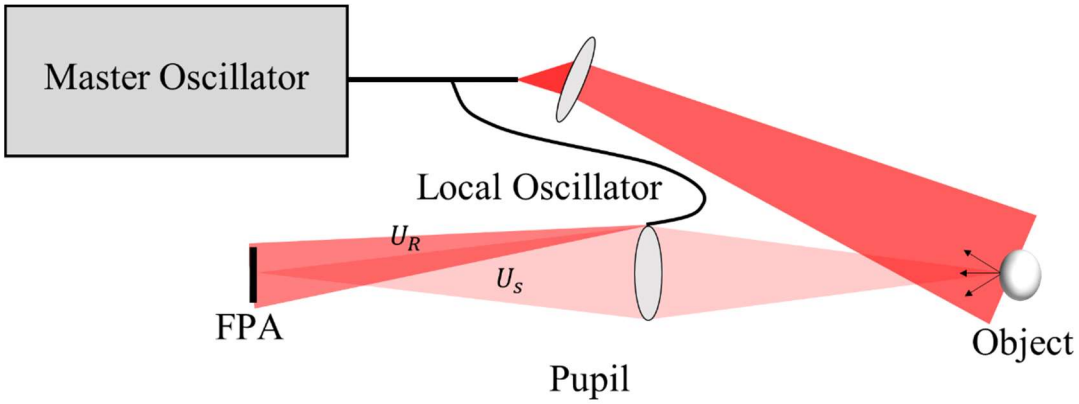

Figure 2.1. Example setup of the off-axis image plane recording geometry.

As shown in Fig. 2.1, a master oscillator splits light into two paths. One path directs light toward and scatters light off an optically rough, extended object. The scattered signal is collected by the pupil of an imaging system. This collected light is imaged onto the focal plane array (FPA) of a camera to create the signal field, U_S. The other optical path consists of a local oscillator that

injects light off-axis relative to the pupil. This light flood illuminates the FPA, creating a strong reference field, U_R. The reference and signal fields are interfered at the FPA, creating a spatially modulated, or fringe, pattern called a hologram.

2.2 Signal-to-noise ratio

To derive the SNR for a DH system in the off-axis IPRG, the irradiance of the hologram must first be defined. With Fig. 2.1 in mind, the hologram irradiance can be written as

$$\begin{aligned} I_H(x_i, y_i) &= \left|U_R(x_i, y_i) + U_S(x_i, y_i)\right|^2 \\ &= \left|U_R(x_i, y_i)\right|^2 + \left|U_S(x_i, y_i)\right|^2 + U_R(x_i, y_i)U_R^*(x_i, y_i) + U_R^*(x_i, y_i)U_S(x_i, y_i) \end{aligned}, \quad (2.1)$$

where I_H is the hologram irradiance, (x_i, y_i) are the image-plane coordinates, $|\bullet|^2$ is the square-magnitude operator, and $*$ denotes the complex conjugate. By design, the image and pupil planes form a Fourier conjugate pair. Therefore, the inverse Fourier transform of the hologram irradiance provides access to the complex-optical field collected by the pupil. This is the field of interest for DH. Taking advantage of the linearity of Fourier transforms, the hologram irradiance in pupil-plane coordinates is then

$$\begin{aligned} I_H(x_p, y_p) &= F^{-1}\left\{I_H(x_i, y_i)\right\} \\ &= F^{-1}\left\{\left|U_R(x_i, y_i)\right|^2\right\} + F^{-1}\left\{\left|U_S(x_i, y_i)\right|^2\right\} \\ &\quad + F^{-1}\left\{U_R(x_i, y_i)U_R^*(x_i, y_i)\right\} + F^{-1}\left\{U_R^*(x_i, y_i)U_S(x_i, y_i)\right\} \end{aligned}, \quad (2.2)$$

where (x_p, y_p) are the pupil-plane coordinates and $F^{-1}\{\bullet\}$ is the inverse Fourier transform operator as defined in Appendix A by Eq. (A.2).

Before proceeding, the form of the reference and signal fields require discussion. The reference field is being injected off-axis from the optical axis of the imaging system. Additionally,

the exit of the local oscillator is typically approximated as a point source [22]. The reference field, then, can be represented by the Fresnel approximation for a tilted spherical wave, such that

$$U_R\left(x_i, y_i\right) = A_R e^{ikz_i} e^{i\frac{k}{2z_i}\left(x_i^2+y_i^2\right)} e^{i\frac{2\pi}{\lambda z_i}\left(x_R x_i + y_R y_i\right)}, \tag{2.3}$$

where A_R is the complex amplitude of the reference, k is the angular wavenumber, z_i is the distance to the image plane, λ is the wavelength, and $\left(x_R, y_R\right)$ is the location of the exit of the local oscillator in the pupil plane. For the off-axis IPRG, the signal field at the image plane can be represented by the Fresnel approximation of a focused plane wave [22], such that

$$U_S = \frac{e^{ikz_i}}{i\lambda z_i} e^{i\frac{k}{2z_i}\left(x_i^2+y_i^2\right)} F\left\{U_p\left(\frac{x_i}{\lambda z_i}, \frac{y_i}{\lambda z_i}\right)\right\}, \tag{2.4}$$

where $F\{\bullet\}$ is the Fourier transform operator as defined by Eq. (A.1) and U_P is the complex-optical field passing through the pupil.

Substituting Eqs. (2.3) and (2.4) into Eq. (2.2), the hologram irradiance in pupil plane coordinates can be written as

$$\begin{aligned} I_H\left(x_p, y_p\right) = {} & \left|A_R\right|^2 \delta\left(x_p, y_p\right) + \frac{1}{\lambda^2 z_i^2} U_P\left(x_p, y_p\right) \otimes U_P^*\left(-x_p, -y_p\right) \\ & + \frac{A_R^*}{j\lambda z_i} U_P\left(x_p - x_R, y_p - y_R\right) - \frac{A_R^*}{j\lambda z_i} U_P\left(x_p + x_R, y_p + y_R\right) \end{aligned}, \tag{2.5}$$

where $\delta(\bullet)$ is the Kronecker delta as defined by Eq. (A.3) and $\otimes$ is the convolution operator. Analyzing Eq. (2.5), the first term shows the magnitude of the reference is located at the origin of the inverse Fourier transform plane. In terms of spatial frequencies, this means the magnitude of the strong reference collapses to DC. The second term is the scaled autocorrelation of the pupil, which is sometimes called the "pupil chat". The third and fourth terms are the spatially separated conjugates of the scaled complex-optical field in the pupil.

To isolate one of the complex-optical field terms, a window function of the form

$$W\left(x_p - x_R, y_p - y_R\right) = \mathrm{Circ}\left(\frac{r_p}{d_p}\right), \tag{2.6}$$

where $\mathrm{Circ}(\bullet)$ is the circle function as defined by Eq. (A.4), $r_p = \sqrt{x_p^2 + y_p^2}$, and d_p is the diameter of the circular window, is applied to Eq. (2.5). Doing so recovers

$$\hat{U}_P\left(x_p, y_p\right) = \frac{A_R^*}{j\lambda z_i} U_P\left(x_p, y_p\right), \tag{2.7}$$

where $\hat{U}_p$ is the estimate of the complex-optical field in the pupil in the absence of noise. To summarize, Eqs. (2.1)-(2.7) detail the general process undertaken to calculate an estimate of the complex-optical field in the pupil from a hologram recorded in the off-axis IPRG.

However, to calculate an expected SNR from the estimated complex-optical field, digitization of the hologram by the FPA must first be introduced. Digitization introduces two effects: (1) discretization and (2) detection noise. Therefore, the previous process (as detailed by Eqs. (2.1)-(2.7)) must be repeated with these effects in mind.

Discretization leads to the hologram being expressed in terms of average irradiance over individual FPA pixels. Assuming the pixels are square and adjacent, the discretized hologram irradiance can be written as

$$\hat{I}_H\left(nx_d, my_d\right) = \frac{1}{\mu^2}\int\int_{-\infty}^{\infty} I_H\left(x_i, y_i\right)\mathrm{Rect}\left(\frac{x_i - nx_d}{\mu}\right)\mathrm{Rect}\left(\frac{y_i - my_d}{\mu}\right)dx_i dy_i, \tag{2.8}$$

where $\hat{I}_H$ is the digitized hologram irradiance, n and m are counting integers for the number of pixels in the x and y dimensions, respectively, x_d and y_d are the distances between pixel centers in the x and y dimensions, respectively, μ is the pixel pitch, and $\mathrm{Rect}(\bullet)$ is the rectangle

function as defined by Eq. (A.5). While not included in Eq. (2.8), the integration time of the detector must also be considered during digitization. If $\hat{I}_H$ is constant in time, Eq. (2.8) is simply multiplied by the total integration time. Otherwise, the discretized hologram irradiance must be integrated as a function of time. For the purposes of this SNR derivation and without loss of generality, $\hat{I}_H$ is assumed temporally constant.

Detection noise encompasses all sources of noise introduced by the detector, but, for DH, detection noise is dominated by shot noise and read noise. As both shot and read noise are photon-related effects, Poisson statistics (i.e., the mean equals the variance) can be assumed for the noise terms. Additionally, if the detector has a sufficiently large number of pixels, the noise terms are delta-correlated and the noise variances are additive [22, 27]. Using these assumptions, the total noise variance can be written such that

$$\sigma_n^2 = \sigma_s^2 + \sigma_r^2, \tag{2.9}$$

where σ_n , σ_s, and σ_r are the standard deviations of the total noise, shot noise, and read noise, respectively.

Taking discretization and noise into account, the average number of photoelectrons generated by each pixel of a detector due to recording a hologram is

$$\bar{m}_H\left(nx_d, my_d\right) = \frac{\eta_q t_i}{h\nu}\mu^2 \hat{I}_H\left(nx_d, my_d\right) + \sigma_n n_k\left(nx_d, my_d\right), \tag{2.10}$$

where η_q is the quantum efficiency of the detector, t_i is integration time, h is Planck's constant, ν is frequency, and n_k is the k-th realization of real-valued, zero mean, unit variance Gaussian random numbers. Repeating the steps taken for Eqs. (2.1)-(2.7), the estimated complex-optical field in the pupil for a DH system in the off-axis IPRG can be written as

$$\hat{U}_P\left(x_p,y_p\right)\approx\frac{\eta_q t_i}{h\nu}\mu^2 A_R^* U_P\left(x_p,y_p\right)+\sqrt{\frac{\pi}{8}}\frac{\sigma_n}{q_I}N_k\left(x_p,y_p\right), \tag{2.11}$$

where q_I is the image plane sampling quotient and N_k is the k-th realization of complex-circular Gaussian random numbers with zero mean and unit variance for both the real and imaginary parts. For reference, the image plane sampling quotient is the spatial sampling resolution of the hologram. In the Fourier plane (i.e., spatial-frequency space), this becomes the number of windowed-pupil functions that can fit across a single dimension of the plane. In practice, DH systems are designed such that $2\le q_I\le 4$.

With an estimate of the complex-optical field in the pupil, the theoretical SNR can now be calculated. This dissertation uses the power definition of SNR [9, 22], such that

$$SNR=\frac{\left\langle\left|\hat{U}_P\left(x_p,y_p\right)\right|^2\right\rangle}{V\left\{\hat{U}_P\left(x_p,y_p\right)\right\}}, \tag{2.12}$$

where $\langle\bullet\rangle$ is the expectation value operator and $V\{\bullet\}$ is the variance operator. Substituting Eq. (2.11) into Eq. (2.12) and assuming $|U_P|^2\approx|A_S|^2$,

$$\begin{aligned} SNR &\approx \eta_{tot}\frac{4q_I^2}{\pi}\frac{\left(\frac{\eta_q t_i}{h\nu}\mu^2\left|A_R\right|^2\right)\left(\frac{\eta_q t_i}{h\nu}\mu^2\left|A_S\right|^2\right)}{\sigma_n^2}, \\ &\approx \eta_{tot}\frac{4q_I^2}{\pi}\frac{\bar{m}_R\bar{m}_S}{\sigma_s^2+\sigma_r^2} \end{aligned} \tag{2.13}$$

where A_S is the complex amplitude of the signal, η_{tot} is the total-system efficiency, and $\bar{m}_R$ and $\bar{m}_S$ are the mean number of photoelectrons generated by the reference and signal, respectively.

Before moving forward, it is important to note a subtle, yet substantial change made between Eqs. (2.11) and (2.13): the inclusion of the total-system efficiency, η_{tot}. This was done

with the foresight that other efficiencies are present in DH systems and must be accounted for. Acknowledging this now allows for a more accurate SNR calculation, such that it will not need to be revisited later.

Because Poisson statistics were assumed and the variances are additive, the shot noise variance can be separated into its components and written as

$$\sigma_s^2 = \bar{m}_R + \bar{m}_S . \tag{2.14}$$

Substituting Eq. (2.14) into Eq. (2.13), the SNR can be written such that

$$SNR \approx \eta_{tot} \frac{4q_I^2}{\pi} \frac{\bar{m}_R \bar{m}_S}{\bar{m}_R + \bar{m}_S + \sigma_r^2} . \tag{2.15}$$

Assuming a strong reference such that the reference noise (and, therefore, $\bar{m}_R$) dominates all other noise sources, Eq. (2.15) can be simplified to

$$SNR \approx \eta_{tot} \frac{4q_I^2}{\pi} \bar{m}_S . \tag{2.16}$$

As can be seen in Eq. (2.16), the SNR of a DH system in the off-axis IPRG is expected to scale linearly with the strength of the signal. This means the a properly functioning DH system operates within a shot-noise-limited regime [20, 22].

2.2 Using infrared-wavelength sources in DH systems

To understand why it may be advantageous to use IR wavelengths for DH systems, it is necessary to understand the relevant atmospheric turbulence properties. Turbulence in the atmosphere is generated by temperature and pressure differences in adjacent regions of air, causing spatial and temporal variations in its refractive index [28]. Temporal variations are considered insignificant compared to the amount of time it takes for light to traverse a region of atmosphere,

so turbulence metrics tend to focus on the strength of spatial variation. Three of these metrics are the Fried coherence length, log-amplitude variance, and isoplanatic angle.

The Fried parameter, r_0, measures the distance light travels through the atmosphere before the root-mean-squared wavefront gains one radian of phase aberration [29]. It is directly proportional to wavelength such that

$$r_0 \propto \lambda^{6/5}. \tag{2.17}$$

From Eq. (2.17), a longer wavelength corresponds to a larger Fried parameter, and the farther light can propagate before experiencing more than a 2π radian phase change.

The log-amplitude variance, σ_χ^2, also known as the Rytov number, measures the strength of scintillation experienced by light along the propagation path [28]. It is inversely proportional to wavelength such that [29]

$$\sigma_\chi^2 \propto \lambda^{-7/6}. \tag{2.18}$$

From Eq. (2.18), all else equal, the log-amplitude variance is smaller for longer wavelengths. As a point of reference, branch points and cuts begin forming in earnest for log-amplitude variances greater than 0.25 [29].

The isoplanatic angle, θ_0, measures the largest angle, with respect to the light's origin, over which the optical path length does not differ significantly from the on-axis optical path length [28]. As with the Fried parameter, the isoplanatic angle is proportional to wavelength such that

$$\theta_0 \propto \lambda^{6/5}. \tag{2.19}$$

In regard to turbulence, a larger isoplanatic angle indicates a weaker turbulence. With this in mind, Eq. (2.19) states longer wavelengths are less affected by turbulence than shorter wavelengths.

Together, Eqs. (2.17)-(2.19) show why longer wavelengths are attractive to laser applications that require light to propagate over long swaths of atmosphere. For example, changing from a common visible wavelength, 532 nm, to a common short-wave IR wavelength, 1064 nm, leads to an increase in Fried parameter and isoplanatic angle of approximately 130% and a decrease in log-amplitude variance of approximately 55%. As propagation path and turbulence strength increase, increasing the wavelength may be necessary to accomplish mission goals.

These benefits related to turbulence, though, must be weighed against the limitations of IR detection technology. Visible-wavelength detectors are typically made with silicon while IR detectors are made of more complicated matrices of elements such as indium-gallium-arsenide, or InGaAs. The complexity of IR detector materials makes them more difficult and expensive to manufacture and process [30]. This has resulted in fewer technology maturation efforts, such that IR detectors have significantly higher noise floors than visible detectors. Higher noise floors negatively affect DH efficiencies [17]. Therefore, before IR laser sources can be used for DH applications, the performance of DH systems using IR sources must be quantified and compared to systems using visible-wavelength sources.

2.3 Ambiguity function

In the radar community, there is significant interest in analyzing a radar pulse after it has interacted with a surface. One way to perform such an analysis is to compare the potentially aberrated pulse with a reference pulse. By doing so, the aberrations imparted onto the original pulse by the surface can be calculated. This process is the basis for matched filtering [31].

An important extension of the matched filter introduces the effects of delayed pulses and a moving surface. The equation capturing these effects is called the ambiguity function [32-33]. The ambiguity function is defined as

$$\chi(\tau,\nu_D)=\int_{-\infty}^{\infty}U_R(t)U_S^*(t-\tau)e^{j2\pi\nu_D t}dt=\int_{-\infty}^{\infty}\tilde{U}_R^*(\nu)\tilde{U}_s(\nu-\nu_D)e^{-j2\pi\nu\tau}d\nu\,, \tag{2.20}$$

where τ is the temporal delay between the center of the pulses, ν_D is the Doppler-frequency shift caused by the moving surface, U_R is the reference pulse, U_S is the original pulse being used to investigate the surface, t is time, $\tilde{U}_R$ and $\tilde{U}_S$ are the complex-optical fields of the reference and signal pulses (in the frequency domain), respectively, and ν is frequency.

From the two-dimensional ambiguity function, one-dimensional cuts can be made. One cut of particular interest is along the temporal delay axis, also known as the zero-Doppler cut as the Doppler-frequency shift if set to zero [32]. This cut is of the form

$$\chi(\tau,0)=\int_{-\infty}^{\infty}U_R(t)U_S^*(t-\tau)dt=\int_{-\infty}^{\infty}\tilde{U}_R^*(\nu)\tilde{U}_s(\nu)e^{-j2\pi\nu\tau}d\nu\,. \tag{2.21}$$

Because the zero-Doppler cut of the ambiguity function describes the system response as a function of pulse delay, Eq. (2.21) will serve as the basis for characterizing SNR degradation as a function of imperfect pulse overlap for DH systems in the pulsed configuration.

III. Pulsed laser source digital holography efficiency measurements

The contents of this chapter, Appendix B, and Appendix C were published in *Applied Optics*, vol. 61, no. 16 on 25 May 2022 [34].

In this paper, a 1064 nm pulsed laser source and a short-wave infrared (SWIR) camera are used to measure the total-system efficiency associated with a digital-holography system in the off-axis image plane recording geometry. At zero path-length difference between the signal and reference pulses, the measured total-system efficiency (15.9%) is consistent with that previously obtained with a 532 nm continuous-wave laser source and a visible camera [Appl. Opt. 58, G19-G30 (2019)]. In addition, as a function of temporal delay between the signal and reference pulses, the total-system efficiency is accurately characterized by a new component efficiency, which is formulated from the ambiguity function. Even with multi-mode behavior from the pulsed laser source and substantial dark-current noise from the SWIR camera, system performance is accurately characterized by the resulting ambiguity efficiency.

3.1 Introduction

Digital-holography (DH) systems use the interference of light to boost a weak signal above the noise floor of a camera. They do so with the use of a strong reference. In turn, DH systems provide access to robust estimates of the complex-optical field [22]. These benefits make DH systems advantageous in long-range imaging scenarios [11-16, 35-36]. Such scenarios are often plagued with deep-turbulence conditions and low signal-to-noise ratios (SNRs) [6-9], which limit the effective ranges of DH systems. Thus, it is convenient to quantify system performance in terms of the total-system efficiency. This efficiency, in practice, is comprised of "component efficiencies," which speak to the individual sources that cause SNR loss.

Past efforts to quantify these aforementioned component efficiencies made use of continuous-wave (CW) laser sources and visible cameras [17-20]. Recall that with CW laser sources, the coherence length also limits the effective ranges of DH systems since system performance depends on the interference between the signal and reference. In turn, temporal-coherence requirements for analog-holography systems were evaluated in the 1960's (shortly after the invention of the laser) [37]. Also recall that with DH systems, the interference between the signal and reference is detected and digitized by the camera pixels, adding additional considerations, especially for applications involving atmospheric turbulence [21]. As such, recent work quantified the temporal-coherence efficiency for a DH system with a phase-modulated CW laser source and a visible camera [18]. The results found that small changes in the temporal coherence between the signal and reference can drastically change the total-system efficiency. This outcome is less concerning for laboratory applications like microscopy and medical imaging [23, 38-40], but is most concerning when using DH systems for field applications like long-range imaging [11-16, 35-36].

Using pulsed laser sources, as opposed to CW laser sources, introduces additional considerations for DH systems like the temporal delay between the signal and reference pulses, since the interference of light in this case requires that the pulses overlap in time. While pulsed laser sources have been used in the microscopy and medical-imaging communities since at least the late 1990's [23-25], there has been little published quantification of system performance in terms of the total-system efficiency. This paper addresses this shortcoming. It does so by formulating a new component efficiency—one that accurately characterizes system performance as a function of temporal delay between the signal and reference pulses. This new efficiency is

formulated from the ambiguity function, which is well known within the radar community [31, 41]. Consequently, this new efficiency is referred to here as the "ambiguity efficiency."

It is important to note that this paper uses a DH system with a 1064 nm pulsed laser source and a short-wave infrared (SWIR) camera. In effect, SWIR wavelengths provide better transmission through the atmosphere [26, 31]; thus, this switch in wavelength (compared with previous experiments [17-20]) moves DH systems that much closer to fieldable products. It also presents new challenges that were previously not an issue at visible wavelengths.

The results of this paper ultimately show that the total-system efficiency and its component efficiencies accurately characterize system performance. They do so even with multi-mode behavior from the pulsed laser source and substantial dark-current noise from the SWIR camera. For example, at zero path-length difference (ZPD) between the signal and reference pulses, the results show that the measured total-system efficiency is 15.9%. Such results are consistent with those previously obtained with a 532 nm CW laser source and a visible camera [17]. In addition, the results show that as a function of temporal delay between the signal and reference pulses, the total-system efficiency is accurately characterized by the ambiguity efficiency. Such results are novel yet build on previous experiments in a meaningful way [17-20].

In what follows, Section 3.2 formulates expressions for the SNR in terms of the total-system efficiency and its component efficiencies, including the ambiguity efficiency. Section 3.3 then discusses the data collection and processing needed to obtain measured values for the total-system efficiency and its component efficiencies. In Section 3.4, these measured values are compared to predicted values in two ways: (1) at ZPD between the signal and reference pulses and (2) as a function of temporal delay between the signal and reference pulses. The paper concludes in Section 3.5 with a summary of these comparisons.

3.2 Theoretical setup

Multiple DH recording geometries exist and, in practice, each has its own benefits [6-8, 21, 22]. Because of its simplicity in setup, the off-axis image plane recording geometry (IPRG) was used in this paper [6, 22]. An example of the off-axis IPRG is shown in Fig. 3.1.

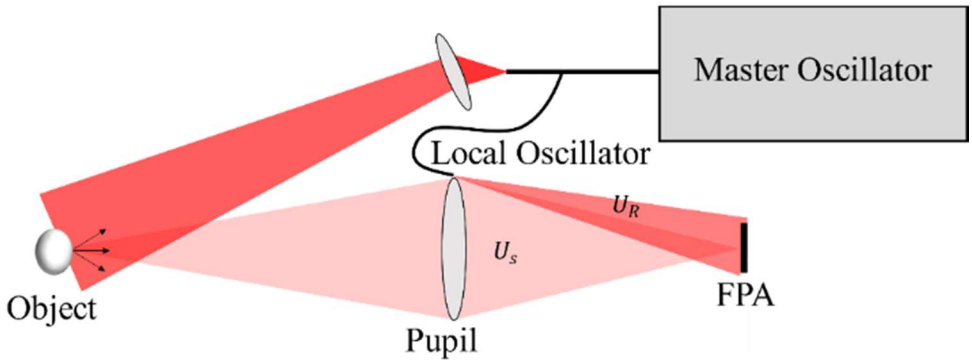

Figure 3.1. Example digital-holography system in the off-axis image plane recording geometry.

For the off-axis IPRG, the laser light from a master oscillator is split into two-optical paths. One path creates a signal by flood illuminating an optically rough, extended object. As shown in Fig. 3.1, the scattered-signal light is then collected by a lens and imaged onto the focal plane array (FPA) of a camera. The other path creates a reference by flood illuminating the FPA of a camera. By means of a local oscillator (LO), the strong-reference light is injected off axis relative to the pupil of the resulting imaging system.

It is important to note that the SNR of a DH system in the off-axis IPRG is dominated by the total-system efficiency. This efficiency can be seen in the following SNR formulation and in greater detail elsewhere [6, 22]. In practice, the total-system efficiency is the product of many component efficiencies, each of which quantifies a source of degradation in terms of system performance. Many component efficiencies have been developed and analyzed for DH systems with CW laser sources [17-21], but a new efficiency, called the ambiguity efficiency, is required

to fully characterize DH systems with pulsed laser sources. Thus, the ambiguity efficiency is formulated from the ambiguity function in this section.

3.2.1 Signal-to-noise ratio

This paper uses the power definition of the SNR [6, 22], such that

$$SNR(x,y) = \eta_{tot}(x,y)\frac{4q_I^2}{\pi}\frac{\bar{m}_S(x,y)\,\bar{m}_R}{\bar{m}_S(x,y)+\bar{m}_R+\sigma_n^2}, \tag{3.1}$$

where (x,y) are the estimated image-plane coordinates, η_{tot} is the total-system efficiency, q_I is the image-plane sampling quotient, $\bar{m}_S$ is the per-pixel mean number of signal photoelectrons, $\bar{m}_R$ is the mean number of reference photoelectrons, and σ_n^2 is the camera-noise variance, which is comprised of various camera-noise sources, such as read noise and dark-current noise.

Assuming the use of a strong reference, $\bar{m}_R \gg \bar{m}_S + \sigma_n^2$. In turn, Eq. (3.1) simplifies into the following expression [22]:

$$SNR(x,y) = \eta_{tot}(x,y)\frac{4q_I^2}{\pi}\bar{m}_S(x,y). \tag{3.2}$$

Such an expression says that the DH system is operating in a shot-noise-limited regime [20, 22].

3.2.2 Total-system efficiency

Ideally, the total-system efficiency η_{tot} is comprised of several multiplicative terms. Thus, it is assumed that no coupling exists between the various component efficiencies that make up the total-system efficiency. Each multiplicative term is then an independent source for SNR loss, such that

$$\eta_{tot}(x,y,\tau) = \eta_{ern}\eta_{snl}(x,y)\eta_{mix}(\tau) \tag{3.3}$$

where η_{ern} is the excess-reference-noise efficiency, $\eta_{snl}(x,y)$ is the shot-noise-limit efficiency, $\eta_{mix}(\tau)$ is the mixing efficiency, and τ is the temporal delay between the centers of the signal and reference pulses. It should be noted other component efficiencies could exist; however, they are beyond the scope of the present analysis.

The excess-reference-noise efficiency, η_{ern}, is a measure of the excess noise present in the reference [17, 20]. If the reference was perfectly uniform (with no excess amplitude noise [42]), then η_{ern}=100%. For simplicity, this paper assumes that η_{ern}= 100% for predicted values of η_{ern}.

The shot-noise-limit efficiency, $\eta_{snl}(x,y)$, is a quantification of the strong-reference assumption made in Eq. (3.2) [17, 20]. In a perfect experimental setup, $\eta_{snl}(x,y)$=100% but, in practice, excess signal noise caused by the pupil-autocorrelation term in the Fourier plane [see Fig. 3.3(b)], as well as camera noise, degrades this component efficiency. Thus, this paper assumes that

$$\eta_{snl}(x,y)=\frac{\bar{m}_R}{\bar{m}_R+\bar{m}_S(x,y)+\sigma_n^2} \tag{3.4}$$

for predicted values of η_{snl}.

The mixing efficiency, $\eta_{mix}(\tau)$, is a measure of how well the signal and reference pulses interfere as a function of τ. For DH systems using pulsed laser sources,

$$\eta_{mix}(\tau)=\eta_{pol}\eta_{mod}\eta_{amb}(\tau), \tag{3.5}$$

where η_{pol} is the polarization efficiency [17], η_{mod} is the modulation efficiency [21], and $\eta_{amb}(\tau)$ is the novel ambiguity efficiency.

For optically rough, extended objects with dielectric substrates, this paper assumes that η_{pol} is 50% because only half of the completely unpolarized scattered-signal light interferes with the completely polarized strong-reference light.

As discussed in Ref. [21], η_{mod} is a measure of how accurately the interference between the signal and reference is detected and digitized by the camera pixels. In this paper, η_{mod} is calculated using the square-pixel modulation transfer function, viz.

$$\eta_{mod} = \left\langle P\left(f_x - \alpha, f_y - \beta\right) \mathrm{sinc}^2\left(p f_x, p f_y\right) \right\rangle, \tag{3.6}$$

where $\langle \cdot \rangle$ denotes spatial average, P is a shifted pupil-filter function, $\left(f_x, f_y\right)$ are the Fourier-plane coordinates, $\left(\alpha, \beta\right)$ are the shifts, and p is the square-pixel width. In this paper, $\mathrm{sinc}\left(x\right) = 1$ when $x = 0$ and $\mathrm{sinc}\left(x\right) = \sin\left(\pi x\right)/\left(\pi x\right)$ otherwise [43, 44]. Additionally, $\left(\alpha = 0.196, \beta = 0.198\right)$ in units of inverse pixels and p = 15 μm. These properties, along with an assumed 100% pixel fill factor, results in η_{mod} = 75%.

The ambiguity efficiency, $\eta_{amb}\left(\tau\right)$, is a measure of the coherence between the signal and reference pulses and is formulated from the ambiguity function, $\chi\left(\tau\right)$. In practice [31, 41],

$$\chi\left(\tau, \nu_D\right) = \int_{-\infty}^{\infty} U_R\left(t\right) U_S^*\left(t - \tau\right) e^{j2\pi\nu_D\tau} dt = \int_{-\infty}^{\infty} \tilde{U}_R^*\left(\nu\right) \tilde{U}_s\left(\nu - \nu_D\right) e^{-j2\pi\nu\tau} d\nu, \tag{3.7}$$

where ν_D is the Doppler-frequency shift (caused by a moving object), U_R and U_S are the complex-optical fields of the reference and signal pulses (in the temporal domain), respectively, t is time, $\tilde{U}_R$ and $\tilde{U}_S$ are the complex-optical fields of the reference and signal pulses (in the frequency domain), respectively, and ν is frequency. However, this paper assumes that $\nu_D = 0$

because the optically rough, extended object is stationary. Therefore, $\chi(\tau, \nu_D)$ can be simplified to $\chi(\tau)$.

In accordance with the power definition of the SNR [see Eq. (3.1)], $\eta_{amb}(\tau) = |\chi(\tau)|^2$. Thus, $\eta_{amb}(\tau)$ simplifies to

$$\eta_{amb}(\tau) = \left| \int_{-\infty}^{\infty} U_R(t) U_S^*(t-\tau)\, dt \right|^2 = \left| \int_{-\infty}^{\infty} \tilde{U}_R^*(\nu) \tilde{U}_s(\nu) e^{-j2\pi\nu\tau} d\nu \right|^2. \tag{3.8}$$

This formulation assumes that there is spatial uniformity in the signal and reference pulses.

3.3 Experimental Setup

As shown in Fig. 3.2, the experimental setup made use of a 1064 nm pulsed laser source and a SWIR camera to create a digital-holography system in the off-axis IPRG. The goal of this experimental setup was to measure the total-system efficiency (1) at ZPD between the signal and reference pulses and (2) as a function of temporal delay between the signal and reference pulses. In turn, a custom-built NP Photonics Coherent High Energy Pulsed Fiber Laser System was used as the pulsed laser source [45].

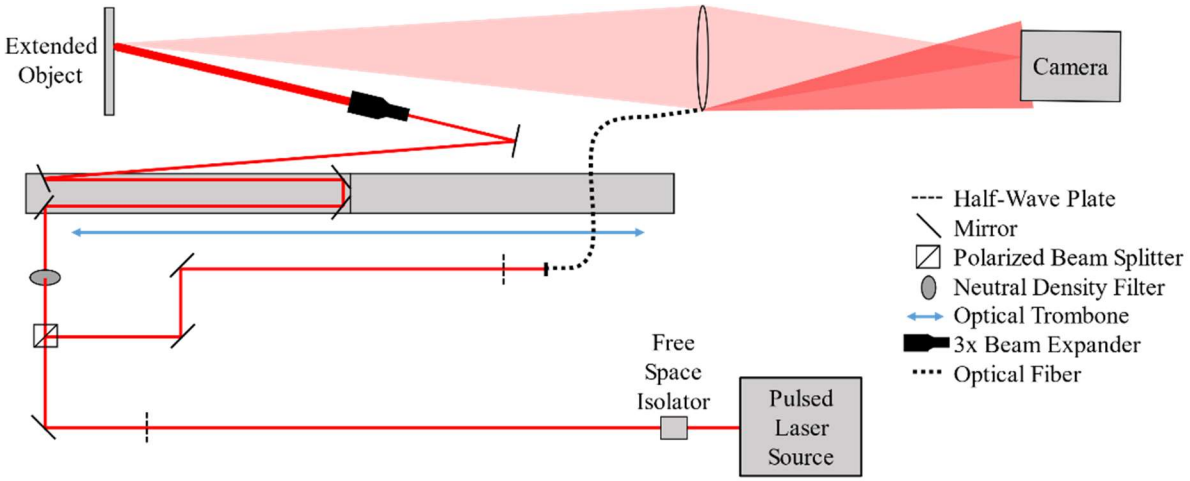

Figure 3.2. Overview of the experimental setup.

The pulsed laser source was comprised of a CW seed laser with a vendor-specified 1064 nm center wavelength and 5 kHz linewidth, high-speed phase and intensity modulators to carve out pulses from the CW seed laser, and multiple ytterbium-doped fiber amplifier stages. Together, this configuration produced 10 ns pulses with average energies of 10 μJ. The average energy per pulse fluctuated $\pm 16\%$ over a 15-minute time period, which was the amount of time required to collect one dataset.

As shown in Fig. 3.2, the pulse train from the pulsed laser source was sent through a half-wave plate before entering a polarized beam splitter (PBS). This PBS split the pulse train into reference and signal pulses. The average energy per pulse associated with the reference pulses was controlled by the half-wave plate before the PBS, while the average energy per pulse associated with the signal pulses was further reduced by a continuously variable neutral density filter with optical density values from 0.04 to 4.0. Such a filter allowed the experimental setup to avoid saturation of the camera pixels.

After the PBS, the signal pulses were sent through an optical trombone to control the amount of temporal delay between the signal and reference pulses at the camera. Thereafter, the signal pulses were expanded by a 3x beam expander and scattered off a sheet of Labsphere Spectralon (i.e., the stationary, optically rough, extended object) with a vendor-specified 99% Lambertian reflectivity, depolarizing the light. This unpolarized, scattered-signal light was then imaged onto a camera with a 2.54 cm diameter lens, which gave rise to a circular pupil. The object and image distances were set in order to obtain a measured image-plane sampling quotient, q_I, of 3.35 [6, 22]. By definition, q_I represents the number of circular-pupil diameters that can fit across the Fourier plane.

The reference pulses were sent through a second half-wave plate and fiber-coupling optics. This second half-wave plate aligned the linear polarization of the reference pulses with the slow axis of a 3 m polarization-maintaining, single-mode optical fiber. In accordance with the off-axis IPRG, the back-end tip of this fiber was placed next to the imaging lens. Thereafter, the reference pulses flood illuminated the FPA of the camera.

An Allied Vision Goldeye G-033 SWIR TEC1 was used for the camera. This camera had a vendor-specified pixel-well depth of 25,000 photoelectrons (pe), a pixel width of 15 μm, and a quantum efficiency of 77% at 1064 nm. This camera also had a measured unstable gain region for integration times less than 25 μs, which resulted in over 25% of the pixel-well depth being filled by dark-current noise. In turn, the experiment was set up for the signal and reference pulses to arrive near the 27 μs integration-time mark with a total frame-integration time of 30 μs. The dark-current noise was still the dominant factor in the camera-noise variance, σ_n^2. In total, $\sigma_n^2 = 6415$ pe^2.

To avoid saturation of the camera pixels, the mean number of reference and signal photoelectrons were set such that $\bar{m}_R = 11{,}784$ pe and $\bar{m}_S = 88$ pe. Because the camera-noise variance was over half the mean number of reference photoelectrons generated (i.e., $\sigma_n^2 > 1/2\,\bar{m}_R$), the strong-reference assumption made in Eq. (3.2) was not valid. As such, the DH system used in this experiment was not operating in a shot-noise-limited regime [20, 22]. By design, the total-system efficiency η_{tot} accounted for this shortcoming with its component efficiencies; in particular, the shot-noise-limit efficiency η_{snl} [see Eq. (3.4)].

3.3.1 Data collection and processing

Data collection occurred for temporal-delay values from τ = -6.5 ns to +4.5 ns in 1 ns increments and from τ = -1.2 ns to +0.5 ns in 0.1 ns increments. The negative values of τ correspond to a delay of the reference pulse with respect to the signal pulse. Conversely, the positive values of τ correspond to a delay of the signal pulse with respect to the reference pulse. For each increment of τ, the Labsphere Spectralon sheet was rotated to generate 10 distinct speckle realizations (for averaging during data processing). Furthermore, for each speckle realization, 10 digital-hologram frames, 10 signal-only frames, and 10 reference-only frames were collected, totaling 300 frames for each dataset (i.e., 30 total frames per speckle realization, for 10 speckle realizations). After the datasets were collected, 100 background frames were also taken, so that the background and camera noise could be appropriately accounted for during efficiency calculations.

The aforementioned frames were imported to MATLAB for data processing. The first step was frame demodulation. Figure 3.3 shows an example using a digital-holography frame.

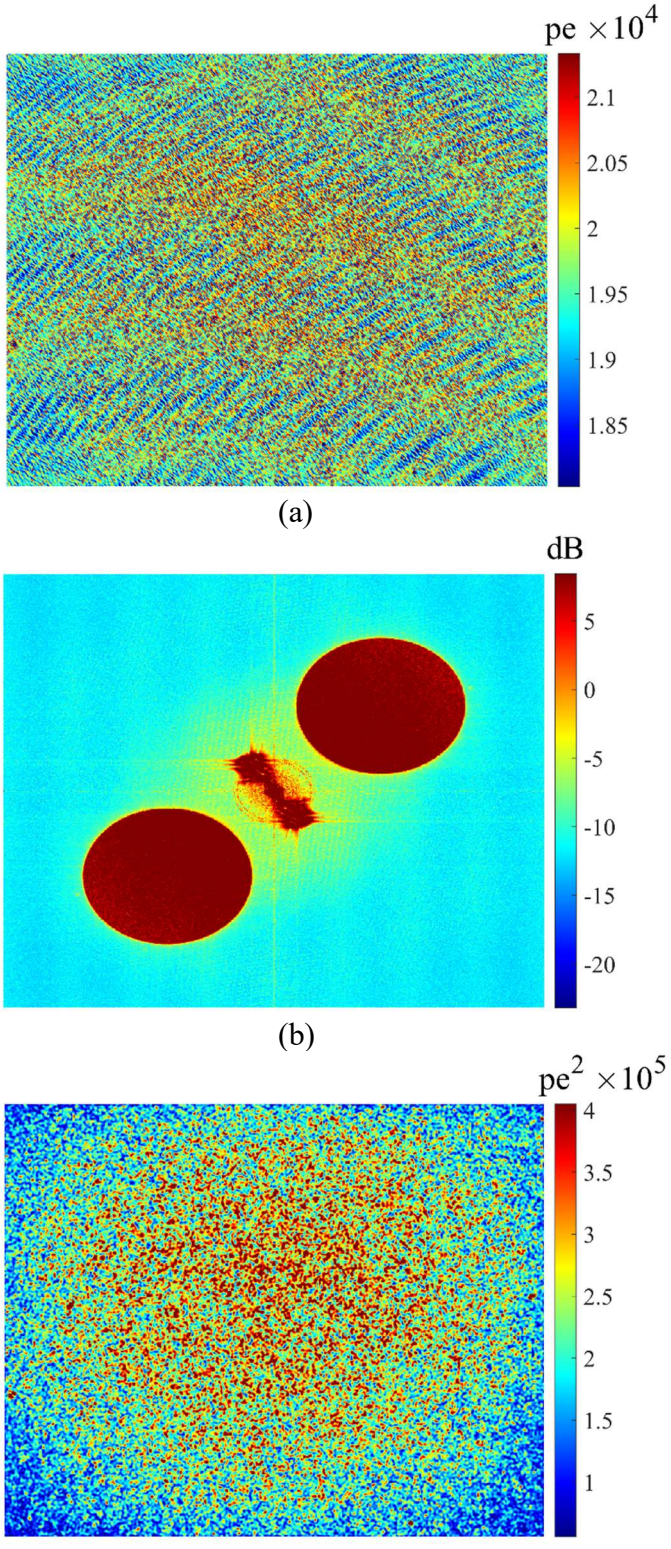

Figure 3.3. Frame-demodulation example. Here, the data processing involves (a) the recorded digital-hologram frame, (b) the associated Fourier plane, and (c) the associated image plane.

The real-valued digital-hologram frame in Fig. 3.3(a) underwent a discrete inverse Fourier transform to obtain the associated complex-valued Fourier plane in Fig. 3.3(b). In accordance with the off-axis IPRG, the Fourier plane contained four distinct terms.

(1) The signal term (the data in the top-right circular pupil)

(2) The complex-conjugate signal term (the data in the bottom-left circular pupil)

(3) The pupil-autocorrelation term (the circularly symmetric data centered at DC)

(4) The LO-autocorrelation term (the non-circularly symmetric data centered at DC)

Provided (1)-(4), a pupil-filter function was used to filter the desired signal term. To complete the frame demodulation, the filtered data was first centered in the Fourier plane, then subsequently underwent a discrete Fourier transform to obtain the associated complex-valued image plane in Fig. 3.3(c).

Frame demodulation was performed on each individual frame to avoid any piston-phase mismatch introduced on a frame-to-frame basis. The energies, or square magnitudes, of the demodulated frames in pe^2 were subsequently calculated in accordance with the power definition of the SNR [see Eq. (3.1)]. Then, the mean of all 100 demodulated energy frames was computed for each pulse delay, τ, to produce an average demodulated energy frame. This process was repeated for the collected signal-only, reference-only, and background-only frames using the same pupil-filter function as was used for the digital-hologram frames. Doing so ensured the noise collected by the hologram frames was appropriately accounted for within the analysis.

3.3.2 Measured total-system efficiency

The average energy frames at each pulse delay, τ, were used to calculate the measured total-system efficiency and its component efficiencies. For this purpose, it is convenient to define the following quantities:

$$E_H\left(x,y,\tau\right)=\left[\bar{m}'_R\left(x,y,\tau\right)-\bar{m}'_B\left(x,y,\tau\right)\right]\times\left[\bar{m}'_S\left(x,y,\tau\right)-\bar{m}'_B\left(x,y,\tau\right)\right], \tag{3.9}$$

$$E'_N\left(x,y,\tau\right)=E'_{D-R}\left(x,y,\tau\right)+E'_{D-S}\left(x,y,\tau\right)-E'_{D-B}\left(x,y\right), \tag{3.10}$$

and

$$E'_H\left(x,y,\tau\right)=E'_{D-H}\left(x,y,\tau\right)-E'_N\left(x,y,\tau\right), \tag{3.11}$$

where E_H is the hologram energy; $\bar{m}'_R$, $\bar{m}'_S$, and $\bar{m}'_B$ are the measured mean number of reference, signal, and background photoelectrons, respectively; E'_N is the measured noise energy; E'_{D-R}, E'_{D-S}, and E'_{D-B} are the measured reference, signal, and background energies after frame demodulation, respectively; E'_H is the measured hologram energy, and E'_{D-H} is the measured hologram energy after frame demodulation. Note that for Eqs. (3.9)-(3.11), the dependence on τ is caused by pulse-energy fluctuations within the datasets, not the pulse delay itself. Also note that the substantial dark-current noise from the SWIR camera is accounted for with $\bar{m}'_B$ and E'_{D-B}. In practice, both $\bar{m}'_R$ and $\bar{m}'_S$ contain this dark-current noise, which must be removed with background subtraction in order to calculate the desired energies in Eqs. (3.9) and (3.10). This background subtraction is explicit in Eq. (3.9). For Eq. (3.10), the measured noise energy is the sum of the reference, signal, and background energies. Since the measured reference and signal energies each contain the measured background energy, it is only subtracted once in Eq. (3.10).

Using Eqs. (3.9)-(3.11), the measured total-system efficiency, as well as the measured excess-reference-noise, shot-noise-limit, and mixing component efficiencies, respectively, were quantified as follows:

$$\eta'_{tot}\left(\tau\right)=\left\langle\frac{SNR'\left(x,y,\tau\right)}{SNR\left(x,y,\tau\right)}\right\rangle=\frac{\pi}{4q_I^2}\left\langle\frac{E'_H\left(x,y,\tau\right)/E'_N\left(x,y,\tau\right)}{\bar{m}'_S\left(x,y,\tau\right)-\bar{m}'_B\left(x,y,\tau\right)}\right\rangle. \tag{3.12}$$

$$\eta'_{ern}(\tau)=\frac{\pi}{4q_I^2}\frac{\left\langle \bar{m}'_R(x,y,\tau)-\bar{m}'_B(x,y,\tau)\right\rangle}{\left\langle E'_{D-R}(x,y,\tau)-E'_{D-B}(x,y,\tau)\right\rangle}, \tag{3.13}$$

$$\eta'_{snl}(\tau)=\frac{\left\langle E'_{D-R}(x,y,\tau)-E'_{D-B}(x,y)\right\rangle}{\left\langle E'_N(x,y,\tau)\right\rangle}, \tag{3.14}$$

and

$$\eta'_{mix}(\tau)=\left\langle \frac{E'_H(x,y,\tau)}{E_H(x,y,\tau)}\right\rangle. \tag{3.15}$$

As with Eqs. (3.9)-(3.11), Eqs. (3.12)-(3.15) gain a dependence on τ due to pulse-energy fluctuations, not the temporal delay itself. The $\pi/4q_I^2$ term in Eq. (3.14) is necessary to account for the ratio of the pupil-filter function area to the total Fourier plane area [6, 22]. In accordance with the off-axis IPRG, q_I accounts for the portion of the noise that is filtered from the Fourier plane by the pupil-filter function.

3.4 Results

This section compares the measured values [see Eqs. (3.9)-(3.15) in Section 3.3] to the predicted values [see Eqs. (3.3)-(3.8) in Section 3.2] for the total-system efficiency and its component efficiencies. It does so in two ways: (1) at ZPD between the signal and reference pulses and (2) as a function of temporal delay between the signal and reference pulses. Even with multi-mode behavior from the pulsed laser source and substantial dark-current noise from the SWIR camera, the results ultimately show that (1) at ZPD, they are consistent with those previously obtained with a 532 nm CW laser source and visible camera [17], and (2) as a function of temporal delay, they are accurately characterized by the ambiguity efficiency.

3.4.1 Results at ZPD

The results at ZPD with the 1064 nm pulsed laser source and SWIR camera were compared with those previously obtained with a 532 nm CW laser source and visible camera [17]. This comparison can be found in Table 3.1, which also shows the measured values, obtained using Eqs. (3.9)-(3.15), to the predicted values, obtained using Eqs. (3.3)-(3.8), for the total-system efficiency and its component efficiencies. It is important to note that the ambiguity efficiency, η_{amb}, is 100% at ZPD, so it is not included as a component efficiency in Table 3.1.

Table 3.1. Comparison of measured and predicted values for the total-system efficiency and its component efficiencies at ZPD.

Efficiency	CW Source ZPD, Measured	Pulsed Source ZPD, Measured	Pulsed Source ZPD, Predicted
Total-System, η_{tot}	25.6% ± 6.3%	15.9% ± 10.3%	24.2%
Excess-Ref.-Noise, η_{ern}	74.5% ± 2.0%	66.8% ± 1.6%	100.0%
Shot-Noise-Limit, η_{snl}	100% ± 0.0%	79.8% ± 15.6%	64.4%
Mixing, η_{mix}	36.8% ± 10.2%	29.2% ± 14.2%	37.5%

As shown in Table 3.1, the measured values for the total-system efficiency and its component efficiencies were lower with the 1064 nm pulsed laser source and SWIR camera than those previously obtained with a 532 nm CW laser source and visible camera [17]. These differences were attributed to multi-mode behavior from the pulsed laser source and substantial dark-current noise from the SWIR camera.

Appendix B uses pulse diagnostic measurements to show that the 1064 nm pulsed laser source produced at least two modes within the reference and signal pulses. Recall that with the off-axis IPRG, the reference pulses diverge onto the FPA of the camera, whereas the signal pulses converge (see Fig. 3.1). Therefore, the multiple modes in the signal and reference pulses were not aligned at the point of detection and digitization by the camera pixels. This modal mismatch

degraded the interference between the signal and reference, and contributed to the measured mixing efficiency being 8.3% less than the predicted mixing efficiency. Additionally, a pixel fill factor of 100% was assumed for the predicted mixing efficiency. If the fill factor was less than this ideal value, then the measured mixing efficiency would decrease accordingly.

Most SWIR cameras, including the one used in this paper, use indium gallium arsenide FPAs. These FPAs have inherently different noise properties than the silicon FPAs typically used in visible cameras. For example, in the CW experiment reported previously [17], the visible camera had a measured camera-noise variance of 5.5 pe^2 compared to a vendor-specified well depth of 10,482 pe. In the pulsed experiment reported here, the SWIR camera had a measured camera-noise variance of 6,415 pe^2 compared to a vendor-specified well depth of 25,000 pe. As a result, the DH system in the CW experiment was operating in a shot-noise-limited regime [20, 22], whereas the DH system in the pulsed experiment was not (i.e., both the measured and predicted shot-noise-limit efficiencies were significantly less than 100% for the DH system in the pulsed experiment).

The 15.4% increase between the measured and predicted values for the shot-noise-limit efficiency was primarily caused by the effects of excess-reference noise. Recall that such effects result from a non-uniform reference. Also recall that the predicted values obtained using Eq. (3.4) assumes that only shot noise from the reference is present, whereas the measured values obtained using Eq. (3.14) also takes into account the effects of excess-reference noise. As such, when measured values for the excess-reference-noise and shot-noise-limit efficiencies are multiplied together, the 53.3% obtained in the pulsed experiment reported here is less than the 74.5% obtained in the previously reported CW experiment. This outcome is due to substantial dark-current noise from the SWIR camera, which lead to the aforementioned increase in camera-noise variance. A secondary cause for the 15.4% increase was probably due to the previously discussed modal

mismatch between the signal and reference pulses. In general, this modal mismatch was not accounted for in the theoretical and experimental setups.

Despite the multi-mode behavior from the pulsed laser source and substantial dark-current noise from the SWIR camera, the predicted values for the total-system efficiency were within the uncertainty bounds of the measured values. This outcome serves as an indication that no coupling existed between the various component efficiencies that make up the total-system efficiency. In turn, the results at ZPD were consistent with those previously made with a 532 nm CW laser source and a visible camera [17].

3.4.1 Results as a function of temporal delay

The results as a function of temporal delay were first compared to the predicted values for the total-system efficiency. This comparison can be found in Fig. 3.4, which shows the measured values, obtained using Eq. (3.12), to the predicted values, obtained using Eq. (3.3), for the total-system efficiency. Here, the measured values, obtained using Eqs. (3.13)-(3.15), served as the component efficiencies in Eq. (3.3) (i.e., $\eta_{tot} = \eta'_{ern}\eta'_{snl}\eta'_{mix}$).

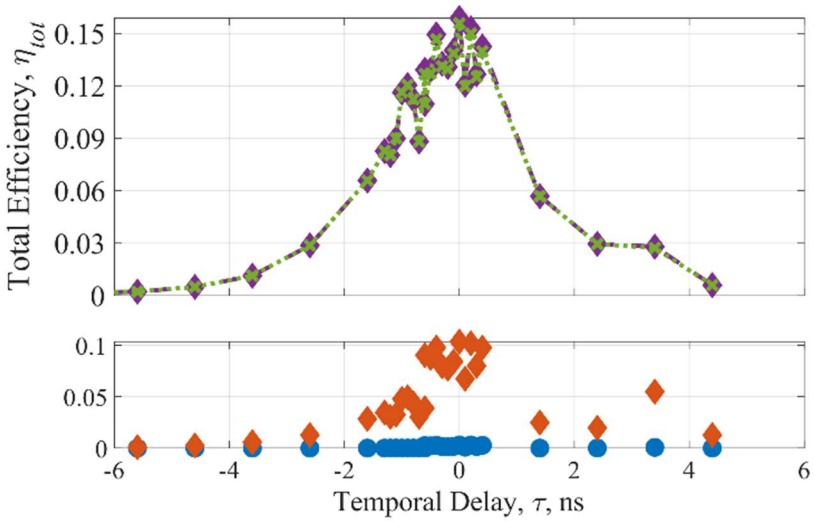

Figure 3.4. Comparison of the measured (-♦) and predicted (··×) values for the total-system efficiency as a function of temporal delay (top), with residuals (•) and measured uncertainties (♦) also as a function of temporal delay (bottom).

As shown in Fig. 3.4, the residuals were less than the measured uncertainties at each temporal-delay value. This outcome served as another indication that no coupling existed between the various component efficiencies that make up the total-system efficiency. If a coupling between component efficiencies had been introduced within the experiment, then the total-system efficiency would not be the multiplicative product of the component efficiencies and the residuals would have exceeded the measured uncertainties.

With the outcomes of Table 3.1 and Fig. 3.4 in mind, the results as a function of temporal delay were then compared to predicted values for the ambiguity efficiency. This comparison can be found in Fig. 3.5, which shows the measured values, obtained using Eq (3.12), to the predicted values, obtained using Eq. (C.3) in Appendix C, for the total-system efficiency. To formulate Eq. (C.3) in Appendix C, the pulse diagnostic measurements from Appendix B were used to inform a multi-mode fit to the ambiguity efficiency formulated in Section 3.2 [see the right-most term in Eq. (3.8)]. For convenience, Eq. (C.3) is repeated here, viz.

$$\eta_{amb}(\tau) = A_1^2 \Delta\nu^4 \, exp\left(-4\pi\Delta\nu|\tau|\right) + A_2^2 \Delta\nu^4 \, exp\left(-4\pi\Delta\nu|\tau|\right), \tag{3.16}$$

where A_1 is the amplitude of the fundamental mode, $\Delta\nu$ is the half width, half maximum of the assumed Lorentzian line shape, τ is again temporal delay, and A_2 is the amplitude of the transverse mode (see Table C.1 in Appendix C for the multi-mode fit parameters). For simplicity, the spectrum was assumed to be comprised of two modes of the same width, and each mode was assumed to have a Lorentzian line shape. To characterize the total-system efficiency as a function of τ, the predicted values from Eq. (3.16) for the ambiguity efficiency were multiplied by the measured total-system efficiency at ZPD (see Table 3.1).

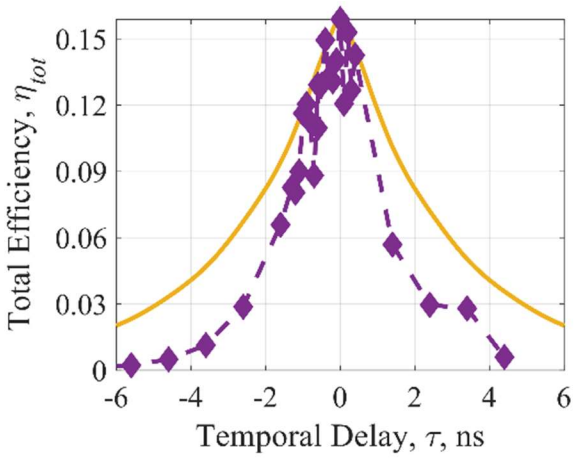

Figure 3.5. Comparison of the measured values for the total-system efficiency (-♦) to the predicted values for the total-system efficiency (–) using a multi-mode fit to the ambiguity efficiency.

As shown in Fig. 3.5, the measured values for the total-system efficiency matched the predicted values for the total-system efficiency well for $|\tau| < 1$ ns. There were many possibilities for what might have caused the overestimation for $|\tau| > 1$ ns. One strong possibility is attributed to improperly accounting for multi-mode effects in the predicted values for the ambiguity efficiency.

It is important to remember that Fabry-Perot interferometers have system line shapes so any measurement reported by these devices is the convolution of this system line shape and the spectral line shape of the incident pulse train. The model used in this paper assumed two modes existed, but the convolution with the Fabry-Perot interferometer line shape may have hidden spectral features, such as additional modes or phase interruptions present within the incident pulse train. Such features could have been masked by small misalignments while measuring the spectral line shape with the Fabry-Perot interferometer.

The Lorentzian line shapes used to represent the spectrum were also not completely accurate. For example, Fig. C.1(b) in Appendix C shows how different spectral line shapes affect the ambiguity efficiency curve. A more accurate fit to the spectral data would most likely result in

more accurate predicted values for the ambiguity efficiency, particularly for $|\tau| > 1$ ns. In addition, the modes were assumed to be independent from one another, but such independence was not verified in the experiment. Dependence between modes would have caused oscillations within the envelope of the predicted values for the ambiguity efficiency, and the depth of modulation within the envelope would have been proportional to the degree of dependence and the mode amplitudes.

The multi-mode pulsed laser source also resulted in a pulse train without perfect transverse coherence, meaning the spectral content in the signal and reference pulses were different across their respective wavefronts. The Fabry-Perot interferometer, being a 1-dimensional measurement device, did not captured this lack of transverse coherence. As mentioned for Eq. (3.8), spatial non-uniformity was not captured in the predicted values for the ambiguity efficiency and would negatively affect the predicted values for the total-system efficiency. The variation in intensity is also greater than the mean intensity for multi-mode sources [42, 46]. This last point was supported by the variation in measured total efficiency near $\tau = 0$ and could have caused a disproportionate decrease in SNR as the hologram energy approached the total-noise floor of the camera.

3.5 Conclusion

In this paper, a 1064 nm pulsed laser source and a SWIR camera were used to measure the total-system efficiency associated with a digital-holography system in the off-axis image plane recording geometry. At zero path-length difference between the signal and reference pulses, the measured total-system efficiency (15.9%) and its component efficiencies, including the excess-reference-noise efficiency (66.8%), shot-noise-limit efficiency (79.8%), and mixing efficiency (29.2%), were consistent with those previously obtained with a 532 nm continuous-wave laser source and a visible camera [17]. In addition, as a function of temporal delay between the signal

and reference pulses, the total-system efficiency was accurately characterized by a new component efficiency, which was formulated from the oft-used ambiguity function from the radar community. Even with multi-mode behavior from the pulsed laser source and substantial dark-current noise from the SWIR camera, system performance was accurately characterized by the resulting ambiguity efficiency.

IV. Digital-holography efficiency measurements using a heterodyne-pulsed configuration

The contents of this chapter was submitted to *Optical Engineering* on 09 August 2022 [47].

A digital-holography (DH) system is created in a heterodyne-pulsed configuration, meaning the reference and signal pulses are non-deterministically correlated in time. Using the off-axis image plane recording geometry, two performance metrics are measured: (1) the total-system efficiency and (2) the ambiguity efficiency. These metrics are compared against the same measured efficiencies for a DH system in a homodyne-pulsed configuration, which uses deterministically correlated reference and signal pulses. The total-system efficiency of both systems is found to be consistent with one another, showing that no new component efficiencies are required when switching from a homodyne- to a heterodyne-pulsed configuration. Additionally, an instantaneous phase modulation model is used to characterize system performance in terms of non-ideal pulse overlap. Such a model validates the use of the ambiguity efficiency for future efforts.

4.1 Introduction

Digital-holography (DH) systems can be designed to operate in long-range imaging scenarios that give rise to low-light and deep-turbulence conditions [6-9, 22]. Such systems involve the digitization of a spatial-modulation pattern or "hologram" created via the interference of two fields of light [10]. These fields are referred to here as the reference and signal. From the recorded digital hologram, an estimate of the complex-optical field can be made, which in terms of amplitude and wrapped phase contains information about the aberrations that are distributed along the propagation path. Therefore, researchers are currently studying ways to improve long-range imaging performance using DH systems [11-16].

The signal-to-noise ratio (SNR) is a key performance metric in terms of understanding the limitations of DH systems. This understanding requires the quantification of individual sources of SNR loss, otherwise known as efficiencies. The efficiencies of DH systems using continuous-wave (CW) laser sources have been extensively studied [17-21], and the success of these systems is largely due to the long coherence lengths of modern-day CW laser sources. Nevertheless, as the path-length differences between the signal and reference exceed the coherence length of the CW laser source, system performance degrades rapidly [18]. This outcome says that the effective ranges of DH systems in a CW configuration is limited by longitudinal coherence.

Using pulsed laser sources circumvents the limitations associated with the coherence length of CW laser sources, allowing for longer effective ranges using DH systems in a pulsed configuration. However, pulsed laser sources introduce additional considerations, such as the temporal overlap of the fields of light being interfered. To this end, the effect of temporal delay between the reference and signal pulses was recently studied using a 1064 nm pulsed laser source and a short-wave infrared (SWIR) camera [34]. This study showed that the efficiencies were comparable to those of a DH system in a CW configuration. It also introduced a novel efficiency, called the ambiguity efficiency, to capture the effects of reduced pulse overlap. In turn, this paper seeks to expand the understanding of DH systems (specifically in a pulsed configuration) in two ways.

The first way increases the applicability of DH systems. In Ref. [34], the two fields of light being interfered were deterministically correlated, since a post-amplification beam splitter was used to create the signal and reference pulses from a single pulse train. This idealization isolated the effect of reduced pulse overlap by ensuring the temporal characteristics of the reference and

signal pulses were identical before interaction with the experiment. Thus, this configuration is referred to as the "homodyne-pulsed configuration" throughout this paper.

For applications like long-range imaging, it is beneficial to analyze performance using signal and reference pulses with non-identical temporal characteristics. This configuration is referred to as the "heterodyne-pulsed configuration" throughout this paper. By eliminating the identical-field constraint, the heterodyne-pulsed configuration increases the applicability of DH systems, since a pre-amplification beam splitter can be used to create the signal and reference pulses from two-independent pulse trains. That or a single pulse train can be used with one pulse being one field and a subsequent pulse being the other. In both cases, the effective strengths of the pulses can be set within the dynamic range of the camera, and the timing of the pulses can be externally triggered to maximize pulse overlap. Both outcomes are desirable for applications like long-range imaging.

Ideally, DH systems operate in a shot-noise-limited regime [6, 20]; however, when this is not the case, system performance is impacted and must be thoroughly characterized in terms of the component efficiencies that make up SNR loss, as is done in this paper. In so doing, this paper shows that the measured efficiencies in a homodyne- and heterodyne-pulsed configuration are consistent with one another; therefore, no new component efficiencies are required to characterize system performance.

The second way shows that the ambiguity efficiency sufficiently accounts for non-ideal pulse overlap. In Ref. [34], the predicted ambiguity efficiency matched the measured ambiguity efficiency well only when the temporal delay between the reference and signal pulses was small. For large temporal delays, the model over predicted system performance. Multiple potential reasons were given in Ref. [34], but none were explored in depth. As a result, this paper goes

further and builds off a recent conference proceeding [48], which formulated more sophisticated models (specifically for the homodyne-pulsed configuration).

In support of the ambiguity efficiency and the heterodyne-pulsed configuration, this paper formulates a model in terms of an instantaneous phase modulation. A phase modulation could result from many issues within the laser source but the effect on the ambiguity efficiency will be the same. Therefore, this paper will investigate an instantaneous carrier frequency change or "mode hop" within the fields of light. The ambiguity efficiency is predicted for simple heterodyne fields both with and without a mode hop included in the model. Overall, the phase modulation leads to a more accurate ambiguity efficiency prediction, showing that the ambiguity efficiency sufficiently accounts for non-ideal pulse overlap.

Before proceeding, it is worth noting that work has been performed to characterize the temporal coherence of pulsed laser sources and their associated effects [49-53]. At large, the underpinning theory, modeling and simulation, and experiments assumed cycloergodicity [50-52]. In other words, the pulses were temporally and spatially identical for all time, resulting in no frame-to-frame variations in the recorded digital holograms. However, by definition, DH systems in a pulsed configuration do not satisfy the cycloergodicity condition. The non-identical temporal characteristics, such as the phases or spectral content, of the reference and signal pulses lead to substantial variations in the in the recorded digital holograms. As a result, the second order moment, or variance, of the associated pulses is non-zero.

Limited coherence theory has been developed for non-cycloergodic pulses and relies on nearly incoherent sources and long integration times [53]. On the other hand, DH systems in a pulsed configuration require partially coherent sources and nearly instantaneous measurements.

Therefore, the work presented in this paper goes significantly past previous efforts and validates temporal-coherence theory for non-cycloergodic pulses via the ambiguity efficiency.

In what follows, this paper begins with a review of the applicable efficiencies in Section 4.2. Section 4.3 then details the experiment, including the data-collection and data-processing methodologies. The results from the heterodyne experiment and the effect of an instantaneous phase modulation are presented in Section 4.4, along with a brief discussion concerning the impact of these results. A summary of the results conclude this paper in Section 4.5.

4.2 Theory

While multiple DH recording geometries exist [6-8, 21, 22], the off-axis image plane recording geometry (IPRG) was used in this paper because of its simplicity in setup [6, 15-21, 34]. An example of the off-axis IPRG is shown in Figure 4.1.

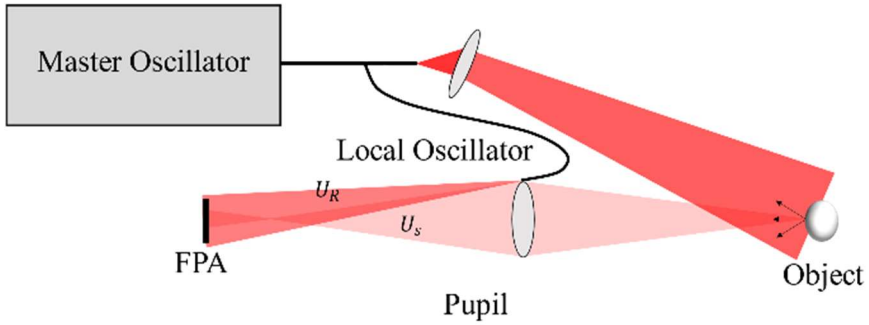

Figure 4.1. Example of the off-axis image plane recording geometry.

For the off-axis IPRG, light from a master oscillator is split into two optical paths. One optical path scatters light off an optically rough, extended object, as shown in Fig. 4.1. The scattered signal is collected by the pupil of an imaging system to create the signal field, U_S, and imaged onto the focal plane array (FPA) of a camera. The other optical path creates a reference field, U_R, by flood illuminating the FPA. The strong reference is injected off axis, relative to the pupil, via a local oscillator (LO).

4.2.1 Total-system and ambiguity efficiencies

In conjunction with the off-axis IPRG, this paper uses the power definition of the SNR [6, 9, 48], such that

$$SNR(x,y,\tau)=\eta_{tot}(x,y,\tau)\frac{4q_I^2}{\pi}\bar{m}_S(x,y), \tag{4.1}$$

where (x,y) are the estimated image-plane coordinates, τ is the temporal delay between the centers of the reference and signal pulses, η_{tot} is the total-system efficiency, q_I is the image-plane sampling quotient, and $\bar{m}_S$ is the mean number of signal photoelectrons generated by the signal pulse. It should be noted Eq. (4.1) assumes the reference is sufficiently strong such that the noise in the reference pulse dominates all other noise sources. In other words, Eq. (4.1) says the DH system is operating in the shot-noise-limited regime [6, 20]. However, if the DH system is not operating at the shot-noise limit, all detrimental effects are captured by η_{tot} and Eq. (4.1) remains valid.

Analyzing η_{tot} more closely, the total-system efficiency is the product of many independent sources of SNR degradation such that [17, 34]

$$\eta_{tot}(x,y,\tau)=\eta_{ern}\eta_{snl}(x,y)\eta_{mix}(\tau), \tag{4.2}$$

where η_{ern} is the excess-reference-noise efficiency, η_{snl} is the shot-noise-limit efficiency, and η_{mix} is the mixing efficiency. The excess-reference-noise efficiency quantifies the spatial uniformity of the reference field, and the shot-noise-limit efficiency quantifies the strong-reference approximation made in Eq. (4.1). Both efficiencies are described in detail elsewhere [17, 20, 34] and are not of primary concern in this paper.

The mixing efficiency, however, merits additional consideration, since it quantifies of how well the reference and signal pulses interfere. In general,

$$\eta_{mix}(\tau) = \eta_{pol}\eta_{mod}\eta_{amb}(\tau), \tag{4.3}$$

where η_{pol} is the polarization efficiency [17], η_{mod} is the modulation efficiency [21], and η_{amb} is the ambiguity efficiency [34]. The polarization efficiency is the quantification of how well the polarization axes of the reference and signal pulses align and the modulation efficiency is a quantification of how well the finite pixels of the FPA record the continuous hologram. As with η_{ern} and η_{snl}, η_{pol} and η_{mod} are discussed in detail elsewhere [17, 21, 34] and are not of primary concern in this paper.

On the other hand, η_{amb} is a main focus of this paper as it is the only efficiency dependent on the temporal overlap between the reference and signal pulses. The ambiguity efficiency is derived from the zero-Doppler cut of the ambiguity function [31, 32, 41], such that

$$\eta_{amb}(\tau) = \left\langle \left| \int_{-\infty}^{\infty} U_R(x,y,t) U_S^*(x,y,t-\tau)\, dt \right|^2 \right\rangle = \left\langle \left| \int_{-\infty}^{\infty} \tilde{U}_R^*(x,y,\nu) \tilde{U}_S(x,y,\nu) e^{j2\pi\nu\tau}\, d\nu \right|^2 \right\rangle, \tag{4.4}$$

where U_R and U_S are the complex-optical fields of the reference and signal pulses in the temporal domain, respectively, t is time, $\tilde{U}_R$ and $\tilde{U}_S$ are the complex-optical fields of the reference and signal pulses in the spectral domain, respectively, ν is frequency, $*$ denotes the complex conjugate, $|\bullet|^2$ is the square-magnitude operator, and $\langle \bullet \rangle$ is the spatial average operator. The square magnitude operator is necessary as, again, Eq. (4.1) uses the power definition for SNR. The spatial average operator is not required in Eq. (4.4), but it is convenient to have spatially independent metrics when cross evaluating multiple DH systems and is thus used here.

4.2.1 Discussion of the ambiguity efficiency

While the ambiguity efficiency captures the SNR degradation caused by temporal misalignment of the fields, caution must be taken when using Eq. (4.4) to predict DH system

performance (specifically in a pulsed configuration). Measuring the temporal or spectral fields for optical wavelengths is non-trivial. Many common non-imaging optical measurement devices, such as fast photodiodes and Fabry-Perot interferometers, only directly measure irradiance. The field is then estimated from irradiance, meaning much of the wrapped phase information is lost. This loss could lead to important phase-related artifacts being hidden within the measurements. In turn, the ambiguity efficiency predictions made from these measurements are inaccurate.

One such phase-related artifact, an instantaneous phase modulation, is investigated in this paper. A phase modulation could be caused by many factors and is indistinguishable from simultaneous multimode propagation when using common frequency measurement devices such as a Fabry-Perot interferometer. However, assuming the incorrect form of multi-modal laser operation results in an inaccurate ambiguity efficiency prediction.

It should be noted that most non-imaging optical temporal and spectral measurement devices only provide a measurement at a single spatial point (e.g., on axis), so the transverse coherence between the reference and signal fields is also lost. Including non-ideal transverse coherence would cause the predicted ambiguity efficiency to narrow, but this dynamic is not investigated in this paper. Furthermore, the temporal and spatial averaging of the measurement devices could also influence the predicted ambiguity efficiency. The model used to investigate the effect of an instantaneous phase modulation does not consider this dynamic either, as these engineering concerns fall outside the scope of this paper.

4.3 Experiment

As shown in Fig. 4.2, a DH system was set up with a 1064 nm pulsed laser source and a SWIR camera in the off-axis IPRG. The laser source was a custom-built NP Photonics Coherent High Energy Pulsed Fiber Laser System [45]. This laser source was set up in a heterodyne-pulsed

configuration, such that the signal and reference pulses were created from two-independent pulse trains in a master oscillator power amplifier or "MOPA" configuration. In practice, other heterodyne-pulsed configurations exist but the conclusions reached in this paper hold for them as well.

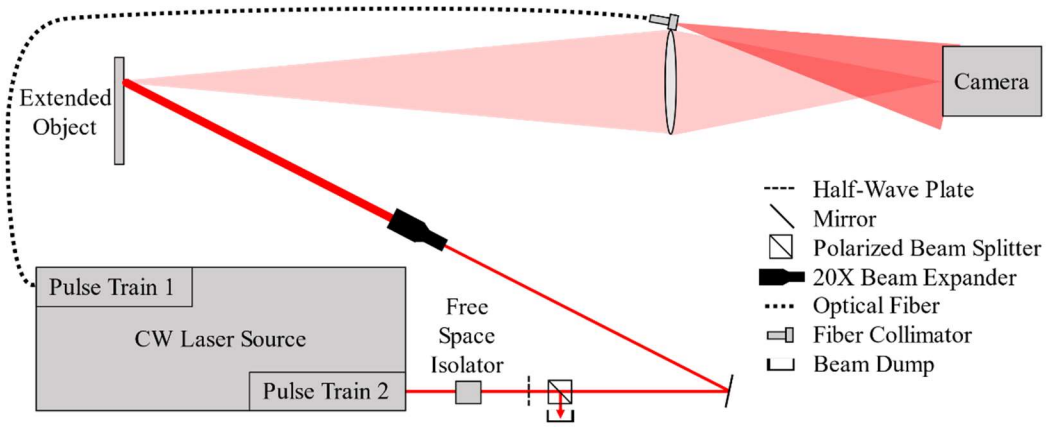

Figure 4.2. Experimental setup overview.

To create the two-independent pulse trains, a pre-amplification beam splitter was used after the CW seed laser (i.e., master oscillator) with a 1064 nm center wavelength. After the beam splitter, each beam was independently intensity modulated, then amplified via independent ytterbium-doped fiber amplifier stages. The independence of the intensity modulation and amplification stages is the fundamental difference between the heterodyne experiment presented here and the homodyne experiment presented in Ref. [34]. Both pulse trains produced pulses at a 1 kHz repetition rate.

Pulse train 1 produced 8.8 ns pulses with an average energy of 10 nJ. The resulting reference pulses exited the backend tip of a 2 m long polarization-maintaining, single-mode optical fiber. The backend tip was placed off axis next to the imagining lens and tilted towards the camera. An adjustable collimator was also used to ensure enough energy from the reference pulses was captured by the camera while maintaining a nearly uniform energy distribution over the camera's FPA.

Pulse train 2, on the other hand, produced 10 ns pulses with an average energy of 10 μJ. The resulting signal pulses passed through a free-space isolator, half-wave plate, and polarized beam splitter (PBS). The half-wave plate and PBS were used to control the energy of the signal pulses to avoid camera-pixel saturation, as discussed later. After the PBS, the signal pulses were sent through a 20x beam expander, scattered off a sheet of Labsphere Spectralon (i.e., the stationary, optically rough, extended object) with a vendor-specified 99% Lambertian reflectivity, and imaged onto the camera via a 2.54 cm imaging lens. It should be noted the object and image distances were set such that the measured image-plane sampling quotient, q_I, was 3.35 [9, 22]. By definition, q_I represents the number of circular-pupil diameters that can fit across the Fourier plane.

The spectral line shapes of the reference and signal pulses were measured using a Thorlabs SA200-8B scanning Fabry-Perot interferometer with a 7.5 MHz resolution and 1.5 GHz free spectral range, and are shown in Fig. 4.3 [54, 55], respectively.

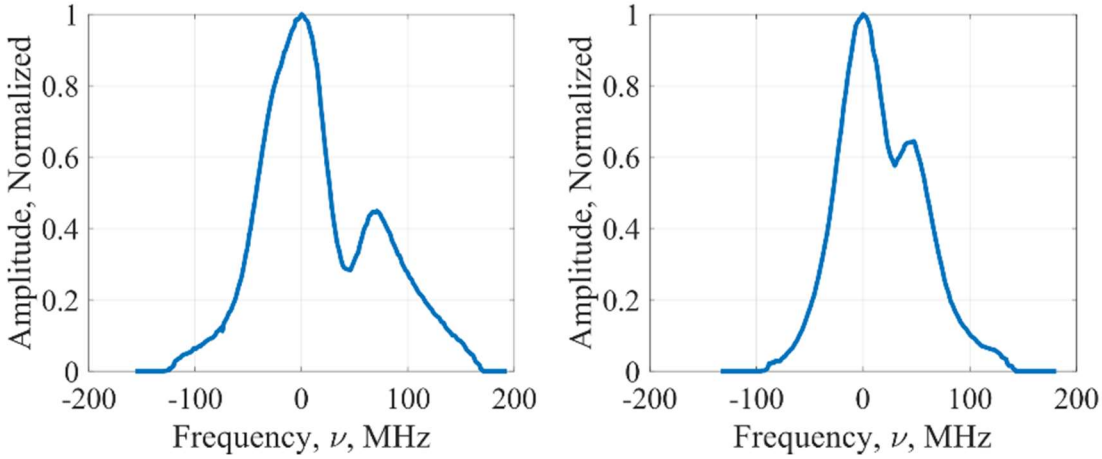

Figure 4.3. Spectral line shapes of the (a) reference and (b) signal pulses.

It was evident from the line shapes shown in Fig. 4.3 that the two-independent pulse trains were operating sub-optimally. For example, at least two modes were visible in both line shapes.

Subsequent spatial beam profile measurements confirmed the multi-mode nature of the pulses [34]. Analysis showed the larger of the two modes in each line shape, or the fundamental mode, was consistent with a Laguerre-Gauss ($p = 0, l = 0$) mode. Furthermore, the smaller of the two modes, or the secondary mode, was consistent with a Laguerre-Gauss ($p = 1, l = 0$) mode. From the laser construction parameters, the total spacing between these two modes was determined to be on the order of 1.5 GHz [34, 45]. This outcome means one mode had been aliased onto the other due to the limitations of the Fabry-Perot interferometer.

In addition to multi-mode operation, the line shapes and widths in Fig. 4.3 were not consistent with Fourier-transform limited pulses. This outcome, paired with differences in mode shape, width, and relative spacing for the reference and signal line shapes, indicated the pulse shaping and amplification processes were negatively affecting the line shapes in different ways. These differences may have been caused by a myriad of reasons, including unequal dispersion along independent propagation paths or non-uniform spatial sampling within the gain media.

The average energy from the two-independent pulse trains fluctuated $\pm$ 16% pulse to pulse consistently over a 6-hour time period, over twice as long as required to collect all necessary data. Therefore, the energy in each pulse was considered stable. The temporal overlap between the reference and signal pulses at the camera FPA was controlled during the intensity modulation process using a Berkeley Nucleonics Corporation Model 577 Digital Delay/Pulse Generator. This experimental nob allowed the total-system efficiency to be measured as a function of relative pulse delay, τ , with a minimum sampling resolution of 250 ps and a root-mean-squared jitter of 100 ps. All optical elements used in the experimental setup were either achromatic or coated to maximize transmission or reflection.

The camera was an Allied Vision Goldeye G-033 SWIR TEC1, exhibiting a pixel-well depth of 25,000 photoelectrons (pe) and a quantum efficiency of 77% at 1064 nm. This camera also had a measured unstable gain region for integration times less than 25 μs, resulting in over a quarter of the pixel-well depth being filled by dark-current noise. In turn, the dark-current noise was the dominant factor in the camera-noise variance, σ_n^2. Overall, σ_n^2 = 6,419 pe^2. Due to the unstable gain region, the experiment was set up for the reference and signal pulses to arrive near the 27 μs integration-time mark with a total frame-integration time of 30 μs.

Because of the high dark-current noise, the mean number of photoelectrons generated by the reference and signal pulses, $\bar{m}_R$ and $\bar{m}_S$ respectively, were set to $\bar{m}_R$ = 11,449 pe and $\bar{m}_S$ = 77 pe to avoid camera-pixel saturation, yet maximize sensing. Assuming Poisson statistics, where the mean is equal the variance, this outcome meant the reference pulses did not dominate all noise sources, as $\sigma_n^2 > 1/2\,\bar{m}_R$. Therefore, the DH system used in this experiment was not operating in the shot-noise-limited regime [20, 22]. As a reminder, this shortcoming was accounted for by the shot-noise-limit efficiency η_{snl} [see Eq. (4.2)]. For the system presented above, $\eta_{snl} = 81\%$.

4.3.1 Data-collection methodology

Digital holograms were collected for temporal pulse delay values from τ = -5.875 ns to +6.125 ns in 1 ns increments and from τ = -1.875 ns to +2.125 ns in 0.25 ns increments to sufficiently sample both the wings and the peak of the total-system efficiency curve. Two measurements were taken at τ = 0, one at the beginning of the overall data collection period and one at the halfway mark, to ensure the master oscillator and amplification paths were performing consistently for all datasets. For each measurement increment, the Labsphere Spectralon sheet was rotated to generate 10 distinct speckle realizations. For each speckle realization, 10 digital-hologram frames were collected for a total of 100 digital-hologram frames for each temporal pulse

delay value. This was done for averaging during data processing. Additionally, 10 reference-only frames and 10 signal-only frames were collected for each speckle realization during both $\tau = 0$ measurements. Reference-only and signal-only frames were unnecessary for all temporal delay values because the energy of both pulse trains was considered stable. After all frames were collected, 100 background frames were collected so the background and camera noise could be appropriately accounted for during efficiency calculations. All frames were imported to MATLAB for processing.

4.3.2 Data-processing methodology

In order to calculate the total-system and ambiguity efficiencies, the collected frames were first demodulated. An example using a digital-hologram frame is shown in Fig. 4.4.

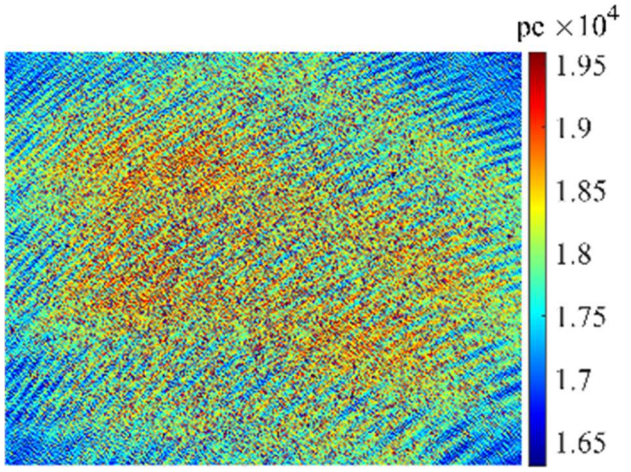

(a)

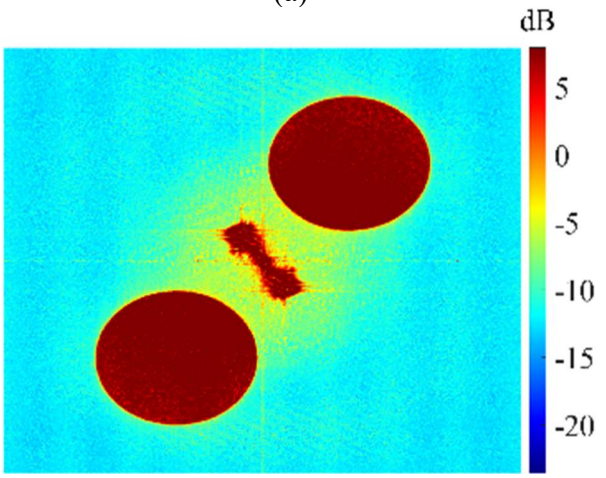

(b)

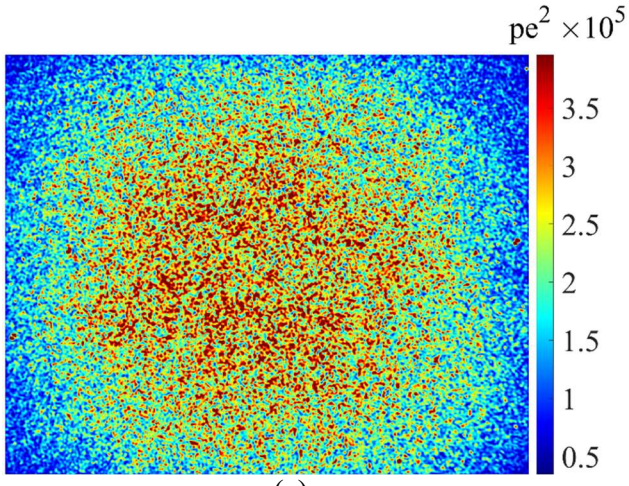

(c)

Figure 4.4. Frame-demodulation example using a digital-hologram frame. The demodulation process involves (a) the recorded frame, (b) the associated Fourier plane, and (c) the associated image frame.

For the example provided, a discrete inverse Fourier transform was performed on the real-valued digital hologram in Fig. 4.4(a) to obtain the associated complex-valued Fourier plane in Fig. 4.4(b). The Fourier plane, in accordance with the off-axis IPRG [22], contained four important terms:

(1) The signal field (the data in the top-right circular pupil),

(2) The complex-conjugate of the signal field (the data in the bottom-left circular pupil),

(3) The LO-autocorrelation (the non-circularly symmetric data centered at DC), and

(4) The pupil-autocorrelation (the circularly symmetric data centered at DC).

Given (1)-(4), a pupil-filter function was used to filter the desired signal field term. The filtered data was then centered in the Fourier plane before undergoing a discrete Fourier transform to obtain the associated complex-valued image plane in Fig. 4.4(c), concluding frame demodulation.

Each collected frame underwent frame demodulation individually. Otherwise, the piston-phase mismatch introduced on a frame-to-frame basis by the two-independent pulse trains may have washed out the spatial modulation pattern of the digitized hologram, artificially reducing measured SNR. Once the individual frames were demodulated, the energy, or square-magnitude, of each demodulated frame was calculated in pe^2 in accordance with the power definition of SNR [see Eq. (4.1)]. The mean of all 100 demodulated energy frames was computed for each pulse delay increment, τ, to produce an average demodulated energy frame. Frame demodulation and the average demodulated energy frame calculation was repeated for the collected reference-only, signal-only, and background frames using the same pupil-filter function as was used for the digital-hologram frames. This ensured the noise collected with the digital-hologram frames was appropriately accounted for during calculations.

Using the calculated average demodulated energy frames, the measured total-system efficiency, η'_{tot}, was computed using the following equations:

$$E'_N(x,y) = E'_{D-R}(x,y) + E'_{D-S}(x,y) - E'_{D-B}(x,y), \tag{4.5}$$

$$E'_H(x,y,\tau) = E'_{D-H}(x,y,\tau) - E'_N(x,y), \tag{4.6}$$

and

$$\eta'_{tot}(\tau) = \left\langle \frac{SNR'(x,y,\tau)}{SNR(x,y)} \right\rangle = \frac{\pi}{4q_I^2} \left\langle \frac{E'_H(x,y,\tau)/E'_N(x,y)}{\bar{m}'_S(x,y) - \bar{m}'_B(x,y)} \right\rangle, \tag{4.7}$$

where E'_N is the measured noise energy; E'_{D-R}, E'_{D-S}, and E'_{D-B} are the measured reference, signal, and background average energies after frame demodulation, respectively; E'_H is the measured hologram energy; E'_{D-H} is the measured hologram average energy after frame demodulation, SNR' is the measured SNR; and $\bar{m}'_S$ and $\bar{m}'_B$ are the measured mean number of signal and background photoelectrons generated, respectively. Note that the substantial dark-current noise from the camera is accounted for with $\bar{m}'_B$ and E'_{D-B} and is removed, where applicable, by background subtraction. It should also be noted the $\pi/4q_I^2$ term in Eq. (4.7) is necessary to account for the ratio of the pupil-filter function area to the total Fourier plane area [9, 22].

The measured ambiguity efficiency, η'_{amb}, follows as the amplitude normalization of the measured total-system efficiency. In particular,

$$\eta'_{amb}(\tau) = \frac{\eta'_{tot}(\tau)}{\eta'_{tot}(0)}. \tag{4.8}$$

This relationship ensures that η'_{amb} equals unity when the reference and signal fields are perfectly overlapped (i.e., τ = 0 ns) and is always less than one otherwise.

4.4 Results and discussion

Using Eqs. (4.5)-(4.8), the measured total-system and ambiguity efficiencies for a DH system in a heterodyne-pulse configuration were calculated. To analyze the effects of using pulses with non-identical temporal characteristics, the measured efficiencies were compared to those of a DH system in a homodyne-pulsed configuration [34]. The total-system efficiencies at $\tau = 0$ ns were similar and well within the uncertainty of each measurement. Furthermore, the ambiguity efficiency curves exhibited the same general features. Therefore, it was concluded that a heterodyne-pulsed configuration is, in terms of performance, consistent with a homodyne-pulsed configuration. A potential reason for the discrepancies between the ambiguity efficiency predicted using Eq. (4.4) and the measured ambiguity efficiency for the heterodyne-pulsed configuration was then investigated using a complex-optical field model.

4.4.1 Comparison of total-system efficiency

Equations (4.5)-(4.7) were used to calculate a measured total-system efficiency at $\tau = 0$ ns of $13.5\% \pm 6.4\%$ for the DH system described in Section 4.3 with a heterodyne-pulsed configuration. This was 15% lower than the measured total-system efficiency at $\tau = 0$ ns of 15.9% $\pm$ 10.3% for the DH system used in Ref. [34] with a homodyne-pulsed configuration, but the uncertainty bounds of both measurements were well overlapped. Also, the decrease in total-system efficiency for the heterodyne-pulsed configuration was most likely caused by the temporally shorter reference pulse. An 8.8 ns pulse was used for the reference pulse in the heterodyne experiment, whereas a 10 ns pulse was used in the homodyne experiment. This meant the interaction time between the fields was shorter and the amplitudes at which that interaction occurred were reduced for the heterodyne experiment. Therefore, the decrease in system

performance for the heterodyne-pulsed configuration can be attributed to the design of this specific experiment, not the use of a heterodyne-pulsed configuration in general.

With the measured total-system efficiency of both systems calculated for $\tau = 0$ ns, it was sufficient to make all further comparisons between the configurations using their respective ambiguity efficiencies. This ensured any additional differences in system performance would not be attributed to the shortened reference pulses used in the heterodyne experiment. The measured ambiguity efficiencies for the heterodyne- and homodyne-pulsed configurations, as well as the ambiguity efficiency predicted for the heterodyne experiment using Eq. (4.4), are shown in Fig. 4.5.

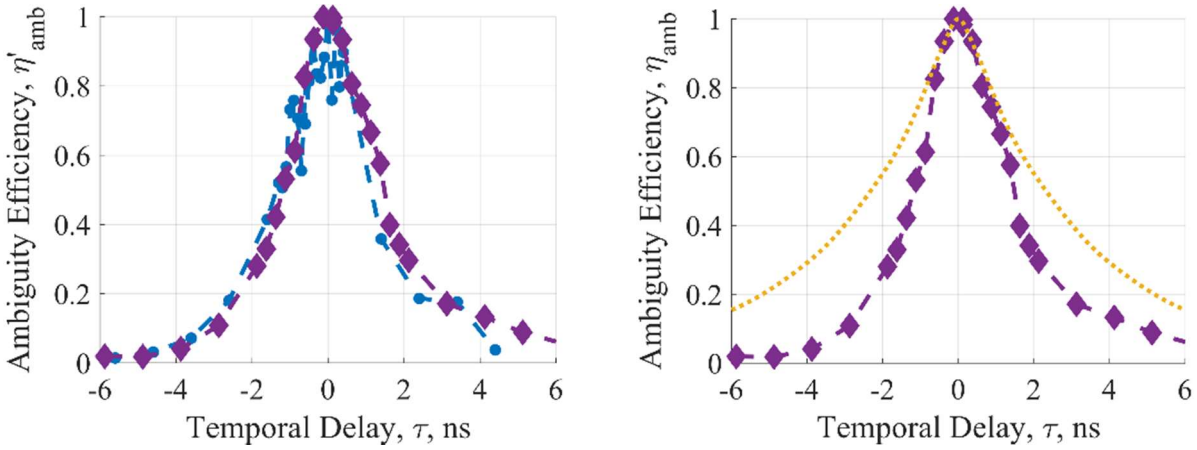

Figure 4.5. Comparison between the measured ambiguity efficiency for the heterodyne-pulsed configuration (- ♦) and (a) the measured ambiguity efficiency for the homodyne-pulsed configuration (– •) from Ref. [18] and (b) the predicted ambiguity efficiency for the heterodyne system (···).

In Fig. 4.5(a), the ambiguity efficiencies for the two configurations are well overlapped. Both follow the same general shape, including the width of each curve and the asymmetry about $\tau = 0$ ns. The ambiguity efficiency for the homodyne-pulsed configuration for $|\tau| \leq 2$ ns was more erratic than that of the heterodyne-pulsed configuration because of the measurement technique used in Ref. [34]. Specifically, the reference and signal quantities used in Eqs. (4.5)-(4.7) were

calculated at each increment of τ. The pulse-to-pulse energy fluctuations in the laser source led to a higher degree of variation between adjacent-τ measurements. Such variation was avoided in the heterodyne-pulsed configuration by only measuring the reference and signal quantities required in Eqs. (4.5)-(4.7) at $\tau = 0$ ns. This outcome was possible because the reference and signal pulses were stable in energy (see Section 4.3). These similarly shaped ambiguity efficiency curves, along with the consistent total-system efficiencies at $\tau = 0$ ns, indicated there was no significant difference in performance when using either a heterodyne- or homodyne-pulsed configuration. Additionally, there were no efficiencies introduced by a heterodyne-pulsed configuration that had not already been accounted for in previous research. Therefore, in terms of system performance, homodyne- and heterodyne-pulsed configurations are consistent.

The ambiguity efficiency predicted using Eq. (4.4), however, did not match the measured ambiguity efficiency calculated using Eq. (4.8), as seen in Fig. 4.5(b). The fields used as inputs to the spectral formulation shown in Eq. (4.4) (i.e., the right-most term) were estimated from the line shapes shown in Fig. 4.3. First, a two-term Lorentzian profile was fit to each spectral line shape. The root-mean-squared error (RMSE) for the reference line shape was 4.7%, and the RMSE for the signal line shape was 3.5%. Then, with the knowledge that the fundamental and secondary modes were spaced approximately 1.5 GHz apart (see Section 4.3), the frequency center of the secondary mode in both fitted Lorentzian profiles was shifted +1.5 GHz. These fitted, shifted Lorentzian profiles were then used as the field inputs to Eq. (4.4). An assumption that no interaction took place between fundamental and secondary modes was then made [42]. The resulting function was taken as the predicted ambiguity efficiency. A detailed explanation of this process can be found in Appendix B of Ref. [34].

In Fig. 4.5(b), the ambiguity efficiency was predicted accurately for $|\tau| \leq 1$ ns but was over-predicted for values $|\tau| \geq 1$ ns. The most probable cause of this over prediction was inaccuracy of the input field estimates [48]. The aliasing and 7.5 MHz resolution of the Fabry-Perot interferometer could have smoothed or hid important features of the spectral line shapes, and certain operational characteristics would be unidentifiable from others. Either of these issues could have led to the inaccurately predicted ambiguity efficiency.

In line with these issues, a potential solution for the inaccurate ambiguity efficiency was postulated: instead of simultaneous propagation of multiple modes, the two-independent pulse trains each experienced an instantaneous phase modulation. It should be noted the effect of this potential solution on the predicted ambiguity efficiency is not unique. In other words, even if including a phase modulation in the input field estimates sufficiently narrows the ambiguity efficiency prediction, other potential solutions cannot be eliminated. Additionally, it is not a guarantee that a phase modulation is present in the fields. The following analysis was performed to validate Eq. (4.4) as a model for the ambiguity efficiency, not to identify any non-ideal characteristics of the laser used in this experiment. By showing it is possible to predict the observed ambiguity efficiency curve width and asymmetry, the ambiguity efficiency model was validated.

4.4.2 Validating the ambiguity efficiency model

In order to investigate the effect on the ambiguity efficiency of including an instantaneous phase modulation in the input fields, a model for the complex-optical fields was created. For this model, it was assumed that the base reference and signal fields could be represented spectrally by pure, Fourier-transform-limited Lorentzian line shapes [56] for the temporal pulse parameters given in Section 4.3. This choice resulted in full width half maximums (FWHMs) of 50 MHz for the reference line shape and 44 MHz for the signal line shape. Each field was also assumed to have

two modes spaced approximately 1.5 GHz apart, identical in all ways except amplitude. The amplitudes of each mode were set to best match the measured data shown in Fig. 4.3. For convenience, the fields described in this paragraph will be referred to as the ideal spectral fields for the remainder of this paper.

Once these ideal spectral fields were defined, they were converted to the temporal domain using a Fourier transform [57]. This was done to ease modeling and computation requirements. The temporal formulation for an instantaneous phase modulation was then multiplied to these ideal temporal fields independently so the effects on the ambiguity efficiency could be analyzed. As a reminder, an instantaneous phase modulation can be caused by multiple issues, all of which result in the same ambiguity efficiency. Therefore, a mode hop was chosen for modeling simplicity. As such, the temporal fields were defined as

$$U_{R,S}(t) = \hat{U}_1^{R,S}(t)\,\xi_1(t) + \hat{U}_2^{R,S}(t)\,\xi_2(t), \tag{4.9}$$

and

$$\xi_1(t) = \left|1 - \xi_2(t)\right| = \begin{cases} 1, & t < t_0 \\ 0, & t \geq t_0 \end{cases}, \tag{4.10}$$

where the subscripts and superscripts R and S indicate the reference and signal fields, respectively, the subscripts 1 and 2 indicate the fundamental and secondary modes, respectively, ξ is the function for a mode hop, and t_0 is the time at which the mode hop occurs. Note the lack of spatial dependence in Eqs. (4.9)-(4.10). Preliminary analysis indicated including spatial dimensions would minimally affect the results. As such, the spatial dependence was removed to improve computation time. However, other potential solutions, especially ones investigating the effect of transverse decoherence, would require spatial dependence to be included in Eq. (4.9).

Before presenting the results concerning the validity of the ambiguity efficiency model presented in Eq. (4.4), a comment about the analysis is required. No effort to model the system hardware was made. Specifically, the measurement of a spectral line shape of a pulsed laser source using a Fabry-Perot interferometer was ignored [54, 55]. Therefore, the model-based spectral line shapes reported below were not expected to match the measured line shapes well and were not a requirement for model validation.

For the instantaneous phase modulation analysis, it was assumed the phase modulation, as modeled by a mode hop, occurred in the amplification stages. To clarify, the intensity modulation scheme (i.e., pulse carving) would require the CW seed to experience a phase modulation every 10 ns on average if the phase modulation occurred in the CW seed. This outcome would be indicative of a level of instability not seen in the laser-beam performance. Therefore, the phase modulation must have taken place in the amplification stages. As a result, the relative mode amplitude and spacing were allowed to change independently in each line shape so that the field-model line shapes matched the measured line shapes as best as possible. With this and the other field-model parameters in mind, the predicted ambiguity efficiency was calculated by substituting Eqs. (4.9) and (4.10) into Eq. (4.4). The aliased spectral line shapes and predicted ambiguity efficiency are shown in Fig. 4.6.

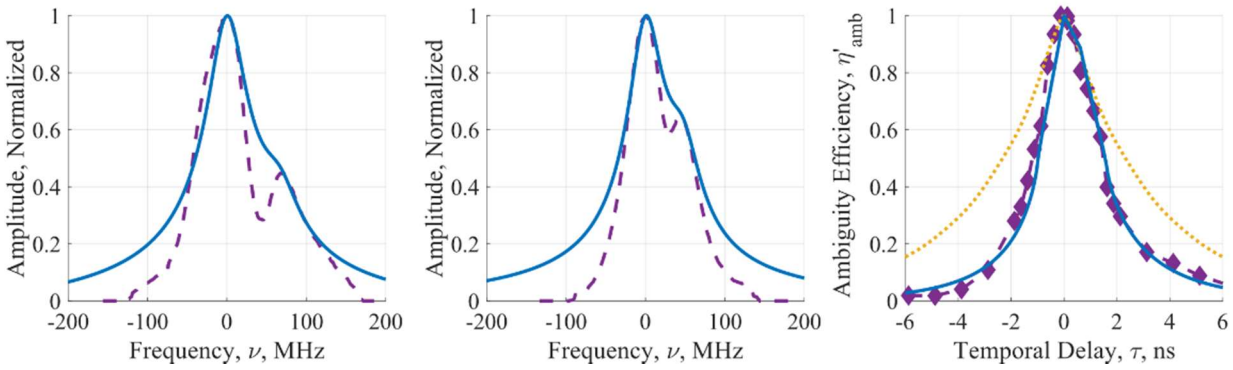

(a) (b) (c)

Figure 4.6. Aliased spectral line shapes of (a) the reference field and (b) the signal field, and (c) the predicted ambiguity efficiency when including a phase modulation in the complex-optical field model. For all plots, the model results (–) are compared to the measured data (- - and - ♦). Additionally, the original ambiguity efficiency prediction (⋯) from Fig. 4.5(b) is included in (c).

As seen in Figs. 4.6(a) and 4.6(b), the spectral line shapes for the reference and signal fields when an instantaneous phase modulation is included in the field model do not match the measured spectra well. The widths of the fundamental peaks are roughly accurate. On the other hand, for both modeled-field line shapes, the existence of a second mode is ambiguous and too much importance is given to the wings. However, these errors cannot be meaningfully improved if a single phase modulation is the only imperfection considered, as was the case here. As a reminder, the line shapes calculated using the complex-optical field model were not linked to validation requirements for the ambiguity efficiency model.

The predicted ambiguity efficiency when including a phase modulation in the complex-optical field model was significantly narrowed, as shown in Fig. 4.6(c). The field model prediction was more accurate than the original prediction at all measured data points where $|\tau| \geq 1$ ns. Asymmetry was also introduced in the ambiguity efficiency prediction, nearly matching the asymmetry in the measured data. Because the inclusion of an instantaneous phase modulation produced a predicted ambiguity efficiency similar to the measured results, further validation of the model presented in Eq. (4.4) was indicated.

4.4.3 Discussion

Using DH systems for applications like long-range imaging requires pulsed laser sources due to the limited longitudinal coherence of CW laser sources. Furthermore, it is highly likely the two pulses used to create the holograms will need to be independent from one another, as the path-length difference between the reference and signal pulses can be in the 10s to 100s of kilometers. In the best-case scenario, where the reference and signal pulses are both Fourier-transform limited, the independence of the pulses will not affect DH system performance in terms of the ambiguity efficiency. This outcome is because the only phase characteristic changing pulse to pulse in each pulse train is the piston phase. In practice, the piston phase only affects the location of the hologram nulls. By collecting only one interference event per hologram (i.e., per camera frame) and demodulating the holograms individually, the effect of hologram-null location change is negated.

When the pulses are degraded such that they are no longer Fourier-transform limited, the power spectrum of the pulses is broadened and hologram quality decreases. Because of this, it was uncertain what effect the independence of the pulses would have on the ambiguity efficiency. In other words, it was unknown if the non-identical perturbations within the independent pulse trains of the heterodyne-pulsed configuration would cause the ambiguity efficiency to narrow or otherwise change with respect to the ambiguity efficiency measured using a homodyne-pulsed configuration. As shown in the results above, neither narrowing nor other changes were observed. It was shown that the ambiguity efficiencies for DH systems in homodyne- and heterodyne-pulsed configurations are consistent.

At first glance, the non-identical power spectra of the reference and signal pulses may seem to contradict this observation. However, examination of the ambiguity efficiency, as given by Eq. (4), shows the quantity of importance is the cross-spectral density of the pulses, specifically the

widths of any spectral features, not the power distributions of the individual pulses. Therefore, two systems with similar cross-spectral densities are expected to exhibit similar ambiguity efficiencies regardless of configuration. This scenario was presented in this paper. The spectral feature widths of the cross-spectral densities of the homodyne-pulsed configuration in Ref [18] and the heterodyne-pulsed configuration described above were similar, and the measured ambiguity efficiencies of both configurations were also similar.

Another issue introduced when using degraded pulses, whether in the homodyne- or heterodyne-pulsed configuration, is difficulty in predicting the ambiguity efficiency. By design, one-dimensional laser diagnostic devices, such as the Fabry-Perot interferometer used in this experiment, are unable to capture degraded transverse beam quality. This outcome is in direct conflict with the two-dimensional DH measurements. Therefore, it is unsurprising that an ambiguity efficiency prediction made using a one-dimensional Fabry-Perot interferometer and non-Fourier transform limited pulses does not match the measured ambiguity efficiency. A complex-optical field model was created and modified to produce a sufficiently narrow ambiguity efficiency prediction, but also produced spectral line shapes outside measurement uncertainty. The narrowing of the ambiguity efficiency prediction indicated the ambiguity efficiency model presented in Eq. (4.4) was valid, but the full potential of that model is unrealizable with the tools used for this experiment.

A solution to this issue would involve recording the spectral line shape across the beam profile with a high-speed, two-dimensional interferometer. Such a device could capture the degraded transverse beam quality of non-spatially uniform pulses. The ambiguity efficiency could then be two-dimensionally predicted, better matching the two-dimensional DH measurement. However, a high-speed, two-dimensional interferometer would still require temporal averaging

across multiple pulses to produce a spectral line shape. Instrument line shape and SNR compound this problem. Therefore, an accurate estimate for the reference and signal fields will continue to be difficult to acquire with current technology.

Another step that could improve prediction accuracy is further developing the complex-optical field model. The current field model did not take into account instrument-specific collection parameters. An updated field model for the experiment presented in this paper would need to account for temporal pulse averaging [55], instrument line shape, and temporal-spatial frequency resolution requirements. By refining the field model, it could better simulate laser diagnostic measurements and improve estimated field inputs to the ambiguity efficiency model. This step, however, is outside the scope of the analysis presented in this paper.

4.5 Conclusion

A digital-holography (DH) system was created in a heterodyne-pulsed configuration. Using the off-axis image plane recording geometry, two performance metrics were measured: (1) the total-system efficiency and (2) the ambiguity efficiency. These metrics were compared against the same measured efficiencies for a DH system in a homodyne-pulsed configuration. The total-system efficiency of both systems was found to be consistent with one another, showing that no new component efficiencies were required when switching from a homodyne- to a heterodyne-pulsed configuration. Additionally, an instantaneous phase modulation model was used to characterize system performance in terms of non-ideal pulse overlap. Such a model validated the use of the ambiguity efficiency for future efforts.

V. Spectral broadening effects on digital-holography systems in a heterodyne-pulsed configuration

The contents of this chapter are in the final stages of the draft process and will be submitted to the IEEE Journal of Quantum Electronics upon completion.

A digital-holography (DH) system in a heterodyne-pulsed configuration is set up in the off-axis image plane recording geometry. Then, spectral broadening of the laser source is introduced to degrade the temporal coherence of the pulses, and the associated effects on the ambiguity and coherence efficiencies are measured. It is found that the ambiguity efficiency is not affected by this source of temporal coherence degradation. The coherence efficiency, however, is found to adequately characterize the performance degradation. As a result, the coherence efficiency is validated for pulsed-source DH systems for the first time in the published literature.

5.1 Introduction

Digital-holography (DH) has been shown as a solution to the low-light and deep-turbulence conditions associated with long-range imaging scenarios [6-9, 22]. Using a strong reference beam, hologram-imaging systems interfere two electric fields to create a spatially modulated pattern, otherwise known as a hologram [10]. With DH, this hologram can be computationally processed to estimate the complex-optical field. This field, in terms of amplitude and wrapped phase, contains information about the spatially-distributed aberrations along the propagation path. Because of these benefits, DH has been studied as a way to improve long-range imaging performance [11-16].

To optimize DH systems, performance in terms of signal-to-noise ratio (SNR) has been characterized for many independent sources of performance degradation [17, 18]. These sources of degradation are commonly called efficiencies. Recent experiments quantified the efficiencies

for both homodyne-pulsed and heterodyne-pulsed configurations using temporally coherence laser sources [34, 47]. With these baselines established, it is beneficial to analyze DH system performance as a function of laser source degradation for pulsed configurations. For either physics-based or equipment-based reasons, the temporal coherence of a high-powered laser source used for DH applications may be less than ideal. Understanding the effects of degraded temporal coherence will help build the trade space when constructing a pulsed-source DH system.

To this end, a DH system in a heterodyne-pulsed configuration was set up to characterize these degraded coherence effects. Pseudo-random bit sequence (PRBS) was introduced to the laser source to degrade the temporal coherence via spectral broadening. The results of this characterization show linewidth broadening has no significant effect on the ambiguity efficiency (i.e., system performance as a function of pulse overlap). However, the total-system efficiency is reduced in accordance with the coherence efficiency. While previously shown for a continuous-wave (CW) configuration [18], this is the first time such results have been presented in the published literature for a pulsed-source DH configuration. This closes the loop, so to speak, between efficiency characterizations of DH systems in CW and pulsed configurations.

In what follows, Section 5.2 describes PRBS and the applicable efficiencies. Section 5.3 details the experiment, including data-collection and data-processing methodologies. The characterization of the effects of spectral broadening of the laser source is presented in Section 5.4. A conclusion is presented in Section 5.5.

5.2 Theory

This Section provides the background theory necessary to interpret and analyze the results presented in Section 5.4. First, the relevant elements of PRBS are introduced to provide insight

into how the laser source is modulated. Then, an overview of the applicable efficiencies, namely the ambiguity and coherence efficiencies, is given.

5.2.1 Effects of PRBS

Spectral broadening in this experiment was achieved by phase-modulating a CW seed laser via PRBS. PRBS involves a binary, randomly fluctuating electrical signal being driven into a phase modulator. In turn, the phase of the complex-optical field passing through the modulator is rapidly changed. Three factors, set by the user, characterize PRBS: (1) the pattern length, (2) the modulation frequency, and (3) the amplitude [58].

PRBS is pseudo-random because the length of the binary, or bit, sequence is finite before it repeats. This length, called the pattern length, is denoted as $2^{n_{PRBS}}-1$, where n_{PRBS} is the shift register length used to create the pattern. The larger the n_{PRBS}, the longer the sequence is before the pattern repeats.

The modulation frequency is the number of possible phase changes per second. In practical terms, the temporal spacing between each bit, or the bit period, is determined by the modulation frequency. Together, the pattern length and modulation frequency drive the mode spacing in the phase-modulated spectrum, $\Delta\nu_{pms}$, of the complex-optical field such that [58]

$$\Delta\nu_{pms} = \frac{\nu_{PRBS}}{2^{n_{PRBS}}-1}, \tag{5.1}$$

where ν_{PRBS} is the modulation frequency. If n_{PRBS} is sufficiently large, the mode spacing will be such that the individual modes are non-resolvable and the spectral line shape of the modulated laser source is broadened.

The amplitude of the PRBS signal, or peak-to-peak voltage, determines the magnitude of the phase change, known as the depth of modulation. This phase change leads to a change in instantaneous frequency, $\Delta\nu_{dm}$, such that [18]

$$\Delta\nu_{dm} = \frac{1}{2\pi}\Delta\phi, \tag{5.2}$$

where $\Delta\phi$ is the depth of modulation. A voltage setting of note is called the half-wave voltage. The half-wave voltage results in a depth of modulation of π, leading to the greatest amount of broadening possible. Going beyond this depth of modulation will cause the line shape to narrow until it returns to the original line shape at a depth of modulation of 2π.

Introducing PRBS to a laser source will cause the source linewidth to broaden with a sinc^2 line shape [59]. The CW seed laser used for this paper has a Lorentzian line shape when not modulated by PRBS, resulting in a modulated line shape, G, of the form

$$G(\nu) = A_L \frac{\Delta\nu_L}{(\nu-\nu_0)^2 + \left(\frac{\Delta\nu_L}{2}\right)^2} + A_S \text{sinc}^2\left(\frac{\nu-\nu_0}{\Delta\nu_S}\right), \tag{5.3}$$

where A_L and A_S are the amplitudes of the Lorentzian and sinc^2 line shapes, respectively, $\Delta\nu_L$ and $\Delta\nu_S$ are the widths of the Lorentzian and sinc^2 line shapes, respectively, ν is the frequency, and ν_0 is the center frequency of the line shapes. Here, $\text{sinc}(x) = 1$ when $x = 1$ and $\text{sinc}(x) = \sin(\pi x)/(\pi x)$ otherwise [43, 44]. In practice, every phase modulator is different. Therefore, it is more accurate to measure the modulated line shapes and apply a fit using Eq. (5.3) than it is to estimate the modulated line shapes using PRBS characteristics. Doing so allows for SNR degradation to be measured as a function of (1) sinc^2 null location, $\Delta\nu_S$, related to PRBS frequency; and (2) the ratio of the energy in the sinc^2 line shape to the energy in the total line

shape, or β, related to depth of modulation. When $\beta = 1$, the laser source is fully modulated and the spectral line shape is completely sinc^2. Otherwise, the laser source is only partially modulated and exhibits both Lorentzian and sinc^2 line shapes.

5.2.2 Efficiencies

This paper utilizes the off-axis image plane recording geometry (IPRG), creating a hologram in the image plane of a pupil by interfering a strong, off-axis, diverging reference pulse with an on-axis, converging signal pulse [22]. The power definition of the SNR for this recording geometry is given by [6, 9, 48]

$$SNR(x, y, \tau) = \eta_{tot}(x, y, \tau) \frac{4 q_I^2}{\pi} \bar{m}_S(x, y), \tag{5.4}$$

where (x, y) are the estimated image-plane coordinates, τ is the temporal delay between the centers of the reference and signal pulses, η_{tot} is the total-system efficiency, q_I is the image-plane sampling quotient, and $\bar{m}_S$ is the mean number of signal photoelectrons generated by the signal pulse. It should be noted Eq. (5.4) assumes the reference is sufficiently strong such that the DH system is operating in a shot-noise-limited regime [6, 20]. Any effects of the system not operating at the shot-noise limit are captured by η_{tot} [17, 34].

The goal of this paper is to analyze system SNR as a function of temporal coherence. Therefore, it is of interest to look closely at the total-system efficiency as it is comprised of independent, multiplicative sources of SNR degradation such that [17, 18, 34]

$$\eta_{tot}(x, y, \tau) = \eta_{ern} \eta_{snl}(x, y) \eta_{pol} \eta_{mod} \eta_{amb}(\tau) \eta_{coh}(\tau), \tag{5.5}$$

where η_{ern} is the excess-reference-noise efficiency, η_{snl} is the shot-noise-limit efficiency, η_{pol} is the polarization efficiency, η_{mod} is the modulation efficiency, η_{amb} is the ambiguity efficiency, and

η_{coh} is the coherence efficiency. The excess-reference-noise, shot-noise-limit, polarization, and modulation efficiencies are not dependent on the coherence of the pulses used to create a hologram [17, 18, 21]. Because of this, these efficiencies are not of concern in this paper.

However, the ambiguity and coherence efficiencies are fundamentally linked to the temporal coherence of the pulses [18, 34, 48]. The ambiguity efficiency is derived from the zero-Doppler cut of the ambiguity function [31, 32, 34], such that

$$\eta_{amb}(\tau) = \left\langle \left| \int_{-\infty}^{\infty} U_R(x,y,t) U_S^*(x,y,t-\tau)\, dt \right|^2 \right\rangle, \tag{5.6}$$

where U_R and U_S are the complex-optical fields of the reference and signal pulses in the temporal domain, respectively, t is time, $*$ denotes the complex conjugate, $|\bullet|^2$ is the square-magnitude operator, and $\langle \bullet \rangle$ is the spatial average operator. The square-magnitude operator is necessary as Eq. (5.4) uses the power definition of SNR. On the other hand, the spatial average operator is not required in Eq. (5.6), but it is convenient to have spatially independent metrics when cross-evaluating multiple DH systems and is thus used here.

The coherence efficiency is related to the effective complex degree of coherence, γ_{eff}, such that [18]

$$\eta_{coh}(\tau) = \left| \gamma_{eff}(\tau) \right|^2. \tag{5.7}$$

If the coherence length of the reference and signal pulses are much longer than the integration time of the imaging system and the pulses are identical, the effective complex degree of coherence is equal to the complex degree of coherence, γ, of the laser source. By the Wiener–Khinchin theorem then, γ_{eff} is the Fourier transform of the laser spectral line shape [42].

In all other circumstances, γ_{eff} requires further calculation [19] and will be dependent on the specific pulse-generation process used. For the experiment set up described in Section 5.3, reference and signal pulses are independently carved from a phase-modulated CW laser source. Therefore, the calculation of the effective complex degree of coherence begins with "carving out" a section of γ of the CW source, such that

$$\gamma_{R,S}(t) = \gamma(t) T_{R,S}(t), \tag{5.8}$$

where γ_R and γ_S are the complex degrees of coherence of the reference and signal pulses, respectively, and T_R and T_S are the temporal profiles of the reference and signal pulses, respectively. Both γ and $T_{R,S}$ equal unity at $t = 0$ and are less otherwise. Note that Eq. (5.8) assumes any amplification subsequent to pulse carving does not affect the complex degree of coherence. Because the pulses may be delayed in relation to one another, the effective complex degree of coherence of the system is found via the correlation of the square roots of the complex degrees of coherence of the pulses, such that

$$\gamma_{eff}(\tau) = \int_{-\infty}^{\infty} \sqrt{\gamma_R(t)} \sqrt{\gamma_S(t-\tau)} dt\,. \tag{5.9}$$

5.3 Experiment

The setup for this experiment is shown in Fig. 5.1. A DH system in a heterodyne-pulsed configuration was set up in the off-axis IPRG with a 1064 nm pulsed laser source and a short-wave infrared (SWIR) camera. The independent reference and signal pulses were generated by a custom-built NP Photonics Coherent High Energy Pulsed Fiber Laser System [45], using two independent pulse trains in a master oscillator power amplifier, or MOPA, configuration. In practice, other

heterodyne-pulsed configurations exist but the conclusions reached in this paper hold for them as well.

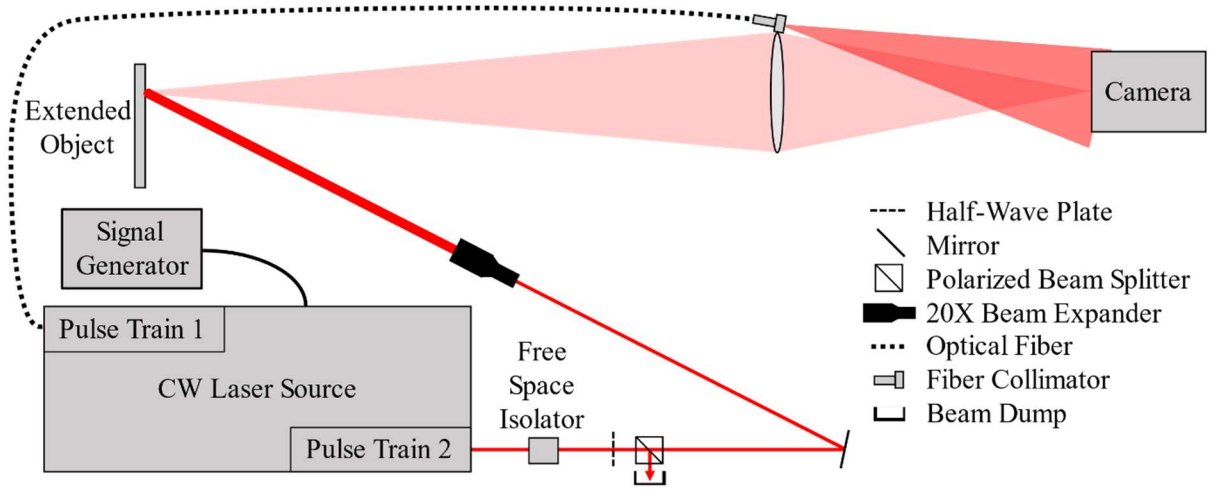

Figure 5.1. Experiment Setup.

The output of a CW seed laser with a 1064 nm center wavelength was passed through a phase modulator controlled by an external signal generator. After the phase modulator, two independent beam paths were created by amplitude-splitting the phase-modulated CW laser. Then, the two prongs of the split CW beam were independently intensity modulated. Following intensity modulation, the pulses were amplified via independent ytterbium-doped fiber amplifier stages. Both pulse trains operated at a 1 kHz repetition rate.

Pulse train 1 generated 8.8 ns reference pulses with an average energy of 10 nJ, which exited the backend tip of a 2 m long polarization-maintaining, single-mode optical fiber. The tip was coupled to an adjustable collimator to maintain a nearly uniform energy distribution over the camera FPA while ensuring enough reference energy was captured to perform DH. This collimator was placed off-axis next to the imaging lens and tilted toward the camera.

Pulse train 2 produced 10 ns signal pulses with an average energy of 10 μJ . These pulses were passed through a free-space isolator, half-wave plate, and polarized beam splitter (PBS) to control the energy of the signal pulses. The pulses were then sent through a 20x beam expander,

scattered off a sheet of Labsphere spectralon (i.e., a stationary, optically rough, extended object) with a vendor-specified 99% Lambertian reflectivity. This reflected light was imaged onto the camera via a 2.54 cm imaging lens. As a note, the object and image distances of the imaging system were set such that the measured image-plane sampling quotient, q_I, was 3.35 [9, 22]. By definition, q_I represents the number of circular-pupil diameters that can fit across the Fourier plane.

The average energy of the pulses from both pulse trains fluctuated $\pm$ 16% pulse to pulse over a 6-hour time period, much longer than required to collect any single dataset. Therefore, the energy in each pulse train was considered stable. A Berkeley Nucleonics Corporation Model 577 Digital Delay/Pulse Generator was used to control the temporal delay, τ, between the reference and signal pulses at the camera FPA during the intensity modulation process. This pulse generator provided a minimum sampling resolution of 250 ps and a root-mean-squared jitter of 100 ps.

The phase modulator internal to the laser system was controlled by an external Picosecond Pulse Labs Model 12020 Pulse/Pattern Generator. This pattern generator was able to generate PRBS with limits of $5 \le n_{PRBS} \le 31$, modulation frequencies of $15\ \text{MHz} \le \nu_{PRBS} \le 1\ \text{GHz}$, and peak-to-peak voltages of $55\ \text{mV} \le V_{p-p} \le 2.5\ \text{V}$. The phase modulator native to the laser system restricted the maximum V_{p-p} to 300 mV. Additionally, due to laser system constraints, these peak-to-peak voltages could not be converted into their associated depths of phase modulation. Therefore, β was measured from the phase-modulated CW spectral line shapes and used as a proxy for the depth of modulation.

For the camera, an Allied Vision Goldeye G-033 SWIR TEC1, with a pixel-well depth of 25,000 photoelectrons (pe) and a quantum efficiency of 77% at 1064 nm, was used. This camera had an unstable gain region for integrations times less than $25\ \mu s$. As a result, over a quarter of

the pixel-well depth was filled by dark-current noise, making dark-current noise the dominant factor in the camera-noise variance, σ_n^2. Overall, $\sigma_n^2 = 6,486$ pe^2. Due to the unstable gain region, both pulses were set to arrive at the camera FPA near the $27\ \mu s$ integration-time mark with a total frame-integration time of $30\ \mu s$.

To avoid camera-pixel saturation while still maximizing sensing, the mean number of photoelectrons generated by the reference and signal at the camera, $\bar{m}_R$ and $\bar{m}_S$ respectively, were set such that $\bar{m}_R = 11{,}121$ pe and $\bar{m}_S = 85$ pe. Assuming Poisson statistics, where the mean equals the variance, these set values meant the reference noise did not dominate all other noise sources, as $\sigma_n^2 > 1/2\,\bar{m}_R$. Therefore, the DH system used in this experiment was not operating in the shot-noise-limited regime [20, 22]. However, this did not affect the ambiguity and coherence efficiencies and is accounted for by other component efficiencies within the total-system efficiency [18, 34].

5.3.1 Data-collection methodology

This experiment was performed in two separate parts. The first part of the experiment focused on the ambiguity efficiency. Three datasets were collected, each corresponding to a different set of PRBS parameters. The first dataset was a baseline, therefore the PRBS generator was disabled. Then, two datasets were taken with the following parameters: (1) $\nu_{PRBS} = 15$ MHz, $V_{p-p} = 200$ mV; and (2) $\nu_{PRBS} = 1$ GHz, $V_{p-p} = 75$ mV. For these two datasets, the shift register length was set to the maximum possible value, $n_{PRBS} = 31$. This guaranteed the minimal mode spacing for all PRBS frequencies [see Eq. (5.1)].

For each dataset, digital holograms were collected for temporal delay values from τ = -6 ns to +6 ns in 1 ns increments and from τ = -2 ns to +2 ns in 0.25 ns increments to sufficiently

sample both the wings and the peak of the ambiguity efficiency curve. Two measurements were taken at $\tau = 0$ ns, one at the beginning of the overall data collection period and one at the halfway mark, to ensure the master oscillator and amplification paths were performing consistently for the entire dataset. For each increment of τ, the Labsphere Spectralon sheet was rotated to generate 10 distinct speckle realizations. For each speckle realization, 10 digital-hologram frames were collected for a total of 100 digital-hologram frames for each temporal pulse delay value. This was done for averaging during data processing. Additionally, 10 reference-only frames and 10 signal-only frames were collected for each speckle realization during both $\tau = 0$ ns measurements. Reference-only and signal-only frames were unnecessary for all temporal delay values because the energy of both pulse trains was stable for each individual dataset. After all other frames in the dataset were collected, 100 background frames were collected so the background and camera noise could be appropriately accounted for during efficiency calculations.

After processing and analyzing the data from the first part of the experiment (as described in Section 5.3.2), the data-collection methodology changed. Results from the first experiment showed the ambiguity efficiency was not significantly affected by the PRBS signal. However, the total-system efficiency was affected uniformly by a constant multiplier. Therefore, the coherence efficiency at a single value of τ was sufficient to characterize the coherence efficiency for all pulse delay values. As such, digital holograms were only taken at $\tau = 0$ ns for various modulation frequency and peak-to-peak voltage pairings. Those pairings can be roughly grouped as follows:

(1) A baseline for which the PRBS generator was disabled,

(2) Stepping from $V_{p-p} = 100$ mV to $V_{p-p} = 300$ mV in 50 mV increments, with an additional collection at $V_{p-p} = 55$ mV, while holding $v_{PRBS} = 100$ MHz, and

(3) Stepping from $v_{PRBS} = 15$ MHz to $v_{PRBS} = 90$ MHz in 15 MHz increments, from $v_{PRBS} = 100$ MHz to $v_{PRBS} = 145$ MHz in 15 MHz increments, and from $v_{PRBS} = 200$ MHz to $v_{PRBS} = 300$ MHz in 50 MHz increments while holding $V_{p-p} = 200$ mV.

The second grouping was collected to characterize the coherence efficiency in terms of depth of modulation. The third grouping was collected to characterize the coherence efficiency in terms of modulation frequency. As with the first part of the experiment, the shift register length was set such that $n_{PRBS} = 31$ for all pairings.

For each modulation frequency and peak-to-peak voltage pairing, the digital-hologram collection process followed that of the first part of this experiment (i.e., 10 speckle realizations, with 10 digital-hologram frames per speckle realization). Additionally, 10 reference-only frames and 10 signal-only frames were collected for each speckle realization for the baseline. As a reminder, the energy of both pulse trains was considered stable so reference-only and signal-only frames were not necessary for each pairing. After data for all pairings were collected, 100 background frames were collected so the background and camera noise could be accounted for during calculations. All frames from both parts of the experiment were imported to MATLAB for processing.

5.3.2 Data-processing methodology

To calculate the ambiguity and coherence efficiencies, the collected frames were demodulated. An example using a digital-hologram frame is shown in Fig. 5.2.

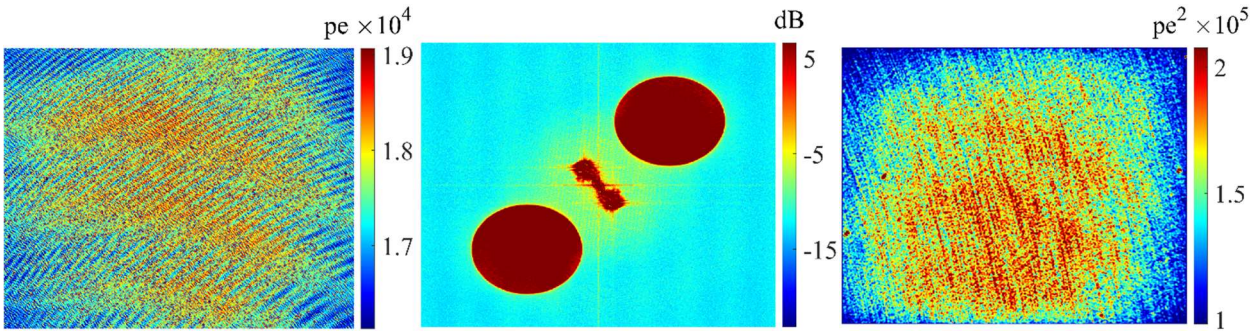

Figure 5.2. Frame-demodulation for a digital-hologram frame. Demodulation involves (a) the real-valued recorded frame, (b) the associated complex-valued Fourier plane, and (c) the associated image frame.

To begin demodulation, a discrete inverse Fourier transform was performed on the real-valued digital-hologram frame in Fig. 5.2(a) to obtain the complex-valued Fourier plane in Fig. 5.2(b). In accordance with the off-axis IPRG [22], the Fourier plane contained four key terms:

(1) The signal field (the data in the top-right circular pupil),

(2) The complex-conjugate of the signal field (the data in the bottom-left circular pupil),

(3) The LO-autocorrelation (the non-circularly symmetric data centered at DC), and

(4) The pupil-autocorrelation (the circularly symmetric data centered at DC).

With (1)-(4) in mind, a pupil-filter function was used to filter the signal field term. The filtered signal term was then centered in the Fourier plane before a discrete Fourier transform was applied to obtain the complex-valued image plane. Finally, the energy, or square-magnitude, of the complex-valued image frame was calculated in pe^2 in accordance with the power definition of SNR [see Eq. (5.4)] to generate Fig. 5.2(c). This concluded frame demodulation.

All collected hologram frames underwent frame demodulation individually. Frame averaging before frame demodulation would reduce SNR as the piston phase mismatch introduced frame-to-frame by the independent pulse trains may have degraded the digitized hologram. The 100 demodulated energy frames associated with a specific pulse delay, τ, were averaged together to produce a mean demodulated energy frame at that τ. This process was repeated for all pulse

delay values. Frame demodulation and the mean demodulated energy frame calculation were repeated for the collected reference-only, signal-only, and background frames using the same pupil-filter used for the digital-hologram frames. This ensured the noise was accounted for appropriately during efficiency calculations.

Using the mean demodulated energy frames, the measured ambiguity efficiency, η'_{amb}, was computed using the following equations:

$$E'_N(x,y) = E'_{D-R}(x,y) + E'_{D-S}(x,y) - E'_{D-B}(x,y), \tag{5.10}$$

$$E'_H(x,y,\tau) = E'_{D-H}(x,y,\tau) - E'_N(x,y), \tag{5.11}$$

$$\eta'_{tot}(\tau) = \left\langle \frac{SNR'(x,y,\tau)}{SNR(x,y)} \right\rangle = \frac{\pi}{4q_I^2} \left\langle \frac{E'_H(x,y,\tau)/E'_N(x,y)}{\bar{m}'_S(x,y) - \bar{m}'_B(x,y)} \right\rangle, \tag{5.12}$$

and

$$\eta'_{amb}(\tau) = \frac{\eta'_{tot}(\tau)}{\eta'_{tot}(0)}, \tag{5.13}$$

where E'_N is the measured noise energy; E'_{D-R}, E'_{D-S}, and E'_{D-B} are the measured reference, signal, and background average energies after frame demodulation, respectively; E'_H is the measured hologram energy; E'_{D-H} is the measured hologram average energy after frame demodulation, SNR' is the measured SNR; and $\bar{m}'_S$ and $\bar{m}'_B$ are the measured mean number of signal and background photoelectrons generated, respectively. Note that the substantial dark-current noise from the camera is accounted for with $\bar{m}'_B$ and E'_{D-B} and is removed, where applicable, by background subtraction. It should also be noted the $\pi/4q_I^2$ term in Eq. (5.12) is necessary to account for the ratio of the pupil-filter function area to the total Fourier plane area [9, 22].

The measured coherence efficiency, η'_{coh}, was calculated in a similar fashion, such that

$$\eta'_{coh}\left(\beta,\Delta\nu_S\right)=\frac{\eta'_{tot}\left(\beta,\Delta\nu_S\right)}{\eta'_{tot}\left(0,0\right)}, \tag{5.14}$$

where β and $\Delta\nu_S$ were estimated from the phase-modulated CW laser source spectral line shapes [see Eq. (5.3)]. The phase-modulated pulsed source spectral line shapes were not used as accurately capturing such spectra was not possible with the available equipment [47]. Therefore, some error between the theoretical coherence efficiency calculated using Eqs. (5.7) and (5.9) and the measured coherence efficiency was expected. Also, because all coherence efficiency measurements were taken at $\tau = 0$ ns, the dependence on τ was dropped for Eq. (5.14).

5.4 Results and discussion

The effects of spectral broadening of the laser source on the ambiguity efficiency was analyzed by systematically degrading the temporal coherence of the laser source, then measuring the resulting ambiguity efficiencies using Eqs. (5.10)-(5.13). Comparison of these measured ambiguity efficiencies showed spectrally broadening the laser source did not significantly affect the ambiguity efficiency of a DH system in a heterodyne-pulsed configuration. However, preliminary analysis showed degraded temporal coherence did reduce total-system efficiency in a nearly uniform manner. Therefore, deeper investigation into the effect of degraded temporal coherence on DH system efficiencies was performed. This analysis showed the coherence efficiency was appropriate to characterize these effects.

5.4.1 Ambiguity efficiency analysis

The phase-modulated CW line shapes associated with the three datasets collected during the first part of this experiment (see Section 5.3.1) are shown in Fig. 5.3. These line shapes, as well as all line shapes used in this paper, were measured using a using a Thorlabs SA200-8B scanning

Fabry-Perot interferometer with a 7.5 MHz resolution. Alongside these line shapes are the ambiguity efficiencies calculated using Eq. (5.13) for the same three datasets.

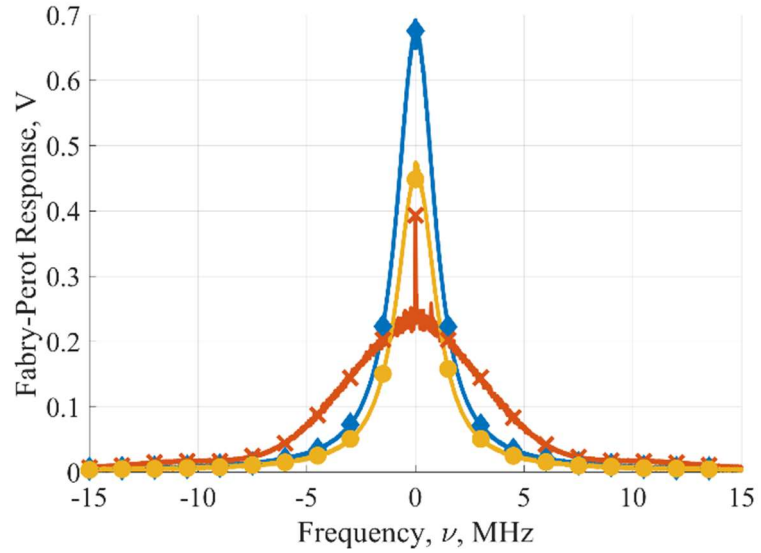

(a)

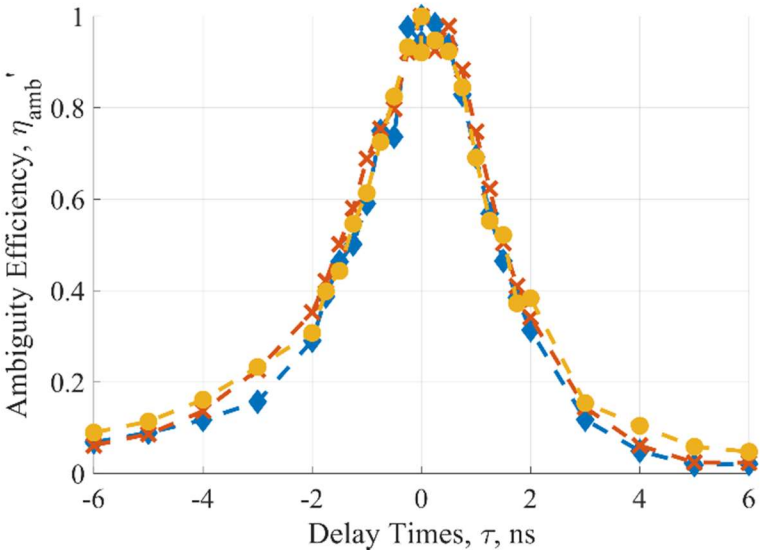

(b)

Figure 5.3. Comparing the (a) phase-modulated CW line shapes and (b) and ambiguity efficiencies for the following ν_{PRBS} and V_{p-p} pairings: $\nu_{PRBS} = 0$ MHz, $V_{p-p} = 0$ mV (– ♦); $\nu_{PRBS} = 15$ MHz, $V_{p-p} = 200$ mV (– ×); and $\nu_{PRBS} = 1$ GHz, $V_{p-p} = 75$ mV (– •).

As seen in Fig. 5.3(b), the ambiguity efficiencies follow the same general shape regardless of modulation frequency or peak-to-peak voltage. At first glance, this result is seemingly in

contradiction with the phase-modulated CW line shapes shown in Fig. 5.3(a). In Fig. 5.3(a), the amount of energy in the peak is distributed to the wings as a function of amount of temporal degradation. In other words, more broadening occurs for greater values of ν_{PRBS} and V_{p-p}. This is most readily visible for the $\nu_{PRBS} = 15$ MHz, $V_{p-p} = 200$ mV case, where the peak power is roughly 36% of the baseline ($\nu_{PRBS} = 0$ MHz, $V_{p-p} = 0$ mV) but has significantly more energy in the wings. The degradation of the laser source seen in Fig. 5.3(a) may bring about the expectation of system performance falling off faster as the temporal delay between the pulses increases (i.e., a narrower ambiguity efficiency).

However, this expectation must be tempered by the heterodyne nature of the DH configuration. By definition, the reference and signal pulses of a heterodyne configuration have non-identical temporal phase characteristics. This difference in temporal phase determines the location of the hologram nulls [47]. As phase modulation is introduced into each pulse independently, the difference in temporal phase between the pulses changes as function of time. Therefore, the hologram null locations are also changing as a function of time, partially washing out the recorded hologram fringes for all values of τ. Because this is a uniform effect for all τ, the ambiguity efficiency should not be affected and the results shown in Fig. 5.3(b) are not in contradiction with the phase-modulated line shapes.

Another way to reach the same conclusion is to look at PRBS noise characteristics. Because $n_{PRBS} > 20$, the noise characteristics associated with the PRBS signals used in this experiment were approximately Gaussian [60]. The mean of a Gaussian noise distribution is zero. Therefore, by using the mean hologram frame for the ambiguity efficiency calculations, the spectral variance of the individual hologram frames was averaged out. This, paired with the non-deterministically correlated phase content of the reference and signal pulses (a key feature of heterodyne

configurations), means no change in the ambiguity efficiency should be expected. This is validated by Fig. 5.3(b). With Fig. 5.3(b) and these explanations in mind, it was concluded that temporally degrading the laser source via PRBS did not significantly affect the ambiguity efficiency of a DH system in a heterodyne-pulsed configuration.

5.4.2 Coherence Efficiency Analysis

While the ambiguity efficiency was not significantly changed as a function of temporal coherence of the laser source, preliminary results showed the total-system efficiency was. Therefore, the coherence efficiency was introduced to account for these effects. The coherence efficiency was predicted using Eqs. (5.7)-(5.9) with an estimated complex degree of coherence, γ, calculated from fitting the phase-modulated CW line shape with Eq. (5.3). An example of this fit is shown in Fig. 5.4.

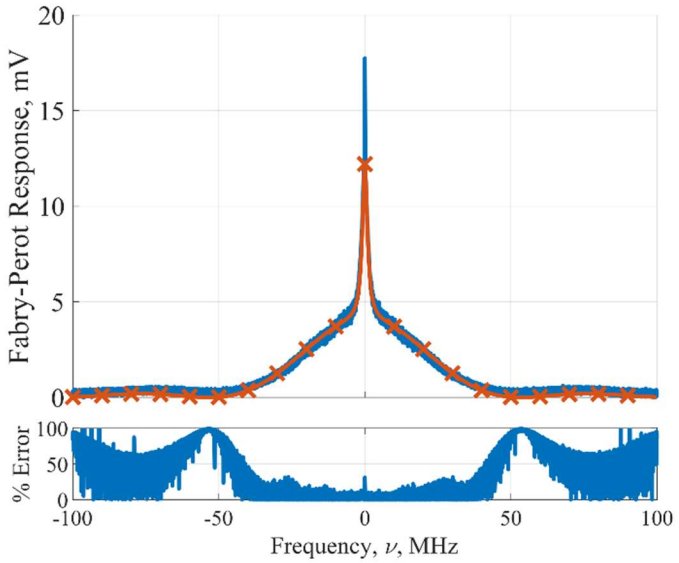

Figure 5.4. Phase-modulated CW line shape (–) with a fitted line shape (−×). The absolute percent error of the fit is plotted underneath.

To create the fitted line shape in Fig. 5.4, the Lorentzian fit was given infinite weight near the center of the line shape and the sinc^2 fit was given infinite weight in the wings. This was done to ensure the unmodulated and modulated sections, respectively, of the line shape were fit as

accurately as possible. Despite this, a narrow peak on the order of kHz in width and centered on the origin was not fitted well by the Lorentzian. This narrow, poorly fitted peak appeared in all fitted line shapes except the unmodulated baseline, indicating there was a systematic, structured element unaccounted for in the phase-modulated line shapes. However, the percent error over this poorly-fitted peak was significantly less than the error at the sinc^2 null locations and further out in the wings. Additionally, a more complicated line shape was fitted to the measured phase-modulated CW data to account for this narrow peak, but the effect on the coherence efficiency characterization was negligible. Also, the kHz linewidth was orders of magnitude narrower than the resolution of the Fabry-Perot interferometer used to measure the spectra. With all three of these factors in mind, this peak was ignored and the summation of a Lorentzian and sinc^2 line shape was used as the fit equation.

From the fitted equations, values for β and $\Delta\nu_S$ were calculated for use during coherence efficiency characterization. The coherence efficiency, as calculated using Eq. (5.14), is shown in Fig. 5.5.

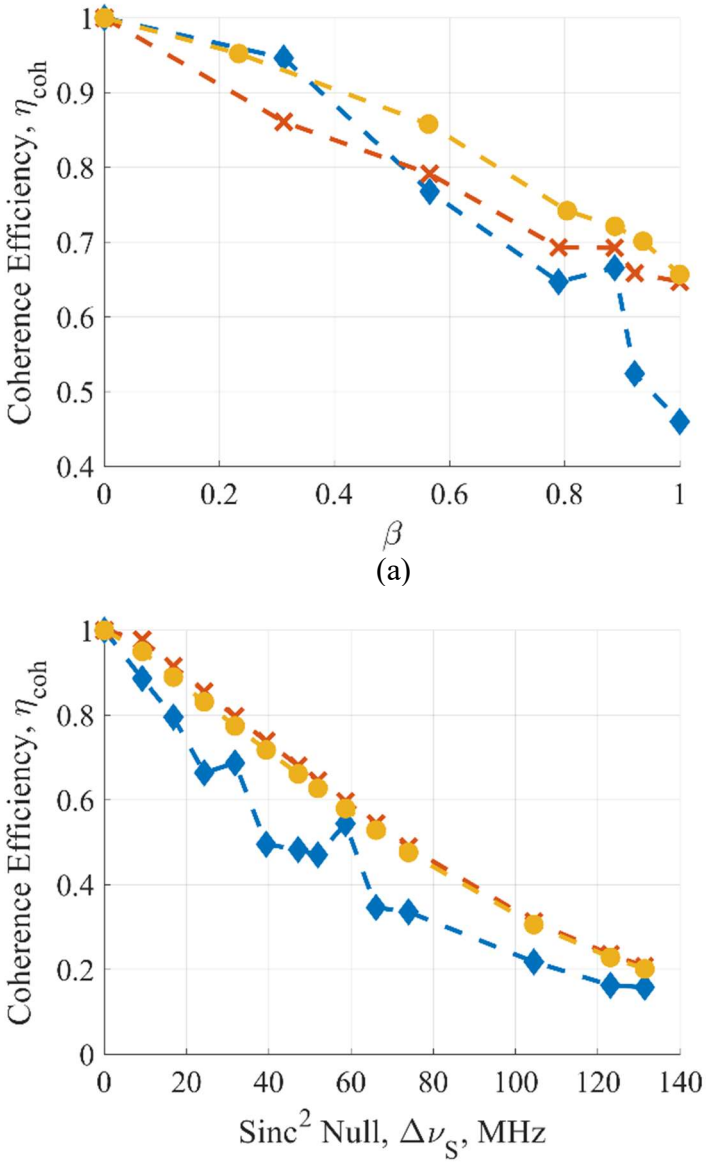

Figure 5.5. Coherence efficiency (- ♦) as (a) v_{PRBS} is held at 100 MHz and (b) V_{p-p} is held to 200 mV. In (a), the theoretical coherence efficiency was calculated using the infinite weighting method ($-\times$) and without weights ($-\bullet$). In (b), the theoretical curves were calculated for the fitted β values ($-\times$) and for $\beta = 1$ ($-\bullet$).

For Fig. 5.5(a), a PRBS frequency of 100 MHz was held constant as the input peak-to-peak voltage changed. This allowed η_{coh} to be characterized as a function of depth of modulation using β as a stand-in variable. Alongside the measured data curve are two theoretical curves calculated using Eq. (5.7). One theoretical curve was generated using the infinite-weighting method described

for Fig. 4. The other theoretical curve fit Eq. (5.3) directly to the phase-modulated CW line shapes with no weighting method. As can be seen in Fig. 5.5(a), the infinite-weighting method was the more accurate method for $\beta > 0.5$ and followed the shape of the measured curve relatively well over the same region. The non-weighted theoretical curve was more accurate for $\beta < 0.4$ and also followed the measured curve shape well over that region. However, neither theoretical curve predicted the entire measured curve well. This indicated the coherence efficiency as presented in Eq. (5.7) is sensitive to minor changes in the input and a slightly more accurate complex degree of coherence would lead to a substantially more accurate prediction.

Fig. 5.5(b) shows the measured coherence efficiency as a function of PRBS frequency while the input peak-to-peak voltage was held at 200 mV. This input voltage was used as it was near the half-wave voltage of the phase modulator. Therefore, the sinc^2 portion of the phase-modulated CW line shape was maximized and the locations of the sinc^2 nulls were as evident as possible. This allowed η_{coh} to be characterized as a function of modulation frequency using $\Delta\nu_S$ as a stand-in variable. As with Fig. 5.5(a), two theoretical curves are presented along with the measured data. One theoretical curve used the β values calculated from the infinitely-weighted line fits and the other substituted those values with $\beta = 1$ (i.e., assumed maximum modulation). Both theoretical curves matched the shape of the measured data curve and relatively matched the magnitude, although both predictions were slightly greater. The $\beta = 1$ curve had lower magnitudes at all modulation frequencies. This was a positive indication as an increased depth of modulation should, and did, lead to a degraded theoretical coherence efficiency.

The higher-magnitude theoretical curves in Figs. 5.5(a) and 5.5(b) were not unexpected. As mentioned in Section 5.3.2, the values for β and $\Delta\nu_S$ were calculated from the fit equations for the phase-modulated CW line shapes, not the phase-modulated pulsed line shapes. Recording

phase-modulated pulsed spectra is non-trivial and was not possible with the available equipment. Also, from previous experiments [34, 47], it was known the amplification processes used for the pulsed laser sources significantly changed the spectral line shape of the CW seed laser and introduced at least one additional longitudinal mode. Therefore, accurate approximations for the reference and signal spectral line shapes could not have been made. Despite this shortcoming, relatively accurate predicted coherence efficiency curves were produced. This indicated the coherence efficiency, as detailed in Section 5.2, was valid and appropriate to characterize the performance of a DH system in a heterodyne-pulsed configuration under the influence of degraded temporal coherence of the laser sources.

5.4.3 Recommendation

While this work focused on the practicalities of using DH systems in deep turbulence applications, there is still a need to further characterize the ambiguity efficiency in terms of source coherence degradation. This would require analyzing a DH system in a homodyne-pulsed configuration. The temporal phase of the reference and signal pulses in a homodyne configuration are identical, meaning any phase modulation within the complex-optical fields of the pulses would perfectly align at the camera FPA when $\tau = 0\,\text{ns}$. This is nearly impossible when a heterodyne configuration is used. Because the phases of the reference and signal pulses are non-deterministically correlated in such a configuration, there is no guarantee phase modulation within the pulses would ever be aligned. This misalignment of phases would increase the number of relative phase changes between the pulses at $\tau = 0\,\text{ns}$ when compared to a homodyne configuration with the same degree of phase modulation. A greater number of relative phase changes leads to a greater number of hologram null shifts within a single collected frame [47] leading to a decrease in total-system efficiency. Therefore, there is an expectation that the total-

system efficiency at $\tau = 0$ ns for a homodyne configuration will be higher than that for a heterodyne configuration when phase modulation is introduced to the source laser.

The deterministic phase correlation between the pulses of a homodyne configuration loses relevance for all $\tau \neq 0$ ns because the phase modulation within the pulses are no longer aligned. This means the same number of relative phase changes between the pulses occur for a given amount of phase modulation regardless of homodyne or heterodyne configuration. Because the homodyne configuration has a dependence on τ that the heterodyne configuration does not, there is an expectation that the ambiguity efficiency for a homodyne configuration will narrow as a function of degree of temporal coherence. The quantification of this effect is necessary to more completely characterize the ambiguity efficiency.

5.5 Conclusion

A digital-holography (DH) system in a heterodyne-pulsed configuration was set up in the off-axis image plane recording geometry. Using this system, the effects of degraded temporal coherence within the laser source, created via spectral broadening, on the ambiguity and coherence efficiencies were characterized. It was found that degraded temporal coherence negligibly affected ambiguity efficiency for this DH configuration. However, the coherence efficiency was found to be sufficient to characterize the performance degradation due the loss of temporal coherence of the laser source.

VI. Conclusion

This dissertation analyzed the efficiencies of a DH system in the pulsed configuration in the off-axis image plane recording geometry through three distinct contributions, with one accepted publication, one submitted publication, and one draft publication. Each contribution increased the understanding of pulsed-source DH. With this new level of knowledge, DH systems in the pulsed configuration can be optimized for use in deep turbulence applications.

The viability of pulsed-source DH in the infrared was shown by quantifying the system efficiencies for a DH system in a homodyne-pulsed configuration. By ensuring the reference and signal pulses had identical phases, the effect of switching from a visible, continuous-wave configuration to an infrared, pulsed configuration was isolated and analyzed. Experimental results showed the total-system efficiency (15.9%), excess-reference-noise efficiency (66.8%), shot-noise-limit efficiency (79.8%), and mixing efficiency (29.2%) of a system in the infrared, pulsed configuration were consistent with the efficiencies of a system in the visible, CW configuration [17]. Therefore, the only efficiency introduced by switching configurations was a novel efficiency, called the ambiguity efficiency. The ambiguity efficiency was necessary to account for the temporal delay between the pulses of a pulsed configuration. An expression for this efficiency was formulated and experimentally validated with a DH system in the homodyne-pulsed configuration. Through validation, the ambiguity efficiency was shown to be robust to multi-mode behavior and excess camera noise.

Due to engineering constraints though, a DH system in a homodyne-pulsed configuration is not tenable for deep turbulence applications. However, using a heterodyne-pulsed configuration would circumvent these issues. But, there was a concern that changing to a heterodyne configuration may introduce additional efficiencies as the phases of the pulses are not

deterministically correlated. Therefore, the total-system and ambiguity efficiencies of a DH system in the heterodyne-pulsed configuration were quantified. The experimental results showed the total-system efficiency (13.5%) of a DH system in a heterodyne-pulsed configuration was consistent with that of a DH system in a homodyne-pulsed configuration [34]. Furthermore, the ambiguity efficiencies of the two configurations were also consistent. These were strong indications that no new component efficiencies were required to characterize a DH system in a heterodyne-pulsed configuration. Additionally, a model was introduced and used to strengthen the validation of the ambiguity efficiency.

The effects of degraded temporal coherence of the laser source, via spectral broadening, on a DH system in a heterodyne-pulsed configuration were then investigated. For this configuration, experiments showed spectral broadening of the laser source did not significantly affect the ambiguity efficiency. The total-system efficiency, however, did change as a function of temporal coherence degradation. These results can be used to begin building a design trade-space for implementing a DH system in a heterodyne-pulsed configuration into deep turbulence applications.

6.1 Recommendations for future work

Future work concerning efficiency quantification for pulsed-source DH systems can be separated into two categories: (1) can be accomplished with data already collected and (2) requires new data to be collected. The first category consists of a single topic and focuses on achieving the shot-noise limit via data processing. The second category spans four topics, each of which will be discussed below.

6.1.1 Using Current Data

With the data collected for the experiments detailed in Chapters III through V, the performance of a pulsed-source DH system operating in the shot-noise limit could be estimated. Similar analysis for partially-coherent CW-source DH systems has already been completed [20]. Using a combination of frame subtraction and frame averaging, the SNR of this CW system was sufficiently increased such that it achieved a shot-noise-limited regime. The same techniques can be applied to the pulsed-source DH holograms already collected. Doing so would potentially remove the effect of the significant camera dark current and reference pulse non-uniformity seen in all three experiments. This analysis would not only produce an estimate of pulsed-source DH system performance in a shot-noise-limited regime, but also quantify the amount of image-post-processing necessary to achieve the shot-noise limit for different degrees of temporal coherence within the sources.

6.1.2 Requires New Data

For the remaining future work recommendations, new experiments need to be designed and performed. The first such experiment should look at the ambiguity efficiency as a function of Doppler-frequency shift. All of the work presented in this dissertation assumed the Doppler-frequency shift was zero, but that may not be realistic for deep-turbulence applications. For instance, the relative velocity between the object of interest and the platform using the DH systems discussed in the above experiments would need to be around 100 m/s or greater for the Doppler-frequency shift to be non-negligible. The ambiguity efficiency is already suited to handle the Doppler-frequency shift, but verification through experimentation is required. Doing so will increase the design trade-space and allow system designers to compensate for Doppler-frequency shift.

A second experiment, or set of experiments, should investigate the effect on the total-system and ambiguity efficiencies when the laser source is degraded by means other than PRBS. The ambiguity efficiency may not remain constant for all types of temporal degradation, so other phase modulation schemes, such as sinusoidal phase modulation, should be examined. Additionally, spatial coherence was ignored throughout this dissertation. However, the partial-transverse coherence of the reference and signal fields undoubtedly affected the measured results. Such a study would be difficult due to instrumentation limitations, but results would be significantly beneficial to the field of digital holography.

Within a similar vein, the changes to the ambiguity efficiency as a function of PRBS bit alignment should be measured. If the bit sequences of the reference and signal pulses are perfectly aligned, the ambiguity efficiency should be greater than when the sequences are misaligned. There are two potential experiments capable of analyzing this relationship. One involves using the homodyne-configuration and very accurate and precise path length differences. On average, this should lead to a narrow spike in ambiguity efficiency at with no other changes. The second experiment involves fine-tuning the CW seed laser phase modulation. With sufficient control, the bits of the modulation sequence could be consistently overlapped as desired. This would lead to perfect bit overlap at any desired amount of pulse overlap. It would also enable measurement of the desired efficiencies when the bit sequence of the pulses was exactly one bit off, two bits off, etc.

A fourth research area should examine the performance of a hybrid-configuration DH system; one where the reference beam is CW and the signal beam is pulsed. A hybrid-configuration would eliminate the need for the ambiguity efficiency while still circumventing the coherence length problem associated with purely CW-configurations. However, this benefit may be

outweighed by the increase in noise due to the CW reference. Quantifying this trade-off would assist when selecting the configuration for a desired application.

Appendix A. Special functions

Fourier Transform

$$F\left\{g\left(x_1\right)\right\}=\int_{-\infty}^{\infty} g\left(x_1\right)e^{-i2\pi x_1 x_2}dx_1 \tag{A.1}$$

Inverse Fourier Transform

$$F^{-1}\left\{g\left(x_1\right)\right\}=\int_{-\infty}^{\infty} g\left(x_1\right)e^{i2\pi x_1 x_2}dx_1 \tag{A.2}$$

Kronecker Delta

$$\delta(x)=\begin{cases}1, x=0\\ 0, x\neq 0\end{cases} \tag{A.3}$$

Circle Function[1]

$$\mathrm{Circ}(r)=\begin{cases}0, & r>0.5\\ 0.5, r=0.5\\ 1, & r<0.5\end{cases} \tag{A.4}$$

Rectangle Function

$$\mathrm{Rect}(x)=\begin{cases}0, & |x|>0.5\\ 0.5, |x|=0.5\\ 1, & |x|<0.5\end{cases} \tag{A.5}$$

[1] $r=\sqrt{x^2+y^2}$

Appendix B. Pulse diagnostic measurements

To inform the results presented in Section 3.4, pulse diagnostic measurements were obtained. For this purpose, Fig. B.1 shows the temporal profile and spectral line shape of the pulses. The temporal profile, as measured using a Thorlabs DET08C photodetector, is shown in Fig. B.1(a), and the spectral line shape, as measured using a Thorlabs SA200-8B scanning Fabry-Perot interferometer with a 7.5 MHz resolution and 1.5 GHz free spectral range, is shown in Fig. B.1(b) [54, 55].

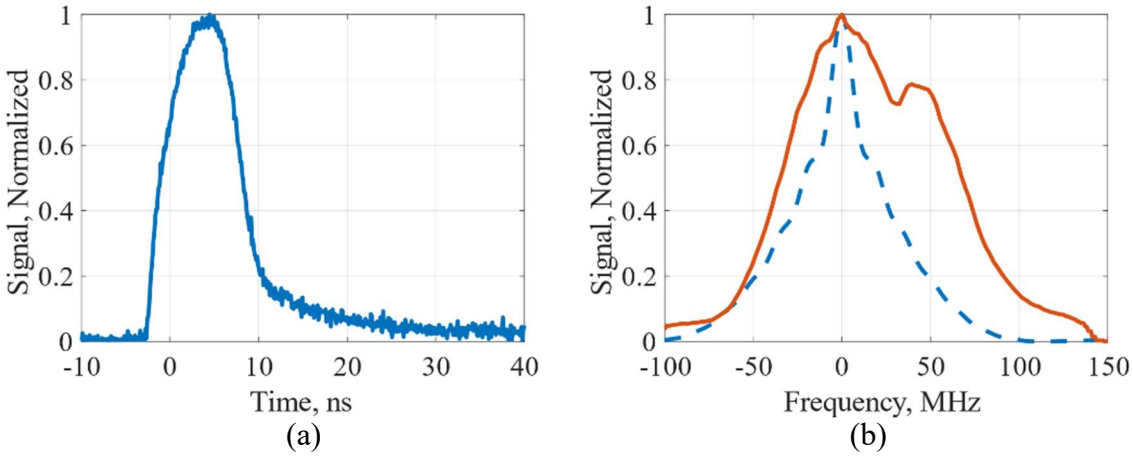

Figure B.1. Pulse diagnostic measurements of (a) temporal profile and (b) spectral line shape, where the measured spectral line shape (–) is compared to the Fourier transform of the temporal profile (--).

The temporal profile in Fig. B.1(a) showed that the pulsed laser source produced 10 ns pulses with tails that were 10s of nanoseconds long. Moreover, the measured spectral line shape in Fig. B.1(b) appeared to contain two spectral peaks spaced approximately 50 MHz apart with the right peak at approximately 80% the amplitude of the left peak. A comparison between the measured spectral line shape and the Fourier transform of the temporal profile indicated that the pulsed laser source did not produce Fourier transform limited pulses [56]. Simply put, the measured spectral line shape was wider than the Fourier transform of the temporal profile. For this

reason, the spectral formulation [see the right-most term of Eq. (3.8)] was used in Appendix C to obtain predicted values for the ambiguity efficiency.

The multi-peaked nature of the measured spectral line shape in Fig. B.1(b) strongly indicated multi-mode operation within the pulsed laser source. In particular, the CW seed laser had a longitudinal mode spacing on the order of 3 GHz and a corresponding transverse mode spacing on the order of 1.5 GHz, both of which were significantly larger than the measured 50 MHz separation [61]. However, if the 1.5 GHz free spectral range of the Fabry-Perot interferometer was taken into account, the observed double-peaked line shape could have been the result of two overlapping scanned spectra. For example, if two subsequent Fabry-Perot interferometer scans were labeled "a" and "b", the secondary mode of scan "a" was overlapped with the fundamental mode of scan "b". To investigate the nature of this potential secondary mode, the pulse train was expanded and the spatial profile was visually inspected using a Xenics Xeva-FPA-1.7-320 camera. A sample spatial profile measurement (with a normalized scale after computing the square root of the raw camera data) is shown in Fig. B.2.

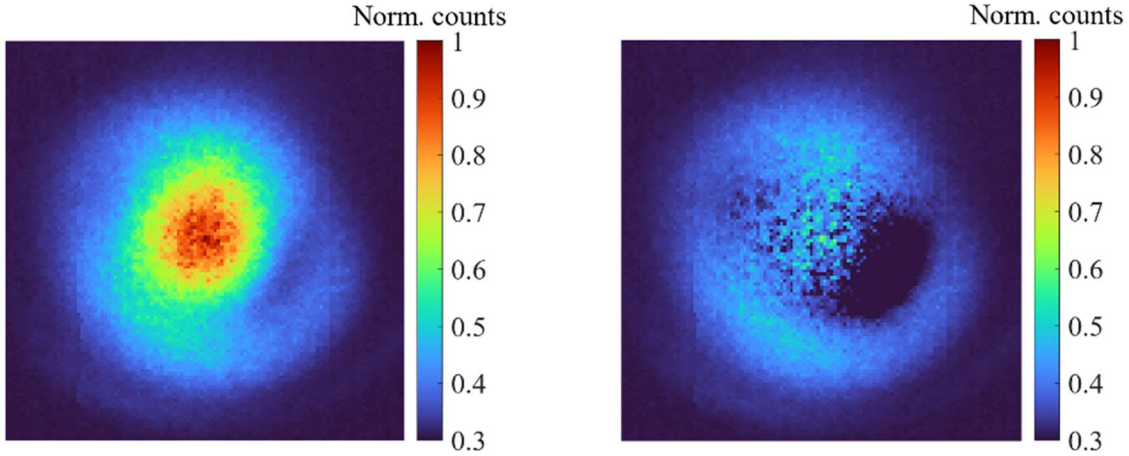

(a) (b)

Figure B.2. Pulse diagnostic measurement of (a) the entire spatial profile and (b) the spatial profile with the fundamental mode removed.

As shown in Fig. B.2(a), the spatial profile indicated the presence of at least two modes. This is confirmed in Fig. B.2(b), which shows the spatial profile of the beam after the fundamental mode (assumed to be a Gaussian (0,0) mode) was removed. As such, the analysis suggested that the pulsed laser source produced a secondary mode consistent with a Laguerre-Gauss (1,0) mode with an astigmatic phase shift [62, 63] This determination was made after taking into account the measured spectrum in Fig. 3.4(b), the mode spacing of the CW seed laser, the free spectral range of the Fabry-Perot interferometer, and the spatial profile in Fig. B.2(b).

Appendix C. Multi-mode fit to the ambiguity efficiency

The pulse diagnostic measurements from Appendix B were used to inform a multi-mode fit to the ambiguity efficiency formulated in Section 3.2 [see the right-most term in Eq. (3.8)]. For simplicity, the spectrum was assumed to be comprised of two modes of the same width, and each mode was assumed to have a Lorentzian line shape, since the pulsed laser source was assumed to be phase noise dominated [64, 65]. Using these assumptions, a linear-least squares regression fit was performed on the spectral line shape [see Fig. B.1(b)] to calculate a fitted equation with the adjusted R^2 fit value of 0.985 and standard error of 3.8%. The right peak of the resulting equation was then shifted 1.5 GHz to the positive-frequency side to account for the overlapping spectra and the free spectral range of the Fabry-Perot interferometer. As a result,

$$f(\nu) = A_1 \frac{\Delta\nu^2}{(\nu - \bar{\nu}_1)^2 + \Delta\nu^2} + A_2 \frac{\Delta\nu^2}{(\nu - \bar{\nu}_2)^2 + \Delta\nu^2}, \tag{C.1}$$

with the multi-mode fit parameters listed in Table C.1. It is important to note that Gaussian and Voigt line shapes were also considered but did not fit as well as the assumed Lorentzian line shape. The multi-mode fit predicted by Eq. (C.1) are shown in Fig. C.1(a).

Table C.1. Multi-mode fit parameters.

Variable	Symbol	Value	Units	95% Confidence Bounds
Amplitude, Fundamental Mode	A_1	0.88	A.U.	(0.869, 0.883)
Center Frequency, Fundamental Mode	$\bar{\nu}_1$	-4.26	MHz	(-4.48, -4.03)
Amplitude, Transverse Mode	A_2	0.57	A.U.	(0.56, 0.58)
Center Frequency, Transverse Mode	$\bar{\nu}_2$	1546.88	MHz	(1546.54, 1547.21)
Half-Width, Half Maximum	$\Delta\nu$	27.87	MHz	(27.60, 28.14)

Substituting Eq. (C.1) into the right-most term of Eq.(3.8), where $f(\nu) \approx \tilde{U}_R^*(\nu)\tilde{U}_s(\nu)$, resulted in the following expression for the ambiguity efficiency:

$$\eta_{amb}(\tau) = A_1^2 \Delta\nu^4 \, exp\left(-4\pi\Delta\nu|\tau|\right) + A_2^2 \Delta\nu^4 \, exp\left(-4\pi\Delta\nu|\tau|\right) + A_1 A_2 \Delta\nu^4 \, exp\left(-i2\pi\tau(\nu_1 - \nu_2)\right) exp\left(-4\pi\Delta\nu|\tau|\right) + A_1 A_2 \Delta\nu^4 \, exp\left(-i2\pi\tau(\nu_2 - \nu_1)\right) exp\left(-4\pi\Delta\nu|\tau|\right) . \quad \text{(C.2)}$$

For further simplicity, and in accordance with common practice, it was assumed the modes were statistically independent, meaning the modes did not interact with one another [42]. This assumption resulted in each peak from Eq. (C.1) being independently substituted into the right-most term of Eq. (3.8) to generate independent terms. In turn,

$$\eta_{amb}(\tau) = A_1^2 \Delta\nu^4 \, exp\left(-4\pi\Delta\nu|\tau|\right) + A_2^2 \Delta\nu^4 \, exp\left(-4\pi\Delta\nu|\tau|\right). \quad \text{(C.3)}$$

As can be seen by comparing Eqs. (C.2) and (C.3), treating the modes as being statistically independent removes the complex cross terms. The multi-mode fit to the ambiguity efficiency predicted by Eq. (C.3) are shown in Fig. C.1(b).

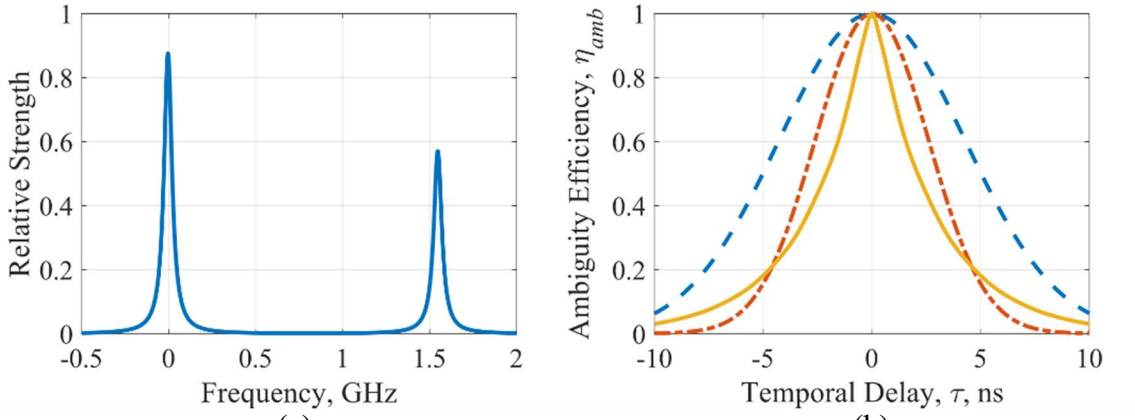

Figure C.1. (a) The predicted multi-mode fit and (b) the predicted ambiguity efficiency assuming the Lorentzian spectral line shape (–), as well as the measured spectral line shape (-·) and a Gaussian baseline (--).

As shown in Fig. C.1(b), Eq. (C.3) was plotted alongside the predicted ambiguity efficiency assuming the measured spectral line shape [see Fig. B.1(b)] and a baseline 10 ns, Fourier-transform-limited Gaussian pulse [56]. In general, the predicted ambiguity efficiency associated with the Lorentzian spectral line shape was narrower than that associated with the measured

spectral line shape for $|\tau| \leq 4.5$ ns and the Gaussian baseline for $|\tau| \leq 12.5$ ns. At $|\tau| = 1$ ns, the predicted ambiguity efficiency associated with the Lorentzian spectral line shape was approximately 74%, nearly 20% worse than that predicted with the measured spectral line shape and 24% worse than the Gaussian baseline.

Appendix D. Complex phase effects on a pulsed-source digital holography system

The contents of this appendix was published in *Proceedings of SPIE: Defense + Commercial Sensing*, 1209206, on 30 May 2022 [48].

The signal-to-noise ratio (SNR) of a digital holography (DH) system is degraded by the total system efficiency, which is comprised of many terms. For pulsed-laser source DH systems, the total-system efficiency is dependent on the amount of temporal overlap between the signal and reference pulses. This temporal overlap not only accounts for the amplitudes of the pulses but also for the phase, which may cause degradations to the achievable SNR. A previous effort formulated a model for the effect of temporal overlap in terms of the ambiguity efficiency [34]. The outputs from the model were compared to measured results obtained using a 1064 nm pulsed-laser source DH system. Initial comparisons showed the model insufficiently accounted for one or more causes of performance degradation, leading to an over-prediction of performance. Two likely causes, mode hopping and linear frequency modulation (LFM), were investigated. It was found both could account for the over-prediction in the model, indicating the model used in the previous effort is valid.

D.1 Introduction

Holography is a robust, accurate wavefront sensing method well-suited for deep-turbulence environments [4]. This coherent beam measurement technique uses a strong reference beam to provide shot-noise limited performance in low signal-to-noise (SNR) scenarios [6-9, 22]. The digitization of the holography process, or digital-holography (DH), has expanded the usability of holography systems due to increased ease and speed of data processing. This, coupled with

improved commercial digital camera technology, has led to DH becoming a potential candidate for long-range imaging and turbulence measurement applications [11-16, 35-36].

In order for the use of DH to be maximized, DH system performance needs to be fully understood. A convenient way to gain this understanding is to identify and measure individual sources that cause SNR loss, or, in other words, quantify the system efficiencies. To this effect, many studies have investigated and characterized continuous-wave (CW) sourced DH systems in terms of efficiencies [17-20]. Using CW sources provides highly longitudinally-coherent beams for interference, but limits the effective range of DH systems due to power restrictions [18, 21]. On the other hand, using pulsed sources offer greater power, and therefore range, at the cost of longitudinal coherence. Also, the introduction of pulses means the total system efficiency of a pulsed-source DH system is a function of how well the pulsed beams overlap, in time, at the point of detection.

A recent experiment investigated this new efficiency for pulsed-source DH systems, called the ambiguity efficiency [34]. To confirm the ambiguity efficiency was the only efficiency introduced when switching from CW to pulsed sources, a predictive model was constructed based on the well-known ambiguity function [31, 41]. The model accurately predicted system performance when the pulsed beams were well overlapped but over-predicted performance as that overlap diminished [34].

This paper investigates and reports on two potential solutions to this over-prediction: including either a mode hop within the laser source or a linear frequency modulation, also known as a chirp, to the model. To do so, Section D.2 introduces the ambiguity efficiency and the two potential solutions and Section D.3 briefly describes the experiment that motivated the deeper dive into the model. Section D.4 introduces a simplified version of the model that solely focuses on the

ambiguity efficiency, then analyzes the effect of the two potential solutions. The analysis will show both the mode hop and chirp are valid solutions to the over-prediction in the model. It should be noted that this result does not indicate a unique solution, but that at least two valid solutions among many potential solutions exists. Also, these solutions are only guaranteed to be valid for the specific scenario presented in Sections D.3 and D.4. For any other scenario, these two potential solutions must be re-evaluated. The paper then concludes with a summary of results in Section D.5.

D.2 Theory

Multiple DH recording geometries exist and each has different benefits [6-9, 21]. Many previous studies [6, 17-22], including the pulsed-source DH experiment serving as the basis for this paper [34], used the off-axis image plane recording geometry (IPRG) due to the simplicity in setup. The off-axis IPRG involves interfering light reflected off of an object and focused through a pupil, known as the signal field [22], with a strong reference field. When quantifying efficiencies for DH systems in the off-axis IPRG, it is convenient to use the power definition of the SNR [6, 22] such that

$$SNR(x,y,\tau) = \eta_{tot}(x,y,\tau)\frac{4q_I^2}{\pi}\bar{m}_S(x,y), \tag{D.1}$$

where (x,y) are the estimated image-plane coordinates, τ is the temporal delay between the centers of the reference and signal fields (only necessary for pulsed-source DH systems), η_{tot} is the total-system efficiency, q_I is the image-plane sampling quotient, and $\bar{m}_S$ is the per-pixel mean number photoelectrons generated by the signal field. It is important to note Eq. (D.1) assumes the DH system is operating at the shot-noise-limit [20, 22]. However, Eq. (D.1) remains valid in non-

shot-noise-limited scenarios because any adverse effects caused by the system not operating in the shot-noise-limit is captured by η_{tot} [17].

In practice, η_{tot} is comprised of many independent, multiplicative efficiencies. For the purposes of this paper, the only one of these efficiencies discussed in detail will be the ambiguity efficiency, η_{amb}. The ambiguity efficiency is a measure of the temporal coherence between the reference and signal fields and is derived from the zero-Doppler cut of the ambiguity function [31, 32, 41], such that

$$\eta_{amb}(\tau) = \left\langle \left| \int_{-\infty}^{\infty} U_R(x,y,t) U_S^*(x,y,t-\tau)\, dt \right|^2 \right\rangle = \left\langle \left| \int_{-\infty}^{\infty} \tilde{U}_R^*(x,y,\nu) \tilde{U}_S(x,y,\nu) e^{j2\pi\nu\tau} d\nu \right|^2 \right\rangle \quad \text{(D.2)}$$

where U_R and U_S are the complex-optical fields of the reference and signal pulses (in the temporal domain), respectively, t is time, $\tilde{U}_R$ and $\tilde{U}_S$ are complex-optical fields of the reference and signal pulses (in the spectral domain), respectively, ν is frequency, $*$ denotes the complex conjugate, $|\bullet|^2$ is the square-magnitude operator, and $\langle \bullet \rangle$ is the spatial average operator. The square-magnitude operator is necessary because the power definition of SNR was used in Eq. (D.1). It should be noted the spatial dependence need not be strictly Cartesian, but can be any 2-dimensional spatial coordinate system.

For CW-sourced DH systems, the ambiguity efficiency is trivially equal to one as long as the path-length-difference between the reference and signal fields is less than the longitudinal coherence length of the source laser beam. On the other hand, the ambiguity efficiency can be the dominant efficiency in pulsed-source DH systems. In these systems, the ambiguity efficiency only equals one when the pulses are perfectly overlapped in time (i.e. $\tau = 0$) and is less than one at all other values of τ.

A previous experiment [34] used Eq. (D.2) as the basis for a predictive model. This model worked well for $\tau \leq 1$ ns but overestimated the measured ambiguity efficiency for all other τ. The overestimation pointed not to the model being incomplete, but to the model inputs being inaccurate. The complex-optical fields used to calculate Eq. (D.2) were estimated from diagnostic measurements taken using a fast photodiode in the temporal domain and a Fabry-Perot interferometer in the spectral domain. While taking these diagnostic measurements, it is possible that important details were lost. This paper investigates two such details and whether either or both could be solutions to the overestimation in the model created for the pulsed-source DH experiment. For this reason, these details are referred to as potential solutions for the remainder of this paper. It is important to note that many other potential solutions exist and any one potential solution being valid does not indicate a unique solution. Additionally, the validity of the solution in the scenario described below does not guarantee validity in any other scenario.

The first potential solution under consideration is a frequency change, or mode hop, within the laser. Multi-mode behavior was observed in the pulsed-source DH efficiency quantification experiment and it was assumed that both modes were propagating at the same time [34]. However, it is also possible that at some point in time during the pulse, the laser frequency shifted from one mode to the other. Neither the temporal nor spectral domain diagnostic measurements would show preference to either possibility. Therefore, this paper will investigate the effect on the laser diagnostics and predicted ambiguity efficiency of changing the complex component of the complex-optical fields from $exp\left(j\omega_1 t\right)$ to $exp\left(j\omega_2 t\right)$, where ω_1 and ω_2 are the angular frequencies of modes one and two, respectively.

The second potential solution under consideration is the presence of a linear frequency modulation, or chirp, within the laser. A chirp is a quadratic exponential factor with respect to time

and has been shown to have deleterious effects on ambiguity functions [32, 33]. This last point is key because the construction of the laser source used during the pulsed-source DH experiment included two fiber Bragg gratings [45]. Fiber Bragg gratings are sensitive to temperature variations such that the wavelength passed by the grating can gain a chirp on the order of tens to hundreds of mega-Hertz for temperature changes in the single-digit milli-Kelvins [66, 67]. Consequently, it is possible that small temperature variations within the laser injected an unintentional chirp. The temporal diagnostic measurement will not change with the inclusion of a chirp, but the change to the spectral diagnostic measurement will vary with the bandwidth of the chirp. Therefore, this paper will investigate the effect on the laser diagnostics and predicted ambiguity of a chirp on the complex-optical fields in the form of $exp\left(j\pi t^2\beta/T\right)$, where β is the bandwidth of the chirp and T is the full-width, half-maximum (FWHM) of the temporal pulse [33].

D.3 Review of Experiment

To better understand the intent of this paper and the results presented in Section D.4, a brief review of the pulsed-source DH experiment is presented here. For greater detail on experimental parameters, setup, measurement, and results, please refer to Ref. [34]. A 1064 nm pulsed laser source producing 10 ns pulses and a short-wave infrared camera were used to measure the total-system efficiency of a DH system in the off-axis IPRG. The measured temporal profile and spectral line shape of the pulses are shown in Fig. D.1.

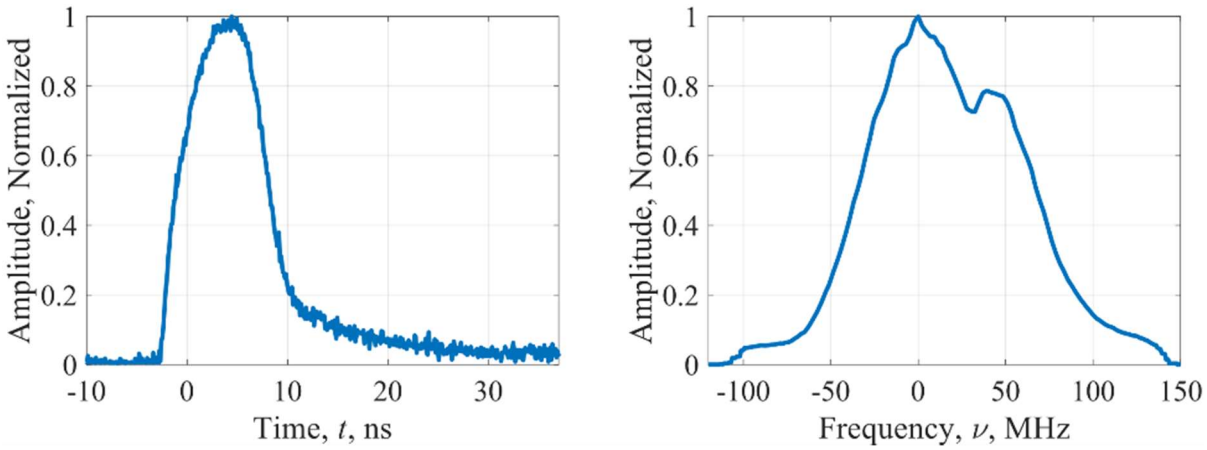

(a) (b)

Figure D.1. Measured (a) temporal profile and (b) spectral line shape of the pulses from the pulsed-source DH experiment described in Ref. [34].

A seen in Fig. D.1(a), the temporal profile is roughly a super-Gaussian of the second order with a 10 ns FWHM and a tail lasting for at least tens of nanoseconds. Fig. D.1(b) shows at least two modes, each with a FWHM of 70 MHz, where one mode has been aliased on top of the other due to measurement device limitations [34]. Subsequent spatial profile measurements of the pulses confirmed the multi-mode nature of the beam. Analysis showed the fundamental mode, or the mode centered at 0 Hz in Fig. D.1(b), was consistent with a Laguerre-Gauss ($p = 0, l = 0$) mode. Furthermore, the secondary mode, or the mode centered near 50 MHz in Fig. D.1(b), was consistent with a Laguerre-Gauss ($p = 1, l = 0$) mode. From the laser construction parameters, the total spacing between these modes is approximately 1.55 GHz [34].

The laser pulses were amplitude-split with a polarizing beam splitter to create the reference and signal fields. This amplitude-splitting ensured maximum coherence between the two fields at the point of detection. The SNR was measured as a function of pulse overlap, or the path-length difference between the reference and signal fields, which was systematically changed via an optical trombone. From these overlap-dependent SNR measurements, a measured total-system

efficiency curve was calculated. The normalization of the measured total-system efficiency curve is the measured ambiguity efficiency.

This measured ambiguity efficiency was compared against the prediction made using Eq. (D.2) and complex-optical field estimates made from the laser diagnostics in Fig. D.1. For specifics on this process, please refer to the appendices of Reference [34]. The comparison is shown in Fig. D.2.

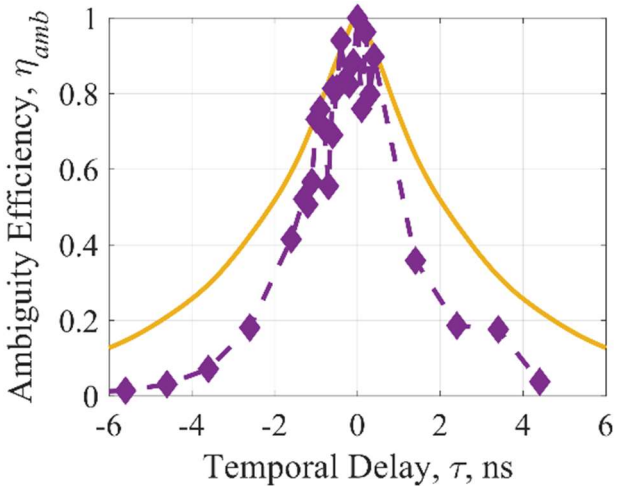

Figure D.2. Predicted vs. measured ambiguity efficiency for the pulsed-source DH system described in Ref. [34].

Fig. D.2 shows the ambiguity efficiency model based on Eq. (D.2) accurately predicted system performance when $\tau \leq 1$ ns but overestimated outside this region. For a convenient metric, the FWHM of the measured ambiguity efficiency was 59% of the predicted value. Therefore, in order to validate the ambiguity efficiency model presented in the pulsed-source DH experiment [34], changes must be made to either the model or the model inputs to increase the accuracy of the predicted ambiguity efficiency.

D.4 Model Results

After analyzing the model and model inputs, it has been determined the most likely cause of the disparity between the predicted and measured ambiguity efficiencies was inaccuracy in the

estimated complex-optical fields. Specifically, the complex-phase measurement made using the Fabry-Perot interferometer (see Fig. D.1(b)) may have produced an incomplete picture of the spectral behavior of the laser pulses. One potential issue with the reported spectral line shape is the nature of modal propagation. At least two distinct modes are evident in Fig. D.1(b). But, as mentioned in Section D.2, it is unknown whether both modes were propagating simultaneously or if there was a mode hop in the laser source. A second potential issue is the masking of spectral features, such as a chirp in the laser source, due to low SNR or measurement technique [54, 55]. Both of these potential issues could result in a narrower-than-expected ambiguity efficiency and are investigated below.

To isolate and highlight the effect of each potential issue, a simplified complex-optical field model will be presented. Using the simplified model, the entire complex-optical field can be defined and the need for estimations is eliminated. From these idealized fields, the idealized laser diagnostics and ambiguity efficiency will be calculated. On an individual basis, the complex-phase factors associated with the two potential solutions identified in Section D.2 will be included in the model and change the idealized fields. For each potential solution, the effect on the laser diagnostics and ambiguity efficiency will then be analyzed.

Before introducing the model used for this paper, it is important to clarify the meaning of the results. The effect of each potential solution is highly dependent on the idealized inputs to the model. For instance, whether a potential solution is valid or not for a temporally Gaussian set of fields is not necessarily consistent across all possible temporal fields. Also, the validity of a potential solution does not guarantee uniqueness. It is possible that more than one potential solution is valid. It is also possible that the true solution is a combination of potential solutions that are, by themselves, not valid. This paper seeks not to identify the exact cause of the overestimation

seen in the pulsed-source DH experiment, but to investigate whether that overestimation could have been caused by using inaccurate complex-optical field estimates. If so, it will be a strong indication that the model used to predict pulsed-source DH system performance is valid.

D.4.1 Simplified Model

Because estimating complex-optical fields from data can lead to inaccuracies, a model was created to allow the fields to be completely defined. While the model was structured so that the resulting complex-optical fields produced similar laser diagnostics as the pulsed-source DH experiment (see Fig. D.1), multiple simplifying features were included. This simplification was done to highlight the effect of each potential solution on the laser diagnostics and predicted ambiguity efficiency.

In the model, each complex-optical field had two modes spaced 1.55 GHz apart in frequency. Spatially, both modes were set to be Laguerre-Gauss modes. The fundamental modes were set to be of order $p=0$, $l=0$ and the secondary modes were set to be of order $p=1$, $l=0$, such that

$$U_1^{R,S}(r,\phi,z) = A_1\left(\frac{w_0^{R,S}}{w(z)^{R,S}}\right) exp\left(-\frac{r^2}{w^2(z)^{R,S}} - jk_1\frac{r^2}{2R_1(z)^{R,S}} + j\left[2p_1+1\right]\tan^{-1}\left(\frac{z^{R,S}}{z_{R,1}^{R,S}}\right)\right) \tag{D.3}$$

and

$$\begin{aligned} U_2^{R,S}(r,\phi,z) = {} & A_2\left(\frac{w_0^{R,S}}{w(z)^{R,S}}\right) \\ & exp\left(-\frac{r^2}{w^2(z)^{R,S}} - jk_2\frac{r^2}{2R_2(z)^{R,S}} + j\left[2p_2+1\right]\tan^{-1}\left(\frac{z}{z_{R,2}^{R,S}}\right)\right)\left(1-\frac{2r^2}{w^2(z)^{R,S}}\right) \end{aligned} \tag{D.4}$$

where the superscripts R and S indicate the reference and signal fields, respectively, the subscripts 1 and 2 indicate the fundamental and secondary modes, respectively, (r,ϕ) are radial

coordinates at longitudinal distance z, A is the amplitude multiplier used to control the energy in each mode, w_0 is the beam waist, $w(z)$ is the beam radius at z, k is the wavenumber, $R(z)$ is the radius of curvature at z, p is the radial index, and z_R is the Rayleigh range. All variables except A in Eq. (D.3) were chosen such that the spatial distribution of the reference field was consistent with a spherical wave in the far-field and the spatial distribution of the signal field was approximately 4.5 mm at the $1/e$ width. The amplitude multipliers A were chosen so each mode had roughly the same energy as the corresponding mode from the pulsed-source DH experiment [34].

Temporally, both fields were given the temporal profile shown in Fig. D.1(a). Both modes in each field were made spectrally pure with Lorentzian line shapes. Therefore, the temporal elements for each mode are

$$U_n(t) = A_t(t)\, exp(j\omega_n t), \tag{D.5}$$

where n is the mode number, A_t is the temporal amplitude, and ω is the angular frequency of the mode.

Combing Eqs. (D.3)-(D.5), and assuming there is no loss in transverse coherence, the idealized complex-optical fields used in this model are

$$U_R(r,\phi,t) = U_1^R(r,\phi)U_1(t) + U_2^R(r,\phi)U_2(t) \tag{D.6}$$

and

$$U_S(r,\phi,t) = U_1^S(r,\phi)U_1(t) + U_2^S(r,\phi)U_2(t), \tag{D.7}$$

where the dependence on z has been hidden as it does not affect the ambiguity efficiency calculation and will not be relevant to future analysis. With the fully defined fields from Eqs. (D.6)

and (D.7), the ambiguity efficiency was calculated using Eq. (D.2). The temporal diagnostic, spectral diagnostic, and ambiguity efficiency are shown in Fig. D.3.

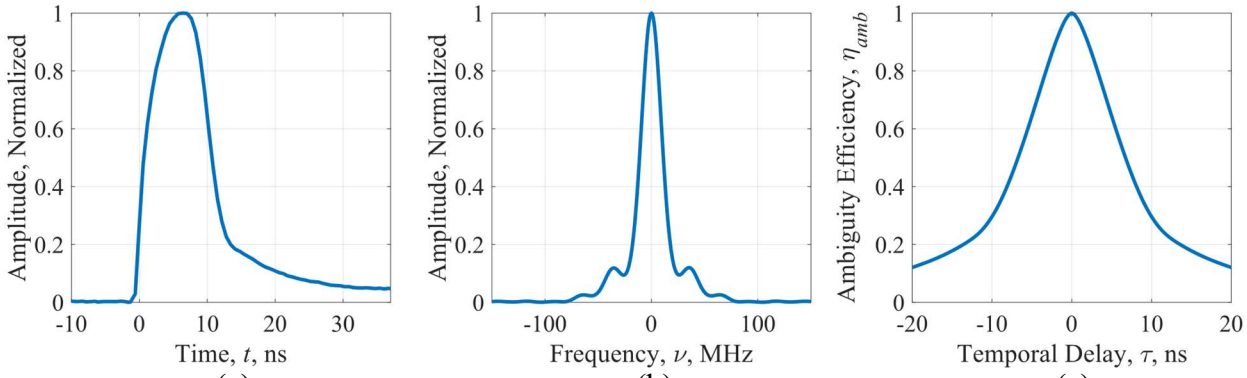

(a) (b) (c)

Figure D.3. The (a) temporal diagnostic, (b) spectral diagnostic, and (c) ambiguity efficiency calculated using the complex-optical fields from Eqs. (D.6) and (D.7).

For both Fig. D.3(a) and Fig. D.3(b), the diagnostic was evaluated at $r = 0$ to mimic the measurements collected using the fast photodiode and Fabry-Perot interferometer in the pulsed-source DH experiment. Also, only the fundamental mode is shown in Fig. D.3(b) so the spectral features can be seen clearly. The secondary mode is 48% of the amplitude of the fundamental mode, but is identical in all other aspects. Therefore, there is no loss of information by only showing the fundamental mode. This holds for all results shown later in this paper. The results shown in Fig. D.3 will be used as comparisons for the effects of the potential solutions discussed in Section D.2. For a potential solution to be considered valid, the inclusion of the potential solution must result in only minor changes to the line shapes of the diagnostics but must also narrow the ambiguity efficiency to 59% of the idealized FWHM.

D.4.2 Mode Hop

In accordance with the pulsed-source DH experiment [22], it was assumed both modes in the complex-optical fields in Eqs. (D.6) and (D.7) propagate simultaneously. However, with regard to the laser diagnostics, it is possible that the laser from which the pulses were carved instead

experienced a frequency change. This "hop" from the fundamental mode to the secondary mode adds a temporally-dependent binary trigger to the temporal fields for each mode such that

$$U_n(t) = \Phi_n(t - t_0) \bullet A_t(t)\, exp(j\omega_n t), \tag{D.8}$$

where $\Phi(t - t_0)$ is similar to a unit-step function that activates or deactivates the mode at a specified time t_0. In other words, the temporal field for the fundamental mode "turns off" and the temporal field for the secondary mode "turns on" at t_0. The specified time is determined by matching the energy in each mode to the corresponding mode from the pulsed-source DH experiment.

Using Eq. (D.8) as the temporal fields in Eqs. (D.6) and (D.7), the ambiguity efficiency was calculated according to Eq. (D.2). The diagnostics and ambiguity efficiency are shown in Fig. D.4.

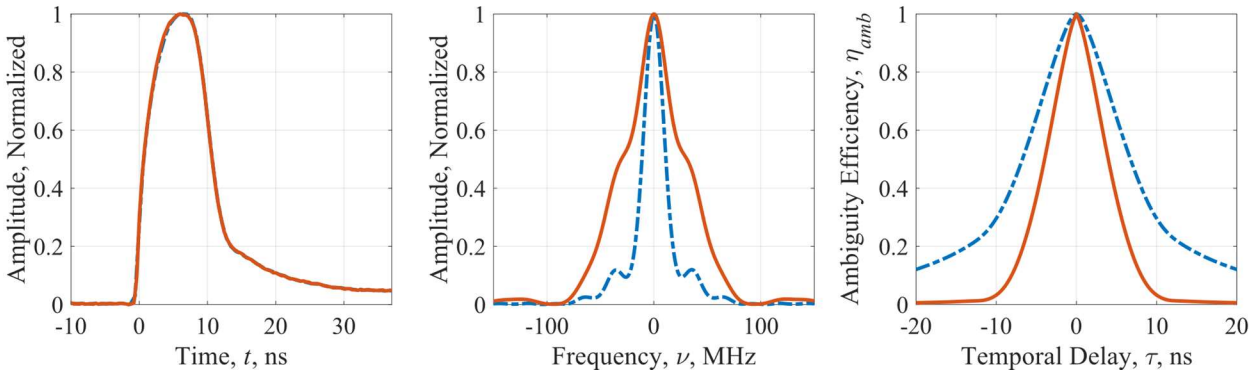

Figure D.4. The (a) temporal diagnostic, (b) spectral diagnostic, and (c) ambiguity efficiency calculated for the laser mode hop scenario. For all plots, the calculations which included the mode hop (–) are compared with the idealized calculations (– ·).

As seen in Fig. D.4, including a mode hop does not affect the temporal diagnostic significantly and only slightly broadens the spectral line shapes. This broadening is consistent with non-Fourier transform limited pulses as was seen in the pulsed-source DH experiment [34, 56]. Additionally, the ambiguity efficiency FWHM is 58% of the ambiguity efficiency FWHM calculated for the

idealized fields. Therefore, a single mode hop within the laser source is a valid potential solution to the over-prediction of the model in the pulsed-source DH experiment.

D.4.3 Chirp

Due to the construction of the laser used during the pulsed-source DH experiment[20, 25], it is also possible an unintended chirp was added to the laser mode frequencies. As stated in Section 2, the inclusion of a chirp would change the idealized temporal fields in Eq. (D.5) such that

$$U_n(t) = A_t(t)\, exp\left(j\omega_n t\right) exp\left(j\pi t^2 \beta / T\right), \tag{D.9}$$

where again β is the bandwidth of the chirp and T is the temporal FWHM[24]. While the temporal FWHM is fixed by A_t, the chirp bandwidth can theoretically be any value. Therefore, it is necessary to investigate the effect of the size of the chirp bandwidth. To this end, Eq. (D.9) was used as the temporal fields in Eqs. (D.6) and (D.7) to calculate the ambiguity efficiency as the chirp bandwidth was increased from 0 MHz to 60 MHz in 2 MHz steps. For a convenient comparison, the FWHM's of the spectral line shapes and of the ambiguity efficiency were calculated as functions of chirp bandwidth. The results are shown in Fig. D.5.

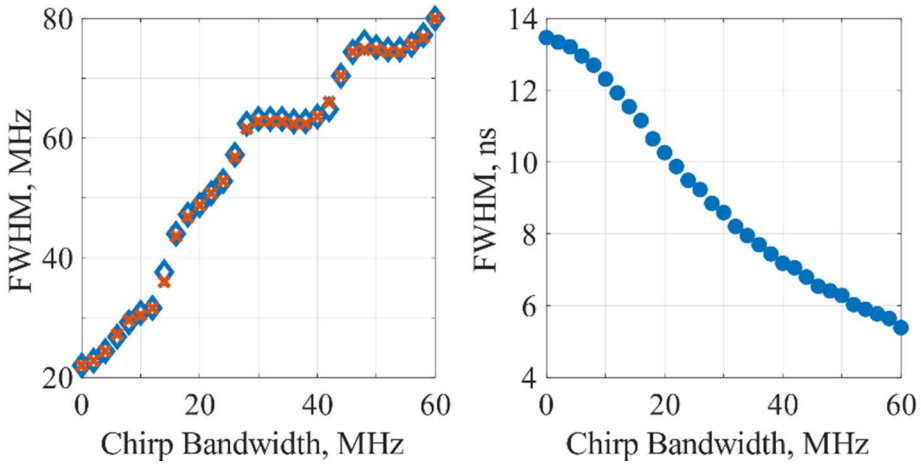

Figure D.5. The FWHM's of (a) both the fundamental mode (♦) and the secondary mode (×) spectral line shapes and (b) the ambiguity efficiency as functions of chirp bandwidth.

As seen in Fig. D.5(b), the FWHM of the ambiguity efficiency when a 34 MHz chirp is included in the model is 59% of the FWHM of the idealized ambiguity efficiency. In Fig. D.5(a), the FWHM's of the spectral line shapes for a 34 MHz chirp increase to approximately 63 MHz. This width is consistent with the spectral mode widths in the pulsed-source DH experiment, as seen in Fig. D.1(b). Together, these results indicate the effect of a 34 MHz chirp bears further investigation. To accomplish this, the diagnostics and ambiguity efficiency calculated using a chirp bandwidth of 34 MHz are displayed in Fig. D.6.

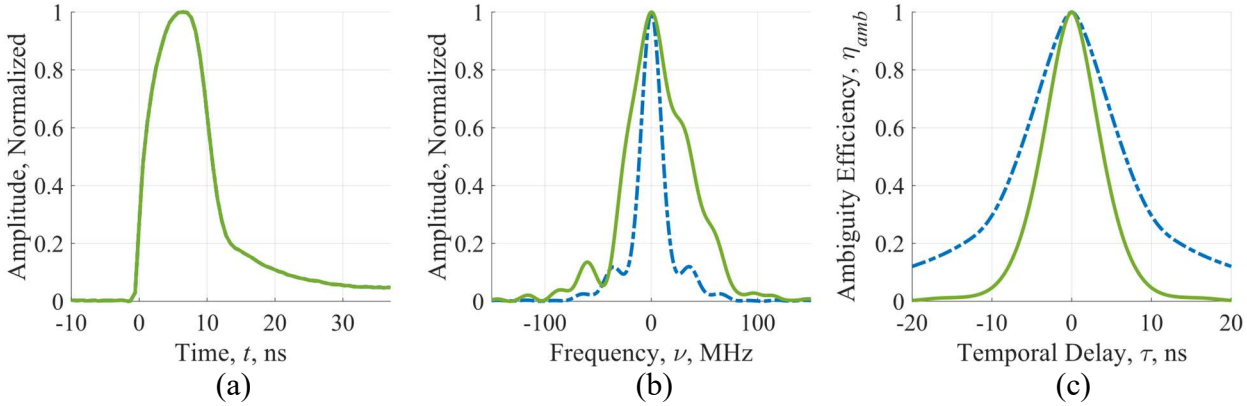

Figure D.6. The (a) temporal diagnostic, (b) spectral diagnostic, and (c) ambiguity efficiency calculated for the 34 MHz chirp scenario. For all plots, the calculations which included the chirp (–) are compared with the idealized calculations (– –).

As seen in Fig. D.6(a), including a chirp does not affect the temporal diagnostic. Additionally, Fig. D.6(c) reaffirms the proper narrowing of the ambiguity efficiency. However, Fig. D.6(b) shows a potentially significant change in the spectral diagnostic. As mentioned above, the overall broadening is not concerning. On the other hand, the asymmetry of the line shape requires further consideration. The modulation on the leading-edge seemingly deepens and the modulation on the trailing-edge is smoothed out. Some of the smaller-scale modulation in the far wings of the line shape could be below the noise floor of a spectral measurement device, and therefore lost. It is reasonable to believe the peak with approximately 13% the amplitude of the main peak would be above the noise floor, especially when compared with Fig. D.1(b). However, it is important to remember the true spectral line shape of the fields used in the pulsed-source DH experiment were most likely not completely Lorentzian but were instead Voigt. Chirp may add less to the leading-edge modulation for Voigt profiles. Therefore, chirp as a potential solution should not be eliminated solely for increasing leading-edge modulation. Taking this into consideration, and with the other results presented above, chirp within the laser source is a valid potential solution to the over-prediction of the model in the pulsed-source DH experiment.

D.5 Conclusion

A previous experiment quantified the system efficiencies for a pulsed-source DH system in the off-axis IPRG [34]. As part of this experiment, a model was built to predict a novel efficiency unique to pulsed-source DH systems, called the ambiguity efficiency. That model over-predicted system performance when the reference and signal fields were not well overlapped at the point of detection. This paper investigated two potential solutions to this overestimation: including either a mode hop or a chirp in the temporal fields used to calculate the predicted ambiguity efficiency. Both potential solutions were shown to correct for the overestimation in the original model in terms

of the ambiguity efficiency FWHM. However, the inclusion of a chirp requires careful scrutiny of the effect on spectral line shape before it can be used. From these findings, it can be concluded that the model for the ambiguity efficiency presented in the pulsed-source DH experiment is valid.

Bibliography

1. R. K. Tyson, *Introduction to Adaptive Optics*. SPIE Press, 2011.

2. D. L. Fried, “Branch point problem in adaptive optics,” J. Opt. Soc. Am. A, vol. 15, no. 10, pp. 2759-2768, (1998).

3. W. Goodman, W. H. Huntley, D. W. Jackson, and M. Lehmann, “Wavefront-reconstruction imaging through random media," Appl. Phys. Lett., vol. 8, no. 12, pp. 311-313, (1966).

4. J. W. Goodman and R. W. Lawrence, “Digital image formation from electronically detected holograms," Appl. Phys. Lett., vol. 11, no. 3, pp. 77-79, (1967).

5. J. W. Goodman, D. W. Jackson, M. Lehmann, J. Knotts, and A. P. Profile, “Experiments in Long-Distance Holographic Imagery," Appl. Opt., vol. 8, no. 8, pp. 1581-1586, (1969).

6. M. F. Spencer, R. A. Raynor, M. T. Banet, and D. K. Marker, “Deep-turbulence wavefront sensing using digital-holographic detection in the off-axis image plane recording geometry,” Opt. Eng., vol. 56, no. 3, 031213 (2016).

7. M. T. Banet, M. F. Spencer, and R. A. Raynor, “Digital-holographic detection in the off-axis pupil plane recording geometry for deep-turbulence wavefront sensing,” App. Opt., vol. 57, no. 3, pp. 465–475 (2018).

8. D. E. Thornton, M. F. Spencer, and G. P. Perram, “Deep-turbulence wavefront sensing using digital holography in the on-axis phase shifting recording geometry with comparisons to the self-referencing interferometer,” App. Opt., vol. 58, no. 5, pp. A179–A189 (2019).

9. M. F. Spencer, “Limitations of the Deep-Turbulence Problem,” Proc. OSA, PW3F.1 (2021).

10. J. W. Goodman and R. W. Lawrence, “Digital image formation from electronically detected holograms,” App. Phys. Lett., vol. 11, no. 3, pp. 77-79 (1967).

11. J. C. Marron and K. S. Schroeder, “Holographic laser radar,” Opt. Lett., vol.18, no. 5, pp. 385–387 (1993).

12. J. C. Marron, R. L. Kendrick, N. Seldomridge, T. D. Grow, and T. A. Höft, “Atmospheric turbulence correction using digital holographic detection: experimental results,” Opt. Exp., vol. 17, no. 14, pp. 11638–11651 (2009).

13. A. E. Tippie and J. R. Fienup, “Phase-error correction for multiple planes using a sharpness metric,” Opt. Lett., vol. 34, no. 5, pp. 701–703 (2009).

14. A. E. Tippie and J. R. Fienup, “Multiple-plane anisoplanatic phase correction in a laboratory digital holography experiment,” Opt. Lett., vol. 35, no. 19, pp. 3291–3293 (2010).

15. C. J. Pellizzari, M. F. Spencer, and C. A. Bouman, “Imaging through distributed-volume aberrations using single-shot digital holography,” J. Opt. Soc. Am. A., vol. 36, no. 2, pp. A20–A33 (2019).

16. C. J. Radosevich, C. J. Pellizzari, S. Horst, and M. F. Spencer, “Imaging through deep turbulence using single-shot digital holography data,” Opt. Exp., vol. 28, no. 13, pp. 19390–19401 (2020).

17. D. E. Thornton, M. F. Spencer, C. A. Rice, and G. P. Perram, “Digital holography efficiency measurements with excess noise,” App. Opt., vol. 58, no. 34, pp. G19-G30 (2019).

18. D. E. Thornton, D. Mao, M. F. Spencer, C. A. Rice, and G. P. Perram, “Digital holography experiments with degraded temporal coherence,” Opt. Eng., vol. 59, no. 10, 102406 (2020).

19. D. E. Thornton, M. F. Spencer, C. A. Rice, and G. P. Perram, “Impacts of Laboratory Vibrations and Laser Flicker Noise,” IEEE J. Quantum Electron., vol. 56, no. 5, 1400107 (2020).

20. D. E. Thornton, C. J. Radosevich, S. Horst, and M. F. Spencer, “Achieving the shot-noise limit using experimental multi-shot digital holography data,” Opt. Exp., vol. 29, no. 6, pp. 9599-9617 (2021).

21. D. E. Thornton, M. T. Banet, and M. F. Spencer, “Subaperture sampling for digital-holography applications involving atmospheric turbulence,” App. Opt., vol. 60, no. 25, pp. G30-G39 (2021).

22. M. F. Spencer, “Spatial Heterodyne,” in *Encyclopedia of Modern Optics, 2nd ed*., Bob Guenther and Duncan Steel, Eds., Elsevier, Amsterdam, The Netherlands (2018).

23. B. Javidi, A. Carnicer, A. Anand, G. Barbastathis, W. Chen, P. Ferraro, J. W. Goodman, R. Horisaki, K. Khare, M. Kujawinska, R. A. Leitgeb, P. Marquet, T. Nomura, A. Ozcan, Y. Park, G. Pedrini, P. Picart, J. Rosen, G. Saavedra, N. T. Shaked, A. Stern, E. Tajahuerce, L. Tian, G. Wetzstein, and M. Yamaguchi, “Roadmap on digital holography [Invited],” Opt. Exp., vol. 29, no. 22, pp. 35078-35118 (2021).

24. S. Schedin, G. Pedrini, H. J. Tiziani, and F. M. Santoyo, “Simultaneous three-dimensional dynamic deformation measurements with pulsed digital holography,” App. Opt., vol. 38, no. 34, pp. 7056-7062 (1992).

25. A. T. Saucedo, F. M. Santoyo, M. Torre-Ibarra, G. Pedrini, and W. Osten, "Endoscopic pulsed digital holography for 3D measurements," Opt. Exp., vol. 14, no. 4, pp. 1468-1475 (2006).

26. P. H. Merritt and M. F. Spencer, Beam Control for Laser Systems, 2nd ed., Directed Energy Professional Society, Albuquerque New Mexico (2018).

27. A. E. Tippie, Aberration Correction in Digital Holography. PhD dissertation, Univ. of Rochester, Volume AS38.6635, (2012).

28. J. D. Schmidt, *Numerical Simulation of Optical Wave Propagation with examples in MATLAB*, SPIE Press, 2010.

29. D. L. Fried, "Optical Resolution Through a Randomly Inhomogeneous Medium for Very Long and Very Short Exposures," J. Opt Soc. Am., vol. 56, no. 10, pp. 1372-1379, (1966).

30. E. L. Dereniak and G. D. Boreman, *Infrared Detectors and Systems*, New York, NY: John Wiley & Sons, Inc., 1996.

31. P. M. Woodward, *Probability and Information Theory with Applications to Radar*, Norwood, MA: Artech House, 1980.

32. N. Levanon and E. Mozeson, *Radar Signals*, Hoboken, NJ: John Wiley & Sons, Inc. (2004).

33. M. A. Richards, J. A. Scheer, and W. A. Holm, *Principles of Modern Radar, Vol. I: Basic Principles*, Raleigh, NC: SciTech Publishing, 2015.

34. S. A. Owens, M. F. Spencer, D. E. Thornton, and G. P. Perram, "Pulsed laser source digital holography efficiency measurements," Appl. Opt., vol. 61, no. 16, pp. 4823-4832 (2022).

35. M. T. Banet and M. F. Spencer, "Compensated-beacon adaptive optics using least-squares phase reconstruction," Opt. Exp., vol. 28, no. 24, pp. 36902–36914 (2020).

36. M. T. Banet, J. R. Fienup, J. D. Schmidt, and M. F. Spencer, "3D multi-plane sharpness metric maximization with variable corrective phase screens," App. Opt., vol. 60, no. 25, pp. G243-G252 (2021).

37. L. Mandel, "Wavefront reconstruction with light of finite coherence length," J. Opt. Soc. Am., vol. 56, no. 11, pp. 1636_1–1637 (1966).

38. L. Martínez-León, G. Pedrini, and W. Osten, "Applications of short-coherence digital holography in microscopy," App. Opt., vol. 44, no. 19, pp. 3977–3984 (2005).

39. T. C. Poon and J. P. Liu, *Introduction to Modern Digital Holography with MATLAB*, Cambridge University Press, New York, New York (2014).

40. G. T. Nehmetallah, R. Aylo, and L. A. Williams, *Analog and Digital Holography with MATLAB*, SPIE Pres, Bellingham, Washington (2015).

41. L. G. Weiss, "Wavelets and Wideband Correlation Processing," IEEE Sig. Proc. Mag., vol. 11, no. 1, pp. 13-32 (1994).

42. J. W. Goodman, *Statistical Optics, Second Edition*, Wiley, Hoboken, New Jersey (2015).

43. A. E. Siegman, "Why the sinc function should be defined as (sinx)/x and not (sinpix/pix)," Appl. Opt., vol. 13, no. 4, pp. 705–706 (1974).

44. W. H. Steel, "Why the sinc function should be defined as (sin x)/x and not (sin pi x)/pi x comments," Appl. Opt., vol. 13, no. 8, pp. 1734 (1974).

45. Coherent High Energy Pulsed Fiber Laser System (CHELS) Product User Manual (6000456), NP Photonics (2020).

46. L. Mandel, "Fluctuations of Photon Beams and their Correlations," Proc. Phys. Soc., vol. 72, no. 6, pp. 1037-1048 (1958).

47. S. A. Owens, M. S. Spencer, and G. P. Perram, "Digital-holography efficiency measurements using a heterodyne-pulsed configuration," Opt. Eng., submitted for publication.

48. S. A. Owens, M. F. Spencer, and G. P. Perram, "Complex phase effects on a pulsed-source digital holography system," Proc. SPIE 12092, 1209206 (2022).

49. W. E. Martin and D. Milam, "Interpulse interference and passive laser pulse shapers," Appl. Opt., 15(12), 3054-3061 (1976).

50. B. J. Davis, "Observable coherence theory for statistically periodic fields, "Phys. Rev. A 76(4), 043843 (2007).

51. R. W. Schoonover, B. J. Davis, R. A. Bartels, and P. S. Carney, "Optical interferometry with pulsed fields," J. of Mod. Opt. 55(10), 1541-1556 (2008).

52. Y. Liu, L Yang, Y. Guo, J. Lin, P. Cui, and J. Zhu, "Optimization methods of pulse-to-pulse alignment using femtosecond pulse laser based on temporal coherence function for practical distance measurement," Opt. and Lasers in Eng. 101, 35-43 (2018).

53. R. Dutta, A. T. Friberg, G. Genty, and J. Turunen, “Two-time coherence of pulse trains and the integrated degree of temporal coherence,” J. Opt. Soc. Am. A 32(9), 1631-1637, 2015.

54. L. L. Steinmetz, W. A. Bookless, and J. H. Richardson, “Recent pulse width and linewidth measurements on the mode-locked Kr+-ion laser,” Appl. Opt., vol. 19, no. 16, pp. 2663-2665 (1980).

55. J. Xue, W. Chen, Y. Pan, J. Shi, Y. Fang, H. Xie, M. Xie, L. Sun, and B. Su, “Pulsed laser linewidth measurement using Fabry-Perot scanning interferometer,” Res. Phys., vol. 6, pp. 698-703 (2016).

56. A. Webster, *Useful Mathematical Formulas for Transform Limited Pulses*, 2012.

57. J. W. Goodman, *Introduction to Fourier Optics*, *Fourth Edition*, W. H Freeman and Company, New York, New York (2017).

58. C. Zeringue, I. Dajani, S. Naderi, G. T. Moore, and C. Robin, "A theoretical study of transient stimulated Brillouin scattering in optical fibers seeded with phase-modulated light," Opt. Exp., vol. 20, no. 19, pp. 21196-21213 (2012).

59. A. Flores, C. Robin, A. Lanari, and I Dajani, “Pseudo-random binary sequence phase modulation for narrow linewidth, kilowatt, monolithic fiber amplifiers,” Opt. Exp., vol. 22, no. 15, pp. 17735-17744 (2014).

60. E. D. Lipson, K. W. Foster, and M. P. Walsh, “A versatile pseudo-random noise generator,” IEEE Trans. Inst. Meas., vol. 25 no. 2, pp. 112-116 (1976).

61. J. T. Verdeyen, *Laser Electronics*, 3rd ed., Prentice Hall, Upper Saddle River, NJ (1995).

62. E. Abramochkin and V Volostnikov, “Beam transformations and nontransformed beams,” Opt. Comm., vol. 83, nos. 1-2, pp. 123-135 (1991).

63. G. Liang and Q. Wang, “Controllable conversion between Hermite Gaussian and Laguerre Gaussian modes due to cross phase,” Opt. Exp., vol. 27, no. 8, pp. 10684-10691 (2019).

64. E. D. Hinkley and C. Freed, “Direct observation of the Lorentzian line shape as limited by quantum phase noise in a laser above threshold,” Phys. Rev. Lett., vol. 23, no. 6, pp. 277-280 (1969).

65. A. Demir, A. Mehrotra, and J. Roychowdhury, “Phase noise in oscillators: a unifying theory and numerical methods for characterization,” IEEE Trans. Circ. Syst. I: Fund. Thry. Appl., vol. 47, no. 5, pp. 655-674 (2000).

66. A. D. Kersey, M. A. Davis, et. al., “Fiber grating sensors,” J. of Lightwave Tech., vol. 15, no. 8, pp. 1442-1463 (1997).

67. L. Jin, W, Zhang, et. al., “An embedded FBG sensor for simultaneous measurement of stress and temperature,” IEEE Photonics Tech. Lett., vol. 18, no. 1, pp. 154-156 (2006).

REPORT DOCUMENTATION PAGE

1. REPORT DATE	2. REPORT TYPE	3. DATES COVERED	
		START DATE	END DATE
20220815	Doctoral Dissertation	20190901	20220915

4. TITLE AND SUBTITLE

Efficiency Quantification for Pulsed-Source Digital Holographic Wavefront Sensing

5a. CONTRACT NUMBER	5b. GRANT NUMBER	5c. PROGRAM ELEMENT NUMBER
5d. PROJECT NUMBER	**5e. TASK NUMBER**	**5f. WORK UNIT NUMBER**

6. AUTHOR(S)

Owens, Steven, A

7. PERFORMING ORGANIZATION NAME(S) AND ADDRESS(ES)

Air Force Institute of Technology
Graduate School of Engineering and Management (AFIT/EN)
2950 Hobson Way
WPAFB, OH 45433-7765

8. PERFORMING ORGANIZATION REPORT NUMBER

AFIT-DS-ENP-22-S-046

9. SPONSORING/MONITORING AGENCY NAME(S) AND ADDRESS(ES)	10. SPONSOR/MONITOR'S ACRONYM(S)	11. SPONSOR/MONITOR'S REPORT NUMBER(S)
National Reconnaissance Office 14675 Lee Road Chantilly, VA 20151	NRO	

12. DISTRIBUTION/AVAILABILITY STATEMENT

DISTRIBUTION STATEMENT A:
APPROVED FOR PUBLIC RELEASE; DISTRIBUTION UNLIMITED.

13. SUPPLEMENTARY NOTES

14. ABSTRACT

The efficiencies of a digital holography (DH) system in the pulsed configuration and the off-axis image plane recording geometry are analyzed. The system efficiencies of an infrared-wavelength DH system in a homodyne-pulsed configuration are compared to those of a visible-wavelength DH system in a homodyne-continuous-wave (CW) configuration. All measured efficiencies were found to be consistent between systems. The consistency of efficiencies also showed infrared DH systems are viable but degraded due to infrared detector technology. A new efficiency, called the ambiguity efficiency, was experimentally verified. Also, a DH system in a heterodyne-pulsed configuration was characterized and compared to a homodyne-pulsed configuration. System performance was consistent. The effect of spectrally broadening the source laser of a DH system in the heterodyne-pulsed configuration was analyzed.

15. SUBJECT TERMS

Digital-holography; pulsed-source; ambiguity efficiency; wavefront sensing, deep-turbulence; coherence

16. SECURITY CLASSIFICATION OF:			17. LIMITATION OF ABSTRACT	18. NUMBER OF PAGES
a. REPORT	b. ABSTRACT	C. THIS PAGE		
U	U	U	UU	138